Multimaterial multifunctional fibers for biomedical applications

Shan Jiang

Dissertation submitted to the faculty of the Virginia Polytechnic Institute and State University in partial fulfillment of the requirements for the degree of

Doctor of Philosophy

In

Electrical Engineering

Xiaoting Jia, Chair

Anbo Wang

Wei Zhou

Qiang Li

Harald Sontheimer

May 4th, 2021
Blacksburg

Keywords: multifunctional fiber, electrophysiology recording, multisite neural interfacing, bioimpedance sensing

Multimaterial multifunctional fibers for biomedical applications

Shan Jiang

ABSTRACT

The aim of my Ph.D. thesis is to summarize my research on the development of multimateiral multifunctional fibers for bio-related application, mainly in the fields of neural interfacing and bioimpedance sensing.

Understanding the cytoarchitecture and wiring of the brain requires improved methods to record and stimulate large groups of neurons with cellular specificity. This requires the development of improved miniaturized neural interfaces that integrate into brain tissue without altering its properties. Despite the advancement of the existing neural interface technologies such as microwires, silicon-based multielectrode arrays, and electrode arrays with flexible substrates, the physical properties of these devices limit their access to one, small brain region with single implantation.

Beyond neural interfacing, extracting molecular information is crucial for understanding many neurological diseases and disorders. The most adapted methods are fast scan cyclic voltammetry and microdialysis. However, both have some limitations such as offline sensing or lack of selectivity. Furthermore, by concentrating optical fields at the nanoscale, plasmonic nanostructures can serve as optical nanoantennas to achieve ultrasensitive bio-/chemical sensing. But due to the limitation of the sensing mechanism, it is hard to perform the plasmonic sensing in live animals.

Moreover, the relatively poor electrical performance of the electrode materials that can be utilized in the thermal drawing process limits the function of the fiber in other types of biomedical application, such as deep brain stimulation and electrochemical sensing. For example, the large

inherent electrical resistance of the electrode material will significantly interference the electrical impedance result while the main purpose of this kind of study is to explore the frequency-dependent electrical properties of the tested subjects.

To overcome above difficulties This thesis introduces broad application of multimaterial multiplexed fibers in biomedical areas. I first describe the development and application of spatially expandable multifunctional fiber-based probes for mapping and modulating brain activities across distant regions in the deep brain (Chapter 2). Secondly, I present the flexible nano-optoelectrodes integrated multifunctional fiber probes that can have hybrid optical-electrical sensing multimodalities, including optical refractive-index sensing, surface-enhanced Raman spectroscopy, and electrophysiological recording (Chapter 3). Thirdly, I demonstrate that hollow multifunctional fibers enable in-line impedimetric sensing of bioink composition and exhibit selectivity for real-time classification of cell type, viability, and state of differentiation during bioprinting (Chapter 4). The same device allows for local delivery of immune checkpoint blockade antibodies and for monitoring of clinical outcomes by tumor impedance measurement over the course of weeks with the photodynamic therapy option to enhance anti-tumor immunity and prolong intratumoral drug retention (Chapter 5). An overview future work has been summarized (Chapter 6).

Multimaterial multifunctional fibers for biomedical applications

Shan Jiang

GENERAL AUDIENCE ABSTRACT

Electrode technology has played an indispensable role in neuroscience community since the first employment of insulated tungsten wire in cat brain in 1950s. The electrophysiological signal acquired from or the electrical current delivered to the brain tissue using the implanted electrode, has permitted us to understand the functional networks in the brain and treat neurological diseases. Over the past decades, significant progress has been made in developing miniaturized electrical neural interfaces. The development of optogenetics involving genetically-modified neurons that express light-sensitive proteins (opsins) has provided a powerful tool for modulating the neuronal activity to be switched on or off using light at a particular wavelength. Leveraging the thermal drawing process (TDP) from optical fiber industry for producing conventional silica fibers, multifunctional fiber-based neural probes have recently been developed, allowing for simultaneous optical stimulation, electrical recording, and drug delivery *in vivo*. However, the interfacing sites in these fiber-based neural probes have been restricted to a single location (at the fiber tip) so far, making the broad application of these probes unfeasible.

Beyond neural interfacing, extracting molecular information is crucial for understanding many neurological diseases and disorders. The most adapted methods are fast scan cyclic voltammetry and microdialysis. However, both have some limitations such as offline sensing or lack of selectivity. Furthermore, by concentrating optical fields at the nanoscale, plasmonic nanostructures can serve as optical nanoantennas to achieve ultrasensitive bio-/chemical sensing. But due to the limitation of the sensing mechanism, it is hard to perform the plasmonic sensing in live animals.

To overcome these limitations, we first developed a platform that provides three-dimensional coverage of brain tissue through multifunctional polymer fiber-based neural probes capable of interfacing simultaneously with neurons in multiple sites (Chapter 2). In a later study, we demonstrate that conductive nanoantenna arrays can be integrated with microelectrodes on the tip of multifunctional fiber probes as nano-optoelectrodes to enable optical bio-/chemical spectroscopy as well as to improve electrophysiology recording (Chapter 3).

Besides, inspired by a convergence fiber drawing method, we have also managed to incorporate copper wires inside multifunctional fibers with a hollow channel in the center, in favor of high electrical conductivity. This technology developed here holds great promise for electrochemical impedance sensing of the tested media without the interference from the utilized electrodes' high resistance. Hence, by exploiting the functional fibers and the superior electrical performance, the copper-electrode-based fiber has been used for in vitro bioink bioimpedance sensing during 3D printing process (Chapter 4) and in vivo tumor impedance monitoring and drug delivery (Chapter 5).

In summary, my research produces unique platforms for fundamental research studies as well as the readily translational application for human subjects. Given the scalable, straightforward, and versatile fabrication method, the multifunctional fibers delivered by our team would pave the way for new engineered tools for broad biomedical community.

Acknowledgments

Pursuing this doctoral degree has been a life-changing experience for me. Looking back on all the memorable moments during this journey, I feel extraordinarily proud of myself for hanging on to the right path by conquering all the difficulties and letting go of the past. This journey has not only taught me science but also equipped me with the ability of critically thinking, working with others, and appreciating small things in every normal daily life.

I still remember the scene when I received the very first email from Prof. Jia asking whether I was still interested in joining her group. Ever since then, Prof. Jia has been an advisor and mentor of mine with tremendous supports and cares. I'm truly grateful for her choosing me as her first Ph.D. student and the opportunity of developing state-of-the-art technology. I will not forget the moments when she immediately responded to my text messages of exciting recording results at 4 am, when we were revising documents together till 3 am over the phone, when she calmed me down after my emotional breakdowns with her tender and encouraging voice. Her enthusiasm for science has inspired me to outperform myself and I would not have made this far without her unconditional support and guidance. It is her one hundred percent trust and encouragement that shape me into an independent researcher. Her dedication to work and family will always positively influence me, and she will remain as my role model for a mentor and scientist.

Working with Prof. Sontheimer has also been a very valuable and fortunate experience for me. As a mentor with a completely different background, he is always willing to share his knowledgeable suggestions and comments with me from a very different perspective, which oftentimes illuminates me on the matter of research. I remember him saying, 'It usually takes two

weeks to get all the data for the experiments, but it always takes two years to find these two weeks.', 'Where do you see yourself in five years?', 'What is the title of your first R01?'. All his inadvertent words have inspired me to think far beyond the present and understand more about the natures of a doctoral degree and life. His action towards vonlunteering in COVID-19 sample testing will always remind me to pay back to the community in every possible way as a scientist. I am very grateful for his generous support for my research and his willingness to see me as a member of his lab.

I would like to extend my gratitude to other members of my Ph.D. advisory committee, Prof. Anbo Wang, Prof. Wei Zhou, and Prof. Qiang Li for their insightful advice and constructive comments.

My special gratitude to Paul Youmans, a generous man who would always put other people's needs in priority. He had taken me under his wings since the beginning of my working with animals as the former lab manager of Sontheimer lab. Thank you, Paul, for taking care of my animals, for helping me put up the protocols, for remembering my birthday with a cupcake surprise, and for everything that you did for us.

Studying in the multi-disciplinary field allows me to explore different research areas and it would not have been such a pleasant experience without the welcome and pleasing environments provided by the awesome colleagues from different labs. I would like to thank all the colleagues that I have worked with from the Center for Photonics Technology (CPT), Sontheimer lab, Tong lab, Zhou lab, and Johnson lab. Here I would like to thank Yuanyuan Guo for mentoring me when I first came to Virginia Tech, Bo Dong for always offering help whenever I needed it, Dipan for

patiently and generously sharing his skills and knowledge with me, Tre for teaching me the very basics of staining, and Jenny for breeding mice for me.

My life in Blacksburg has been quite joyful thanks to my friends' companion. Many thanks to the hangouts and delicious food that warms my soul, allowing me to release burdens and beat fatigues. Special thanks to Albert Zhong, Huishan Yang, Junran Xu, Zhen Guo, Tre Mills, Yujing Zhang, Ziang Feng, and Yuan Yao for all the precious moments we shared. I will definitely miss the days and nights, holidays and birthdays we spent together, and all the laughs, cries, singing, late-night talking, painting, dancing, swimming, hiking, and running. Wish you guys all the best.

I also thank my friends that I have known for over ten years. They have given me strong support when I need it the most. Will you all have great and happy families.

To my parents and grandparents, I express my deepest gratitude for their unfaltering love and support. They have truly been supportive and caring throughout my entire life and concerned about me using their own way even we are half of the world away. I'm also very grateful for their strong spirits and healthy conditions during the special times in 2020. They have taught me how to be an honest, positive, loving, and generous person using their entire life. I would not be the person I am today without their patience, love, and support.

Table of Contents

Chapter 1 Introduction..... 1

1.1 Existing electrical brain interface 2

1.1.1 Electrical neural interface at a single site 2

1.1.2 Linear multi-electrode arrays..... 4

1.1.3 Two-dimensional penetrating and flexible planar electrode array 5

1.1.4 Neural probes with three-dimensional topological structure..... 8

1.2 Delivery of electrochemical techniques..... 9

1.2.1 Electrical detection of biomolecules..... 10

1.2.2 Electrochemical impedance spectroscopy for tissue monitoring..... 12

1.3 Multimaterial multifunctional fiber 13

1.4 Scope and organization..... 17

1.5 References..... 19

Chapter 2 Spatially expandable fiber-based probes as a multifunctional deep brain interface 25

2.1 Introduction..... 25

2.2 Results and discussion 27

2.2.1 Depth-dependent multifunctional fibers 27

2.2.2 Spatially expandable multifunctional fiber-based probes..... 33

2.2.3 Spike recording and burst-suppression recording using spatially expandable fiber probes..... 37

2.2.4 Optogenetic control and electrophysiological readout with implanted fibers 40

2.2.5 Multisite in vivo recordings by fiber probes in a mouse model of infection-induced epilepsy 47

2.2.6 Evaluation of fiber probe and stainless steel microwire biocompatibility using immunohistochemistry..... 52

2.3 Materials and methods..... 55

2.4 Conclusion 65

2.5 References 66

Chapter 3 Nano-optoelectrodes integrated with flexible multifunctional fiber probes by high-throughput scalable fabrication 70

3.1 Introduction 70
3.2 Results and discussion 72
3.2.1 Fabrication of nano-optoelectrodes on multifunctional fibers 72
3.2.2 Refractive index sensing and SERS measurement 75
3.2.3 Electrical characterization of the surface modified electrodes 78
3.2.4 In vivo electrophysiology 81
3.2.5 Biocompatibility of the surface modified electrode 84
3.3 Conclusion 85
3.4 Materials and methods 86
3.5 References 94

Chapter 4 3D Bioprinting using hollow multifunctional fiber impedimetric sensors 97

4.1 Introduction 97
4.2 Results and discussion 99
4.2.1 Principle of in-line bioink compositional analysis for 3D bioprinting processes 99
4.2.2 Fabrication of hollow multifunctional fibers for extrusion of cell-laden bioinks 100
4.2.3 Detection of cell viability differences 103
4.2.4 Examination of bioinks with different cell type 105
4.2.5 Signal response to stem cells and differentiated cells 107
4.3 Conclusions 111
4.4 Materials and methods 111
4.5 References 117

Chapter 5 Implantable miniature optical fibers for on-demand delivery of checkpoint immunotherapies and tumor impedance measurement 119

5.1 Introduction 119
5.2 Results and discussion 121

5.2.1 Design and fabrication of IMOD and its use for in vitro drug release 121
5.2.2 In vivo tumor impedance measurement 125
5.2.3 Circuit model analysis 127
5.2.4 Effect of PDT on intratumoral drug retention 131
5.2.5 Tumor impedance measurement responds to the ICB antibody treatment via IMOD 132
5.3 Conclusions 133
5.4 Materials and methods 134
5.5 References 139

Chapter 6 Overview and future direction 144

6.1 Overview 144
6.2 Future direction 145
6.3 References 151

List of Figures

Figure 2.1 Depth-dependent multifunctional fiber probe. 28

Figure 2.2 Depth-dependent fiber probes (Fiber S1-2). 29

Figure 2.3 2D simulation of the scattered light intensity from a femtosecond-laser exposed waveguide. 31

Figure 2.4 EIS measurement of the exposed electrode of Fiber F3. 32

Figure 2.5 Characterization of optical properties of Fiber F2 and Fiber F4. 33

Figure 2.6 Spatially expandable multifunctional fiber-based probes. 35

Figure 2.7 Spontaneous activity investigation by spatially-expanded functional fiber probes (F1, n=5). 38

Figure 2.8 LFP recordings from spatially expandable fiber probes. 40

Figure 2.9 Simultaneous multisite optogenetic stimulation, electrical recording, and drug delivery. 42

Figure 2.10 Normalization of the recording results from depth-dependent probes and spatially expandable fiber probes. 44

Figure 2.11 Recordings from a perfused brain with optical stimulation of 10 Hz by the depth-dependent fiber probes. 45

Figure 2.12 Light efficiency measurement of a single exposed optical window. 45

Figure 2.13 Simultaneous optical stimulation and electrical recording in Thy1 mouse using the depth-dependent fiber probes. 46

Figure 2.14 Unfiltered, Spike-filtered, and LFP filtered recording results before, during and after CNQX administration in a transgenic Thy1-ChR2-YFP mouse brain. 46

Figure 2.15 Similar brain activity of the seizure-like afterdischarges detected by other three brain regions. 47
Figure 2.16 Multisite recording of seizure activity in various brain regions in a mouse model of infection-induced epilepsy. 50
Figure 2.17 Convulsive seizure detected by depth-dependent fiber probe (straight implant). 52
Figure 2.18 Biocompatibility study of the functional fiber probes (Fiber F1) and stainless steel wire. 53
Figure 2.19 Immunohistochemical comparison of tissue reaction to chronically implanted multimodal Fiber F2 and conventional stainless steel probes after four-week implantation. 54
Figure 2.20 Location of depth-dependent fiber probe implanted angularly to the brain surface for electrophysiological recording. 60
Figure 3.1 Fabrication of nano-optoelectrodes on multifunctional fiber tips. 73
Figure 3.2 Transmission spectra of the silica fiber before drawing and in the drawn multifunctional fiber. 74
Figure 3.3 Refractive index sensing and SERS measurements from nano-optoelectrodes integrated fiber probes. 76
Figure 3.4 FDTD-simulated extinction spectra in different background refractive index environments. 77
Figure 3.5 EIS measurements and the equivalent circuit model fitting of the electrode before and after surface modification. 79
Figure 3.6 Electrophysiology recording from the surface-modified CNF-CPE electrodes, and its comparison with that from the unmodified electrodes. 83

Figure 3.7 Power spectral density of the recording from surface modified and unmodified electrodes. 84
Figure 3.8 Immunohistological comparison of tissue reaction to chronically implanted surface modified probes (center) and conventional stainless steel probes (right) after two-week implantation. 85
Figure 3.9 Schematic illustration of the extinction measurement. 89
Figure 4.1 Sensing principle of the bioink during 3D printing process. 100
Figure 4.2 Fabrication of hollow multifunctional fibers. 103
Figure 4.3 EIS recording of bioinks with different cell viabilities. 105
Figure 4.4 Bioimpedance reading of bioinks with diverse cell types. 107
Figure 4.5 Measurements of bioinks to the extent of diffrenciation. 110
Figure 5.1 Design and fabrication of an implantable miniaturize optical fiber device (IMOD) for on-demand drug delivery and tumor impedance measurement. 123
Figure 5.2 In vitro sustained release of drugs loaded onto the fiber in IMOD. 124
Figure 5.3 Ex vivo intratumoral release of fibers loaded with different drugs. 125
Figure 5.4 The use of IMOD for tumor impedance measurement. 126
Figure 5.5 In vivo tumor impedance measurements using IMOD. 127
Figure 5.6 Modeling of tumor impedance measurement in E0771 tumors and comparison between experiments and simulation curves. 128
Figure 5.7 Combined fitting results of tumor G4M2 and G4M3. 131
Figure 5.8 Effect of photodynamic therapy (PDT) on intratumoral retention of proteins. 132
Figure 5.9 Correlation between tumor shrinkage and impedance (highlighted in light green). . 133

Figure 6.1 Schematic illustration of the designed fiber structure with 9 electrodes and 9 waveguides. 146
Figure 6.2 Illustration of the fiber-to-chip bonding (left) with detailed electrical (top right) and photonic (bottom right) bonding methods. 147
Figure 6.3 Impedance results of the CNT-CPE electrode. 148
Figure 6.4 In vivo electrophysiology result by using the CNT-CPE electrode. 149

List of Tables

Table 3.1 Means and standard deviations (SD) of parameters in the equivalent circuit model with the unmodified probe. 80

Table 3.2 Means and standard deviations (SD) of parameters in the equivalent circuit model with the surface-modified probe. 81

Table 5.1 Means and standard deviations (SD) of parameters in the equivalent circuit model from different impedance measurement experiments..... 130

Chapter 1
Introduction

An action potential reflects the change of a specific cell's membrane potential induced by the inputs from the neighboring environment. Unlike the skeletal muscle cells, nerve cells and cardiac cells can spontaneously generate action potentials and propagate these electrical signals by the opening and closure of ion channels realizing cell-to-cell communication. Due to this special property of these types of cells, various technologies have been developed to study and treat neurological diseases, relieve spinal pain, and restore regular heartbeats in both research and clinic. Nonetheless, the majority of work has focused on decoding the human brain which serves as the central organ of the human nervous system by in vivo electrical recording. The detected neural signal can be further filtered into two categories in different frequency bands, namely, the local field potential (<100 Hz) reflecting the synchronizing signal of a neural network and spikes (>250 Hz) generated from individual neurons or single units.[1-3] Therefore, it is essential to develop the technology that enables the electrical recording capability with spatial and temporal resolution.

Nonetheless, silent cells that are not capable of firing action potentials reply on the release, reuptake, and metabolism of specific molecules such as hormones, neurotransmitters, and cytokines for information exchange. Understanding the complex dynamics of these molecules requires advanced techniques to make these silent processes heard. Instead of using electrodes to record the endogenous electrical activities, people have utilized electrochemical techniques, mainly fast-scan cyclic voltammetry (FSCV), by applying a sweep of electrical stimulation via electrodes and recorded the resulting current to study the electrochemical properties of the extracellular environment. The working principle of FSCV follows by the rapid oxidation and reduction of the analyte molecules nearby the electrode and the measured voltammogram shape

can be used for biochemical molecule detection[4-6]. Similarly, Electrochemical Impedance Spectroscopy (EIS) has been applied as a diagnostic and monitoring tool to measure the bioimpedance of tissue samples or particular cells[7-9]. This approach enables real-time cell/tissue characterization based on the difference in their intrinsic electrical properties, providing information regarding tumorous/benign tissue differentiation and growth monitoring.

1.1 Existing electrical brain interface

Since the first in vivo electrophysiology recording using insulated metal microelectrodes in the 1950s, the past decade has witnessed the remarkable development of neural interfaces. The microfabrication techniques have permitted the revolutionary miniaturization and dense electrode packaging of the silicon-based neural probes[10-15]. In the meantime, many groups have conceived novel electrode techniques utilizing new materials or unprecedented fabrication methods for better biocompatibility or more functionality, many of which proved their unique device platform via in vivo neural recordings[16-23]. All these inventions have made it possible for the neuroscience community to access brain tissues in a 0D, 1D, 2D, or 3D fashion.

1.1.1 Electrical neural interface at a single site

Hubel's tungsten microelectrode has been the pioneered work for recording extracellular action potential in the cat brain[24], which led to the breakthrough in population recording using tetrodes[25-27]. Analyzing the recorded electrical signal from tetrodes using the triangulation method allows for the relative position of the firing neuron to the recording electrodes.

Due to the limitation imposed by the conventional metal wires as electrode materials, there exists a trade-off between the electrical property and the size of the electrode, leading to unfavorable biocompatibility and flexibility. To this end, microthread electrodes (MTEs) consisted

of 7-µm-diameter carbon-fiber in the center and biocompatible dielectric poly(p-xylylene)-based thin-film coating have realized the ultrasmall composite microelectrode with reduced chronic immune response and a subcellular cross-section (total size of ~ 8.5 µm in diameter)[17]. Poly(3,4-ethylenedioxythiophene)/poly(styrenesulphonate) (PEDOT:PSS) was further electrochemically deposited onto the recording site to facilitate the recording performance of in vivo cortical neural signals. Besides, polystyrene-polybutadiene(PS-b-PBD) insulated carbon nanotubes (CNT) fiber microelectrodes have demonstrated their advantageous electrical properties without organic electrically active coating[20]. The high surface area of CNT fibers has favored the electrode's charge storage capacity and charge injection limit leading to stable long-term neural recording over the course of several weeks while the stimulation efficacy of the CNT microelectrodes was validated in acute experiments. However, the precise implantation of such flexible material is usually assisted with the temporary stiffness increase of the electrode by shutter attachment or dissolvable hydrogel coating, yielding unnecessary tissue damage. Using a fluidic Microdrive technology, Vitale et al. have delivered their carbon nanotube-based microelectrodes to the targeted regions without an excess stiffening process.[21] This fluidic electrode delivery mechanism also precludes the injected fluid overpressure risk by venting away the excessive fluid.

Similar to the patch-clamp data acquisition mechanism, a hollow core has been incorporated within a tapered dual-core optical fiber with an end tip diameter of 6-20 µm enabling the study of the correlated relations between electrophysiological and optical signals with single-neuron resolution[18]. Inside the hollow core, a 1-3 M NaCl electrolyte solution has been selected to serve as the contacting media for acquiring the electrical activity where tungsten or stainless steel wire has been introduced for electric connection with the recording system. More recently, electrolyte-filled (3 M KCl) flexible quartz nanopipettes with an inner diameter of ~ 10-20 nm

have recorded intracellular action potentials by electroporation or complete tip insertion in awake behaving animals.[16] When interfacing with multiple cells, the low flux, and the vortex flow at the tip of the nanopipettes potentially prevent the debris blockage concern which has been a frequent issue in whole-cell patch-clamp.

1.1.2 Linear multi-electrode arrays

The fast development in the silicon-based electronics industry allows for the integration of multiple recording sites within a single probe. Silicon-based Michigan array has been created as the first neural probe that has the arrangement of the linear electrodes with micron-scale features.[15,28] By using the nanofabrication electron beam lithography (EBL) technique, the number of the passive electrodes in the single shank has increased by an order of magnitude (from ≥ 16 sites to up to 200 recording sites)[14]. A notable breakthrough was the incorporation of complementary metal-oxide-semiconductor (CMOS) technology into the Michigan-style probe, realizing large-scale active recording electrodes with multiplexing[10-14,29]. The Neuropixels probe was able to host 960 recording electrodes each with a size of 12 x 12 µm and was spaced with a center to center distance of 25 µm on a 70 µm x 20 µm and 10 mm long shank where 384 independent recording channels can be programmed to be active in between. Sharing the similar CMOS technology, NeuroSeeker probes managed a dense package of an even higher electrode count (1344 recording sites and 12 reference sites) on a 100 µm x 50 µm and 8 mm long shank where the recording and reference site measuring 20 µm x 20 µm and 20 µm x 80 µm, respectively.[13] By employing the time-division multiplexing and innovative circuit design techniques, the NeuroSeeker probe has succeeded in providing the highest electrode channel count, i.e. all the presented pixels along the probe length, that can actively record neural signals from a rat brain's neocortical, hippocampal, and thalamic regions simultaneously.

Meanwhile, the inevitable immune response caused by the mechanical mismatch between the rigid probes and brain tissue has drawn people's attention[30-32]. One straightforward strategy to overcome this inflammation is to build a bio-friendly interface between the electrode and brain tissue by coating alpha-MSH[33] or dexamethasone (DEX)[34]. By utilizing a special fish-bone probe geometry and a biodegradable silk polymer coating, the fish-bone-shaped polyimide neural probe aimed to distant the electrodes with large open areas while maintaining sufficient mechanical strength for implantation[35].

Even though the anti-inflammatory coatings have improved the biocompatibility of the silicon-based probes, the stress and pressure induced by the micromotion are still concerning[30,36,37]. Taking a step further, flexible materials have been incorporated into the linear neural probes as insulating substrates[38], such as polyimide[39], parylene C[40,41], and SU-8[19,31]. Ultraflexible nanoelectronic thread (NET) neural probes with insulating layers of SU-8 and electrodes of platinum or gold have been introduced by Luan and her colleagues.[19] The fabricated NET-50 and NET-10 hosted 8 and 4 electrodes in a linear layout featuring a cross-section of 50 μm x 1 μm and 10 μm x 1.5 μm, respectively. This remarkable reduction in probe size and bending stiffness yields much improved biocompatibility and the need for a shuttle device to ensure the precise delivery of the prove during implantation. 4 months single-unit recording results further validated the reliability of the NET probes.

1.1.3 Two-dimensional penetrating and flexible planar electrode array

The parallel arrangement of dense packed linear silicon-based probes has also increased one dimension to the previous linear penetrating configuration[42-46]. To gain better biocompatibility, the neural cell adhesion molecule L1 was introduced to four-shank NeuroNexus probes leading to an increased axonal density and decreased reaction of microglia and astrocytes

around the modified probe.[47] Notably, the first polyimide-based flexible two-dimensional intracortical electrode arrays have permitted chronic recording stability with flexibility and biocompatibility[48]. 8-shank, 64 electrodes, two-dimensional parylene-based neural probes with biocompatible silk fibroin coating also presented stable chronic recording capability over a course of 5 weeks and no observable device deterioration[49]. Inspired by the e-beam lithography technique for the close packing microelectrodes along the silicon-based probe, Wei et al. fabricated a densely packed nanoelectronic thread (NET-e) probe with adjustable patterns with a minimum 200 nm-wide interconnect traces[50]. The lateral distribution of this NET-e probe with 60 μm-intershank-spacing further increased the interfacing dimension for high-density neural mapping. Furthermore, in conjunction with multi-exposure speckle imaging (MESI), a four-shank NET array was implanted into the cortical region of the mouse brain to study the neurovascular relationship in a mouse of stroke-induced by localized photothrombosis[51].

As an alternative design for increasing the recording channel count in the neural probes, silicon-based multi-shank Utah arrays have been produced with a two-dimensional structure, serving as the first and only FDA-approved penetrating microelectrode array for long-term human-implanted brain-computer interface[52-54]. The Argo system bonded Utah-style probes (platinum-iridium microwire) with the CMOS amplifier array supporting the reported greatest simultaneous recording channels (65536) at 32 kHz and 12-bit resolution for in vivo studies.[55]

Additionally, to comply with the soft brain tissue forming a conformal contact, many noninvasive ECoG(electrocorticography)-type surface electrode arrays have been created with flexible substrates leading to better biocompatibility and recording performance, including flexible multiplexed electrode array, NeuroGrid, bioresorbable electrode array, stretchable electrode grids (SEG), Neural Matrix, etc[56-63].

By an integrative strategy of materials and fabrication process, Roger's group have developed planar flexible multielectrode arrays with distinct functionality. For example, a 360-channel flexible, high-resolution multiplexed electrode array exploited an active matrix circuit design with two nanomembrane transistors supporting each electrode with a size of 300 μm x 300 μm[56]. The fabricated active electrodes array was achieved using an integrated multi-layer fabrication process including the transfer printing of the structured doped silicon nanoribbons and photolithographic deposition of electrodes and interconnects encapsulated by polyimide substrate. Even the relatively large electrode lacked the spatial resolution for recording single-unit spiking activities, this large area (10 mm x 9 mm) cortical mapping of cat neural activity revealed spontaneous spindle oscillation under anesthesia, single-trial visual evoked responses upon light stimulus, and recurrent spiral waves during electrographic seizures. Latter, a high-throughput matrix electrode array, Neural Matrix, with 1008 actively multiplexed channels has addressed the challenges including the scaling-up capability, device stability, and system design for large-scale brain interfacing[59].

Moreover, the parylene-substrate NeuroGrid held 256 electrodes with a far reduced size (10 μm x 10 μm and 30 μm spacing) benefiting from the organic PEDOT:PSS coating[57]. This nonpenetrating subdural NeuroGrid array permitted the detection of LFPs and spiking activity with single-unit resolution from the cortical surface and the potential projection of the isolated single neuron from the simultaneously acquired recording featured by neighboring electrodes. To translate this ECoG array to human subjects, a relatively larger NeuroGrid array with coverage of either 420 mm^2 (120 electrodes) or 840 mm^2 (240 electrodes) was designed.[64] The electrodes within the parylene substrate were arranged in a tetrode-patterned layout with a 23 μm interelectrode spacing while the tetrodes were distributed at 2-mm intervals. This large-scale

NeuroGrid may assist and guide the procedures in undergoing surgeries with noninvasive monitoring of brain activities intraoperatively. Furthermore, 32 stretchable electrodes comprising of gold-coated titanium dioxide nanowires (Au-TiO_2NWs) facilitated by further electroplated platinum coating, were encapsulated in a PMDS substrate[60].

1.1.4 Neural probes with three-dimensional topological structure

It is also not surprising to see the integration of Michigan-style probe and Utah-style probe to achieve the dense three-dimensional interfacing structure[65-67]. In addition, a 1024-channel polymer electrode array was stacked by 16 (eight rows of two 64-channel arrays) modules where four 16-channel shanks were assembled[68]. Dense parallel microwire arrays were mated to a comprehensive CMOS amplifier chip by microwire bundling, exposing short sections of the metal electrodes, mechanical pressing to gain electrical bonding to the CMOS array, followed by the epoxy infiltration[69]. The alignment challenge of bonding the microwires and the CMOS pixels were overcome by adjusting the wire-spacing according to the active width of the pixel area. A relatively large number of the putative neurons were identified during acute in vivo recordings from deep cortical and subcortical regions of awake but restrained mice.

Neurotassel probe was drawn from a batch of molten tissue-dissolvable polyethylene glycol (PEG) inducing elastocapillary self-assembly with a cylindrical probe configuration where electrodes shared different depths[22]. With a likewise geometry, NeuroRoots electrodes constituting an array of 32 individual channels with a 7 μm x 1.5 μm lead cross-section and 10 μm-diameter tip platinum or PEDOT coated gold electrode pad[70]. Using a completely different electrode delivery approach, stent-electrode recording array (stentrode, with four 750 μm-diameter platinum electrodes attached to a commercially available self-expanding stent) was implanted into sensorimotor cortical vein assisted by catheter angiography[71].

Another unconventional delivery strategy of the recording system, three-dimensional mesh electrodes with minimal chronic immune response were administered by syringe injection or normal stereotaxical insertion of the pretreated frozen probe[72-74]. A total number of 19 electrodes made of either silicon nanowire field-effect transistors (FETs) or platinum were incorporated into the supporting arms where negative curvature was induced[74]. The 3D-cylindrical mesh structure was generated by the self-organization of the compressive strain applied to the original nanoelectronic 2D film with 80% porosity. The channel of the mesh electrodes was further scaled up to 128[72]. Inspired by the inherent shape of neurons, 16-channel neuron-like electronics (NeuE) with electrodes (8-20 μm) and interconnects (width of 1-4 μm) matching the geometry of soma and neurites were created with a much increased porosity(>99%)[75]. NeuE probes have demonstrated high-fidelity recording quality from acute to 3 months chronic measurements while the imaging data also suggested the possibility to favor the migration of newborn neurons.

More recently, the Neuralink array has drawn worldwide attention[76]. In this system, 96 individual polyimide-substrated threads that had 32 PEDOT:PSS or IrOx-coated gold electrodes each measuring 14 μm x 24 μm were inserted into the targeted brain regions by a temporary shuttle needle (tungsten-rhenium wire) via a robotic approach. Robotic systems were also equipped with six independent light illumination, stereoscopic cameras, and software-based depth-of-field calculations for guiding the whole insertion process and estimating the cortical location. The recent recording data demonstrated an implantation success rate of 90% and a maximum spiking yield of 70% using the customized online spike-detection software.

1.2 Delivery of electrochemical techniques

However, neuron is not the only cell type that consists of brain, where glial cells actively participate in brain signaling using chemicals and the employment of the electrodes is limited to

explore those silent signal transmissions that do not fire action potential. As an alternative approach to accessing to those biochemical activities, electrochemical techniques have been delivered via the implanted electrodes, decoding the complex dynamics with spatiotemporal resolution[4,77-79].

The principle of the electrochemical sensing has been well illustrated in previous reported reviews[7,80]. Here, we focus on the in vivo application of electrochemical techniques from device platform, the sensing methodology, and examined subjects perspectives.

1.2.1 Electrical detection of biomolecules

Amperometric sensors are a type of electrochemical device continuously recording the resulting current flow of an electroactive species in a biochemical oxidation or reduction process with applied potential[81]. One of the widely adopted amperometric technique is fast scan cyclic voltammetry (FSCV), which has been a sensitive approach to sense the electroactive biomolecules that can be oxidized and reduced such as dopamine, norepinephrine, epinephrine, serotonin, and histamine for the fast temporal resolution (< 100 ms)[4,78]. Another amperometric technique that holds a constant potential at the working electrode and measures the current generated by an oxidized or reduced electroactive species at the electrode surface, where enzyme is always introduced to facilitate the electrochemical process of non-electroactive biomarker like glucose, lactate, GABA, and glutamate[78,81].

Carbon-based electrode such as carbon fiber, carbon nanotubes (CNTs), CNT yarn microelectrodes, graphene, and nanodiamond, has been the first choice as an electrochemical electrode for decades due to its high electrical performance, chemical stability, and large surface area. PEDOT/CNT or PEDOT-graphene oxide (PEDOT-GO) has been coated to CNT and carbon fiber electrodes presenting an increased sensitivity of 500-fold and 880%, respectively. Nafion,

anionic functional groups, and ascorbic acid have also been applied to carbonfiber microelectrodes to increase the sensitivity and selectivity[78]. To improve the fabrication yield of the electrodes for electrochemical sensing, surface modified metal electrodes with organic coating have gradually been applied to the FSCV sensing field, while the relatively small potential window of bare metal electrodes limits their directly sensing capability. Coated by a semiconductor-based material (boron-doped nanodiamond film), tungsten electrode has shown improved electrochemical and mechanical characteristics compared to carbon fiber electrodes[82]. For those non-electroactive biomarkers that cannot be identified by conventional electrochemical detection methods, enzyme-based electrode has been developed where a set of immobilized membranes (permselective membrane, enzyme membrane, and diffusion limiting membrane) are crosslinked, entrapped, and electrodeposited onto the surface of the a metal or carbon based electrode[79].

In addition to the wires and fibers sensing platform, silicon, ceramic, and polymer have been selected to serve as the substrate of electrochemical sensing probes with a compact electrode arrangement. Frey et al. integrated two tip working electrodes and one Ag/AgCl reference electrode at a further behind location onto a silicon shank featuring 30-100 μm thickness, 100 μm width, and 6.5 mm in length for in vivo glutamate and choline sensing. Shaped by rectangular dicing and laser cutting, ceramic-based mironeedles have been developed with up to four working electrodes which can be specified to sense glutamate, lactate, choline, and acetylcholine. Incorporating thin-film and laminate technology, a flexible electrochemical sensor with polyimide substrate, two vapor-deposited platinum working electrode, and one Ag/AgCl reference electrode has been realized for glucose and lactate sensing while the enzyme was immobilized in n poly(hydroxyethyl methacrylate)-based (PHEMA) hydrogels.

1.2.2 Electrochemical impedance spectroscopy for tissue monitoring

In contrast to the sensing mechanism of oxidation and reduction in the FSCV and amperometric sensing, the electrochemical impedance spectroscopy (EIS) spectrum records the changes of the electrical conductivity of the working electrode, which will be largely influenced by the analyte composition with no selectivity. As biological tissues share different structures, compositions, and health conditions, with different materials at diverse concentration composing their intracellular fluids, cell membranes, and extracellular matrix, the response to the applied AC signal will vary[9,83,84]. Attributed to the low cost, simplicity, and real-time measurements capability, the EIS has been applied in many healthy organs such as, brain, skin, heart, etc. as well as tumors for diagnostic purposes in vivo.

The most commonly application of EIS for the neuroscience community is to validate the electrical properties of the implanted electrodes for recording or stimulation before the surgery. A few studies reported the followed-up monitoring of the implanted device as a method to assess the stability of the electrical interfaces with the temporal profile of surrounding cells and proteins. Lempka et al., collected impedance results of the implanted deep brain stimulation electrodes before, immediately after and periodically after implantation in the brain of a rhesus macaque monkey[85]. They found out a significant increase of the measured impedance followed by a reverse change through electrical stimulation. Similarly, Williams et al. focused on performing EIS for assessing the changes of neural tissue brough from the foreign implanted probes, which was investigated by standard immunohistochemistry analysis[86]. In general, the changes in impedance measurements correlated well to the cellular distribution around implanted electrode.

Since tumor tissue usually consumes relatively large portion of blood, therefore, tumorous structure can be distinguished from the surrounding benign tissue by their relatively lower

impedance. In normal clinical testing, tissue sample have to be dissected without the accurate information regarding the targeted location during the biopsy process. To solve this issue, bioimpedance measurements have been incorporated into a biopsy needle, providing an accurate approach to identify the tumorous tissue with high spatial resolution[87]. In order to prevent an electrode plorization effect which is highly possible to occur in a two-electrode measurement system, an EIS microelectrode array at a micron scale was integrated with the biopsy needle, improving the accuracy of the application tumorous tissue with relatively small sizes[88].

In a more macroscopic aspect, bioimpedance has been extensively used in assessing the skin hydration level, cardiac output, and body composition. Assisted by the electrical impedance technique reflecting the skin impedance change, skin hydration dynamics have been investigated regarding the transdermal drug delivery[89]. To eliminate the variability and unrepeatability from contact electrodes, fiber bragg gratings have been embedded in a impedance measurement system for force and temperature calibration[90]. Far larger gel electrodes, capacitive electrodes, textile electrodes have been used to perform the bioimpedance measurements on human body for a larger current injection and voltage detection. Modulated by cardiorespiratory events, impedance change can reflect the change of blood flow as the blood flow increase, the corresponding impedance will decrease. Using similar strategy, body composition can be estimated in terms of the percentages of water, protein, fat, minerals, and carbohydrate[84].

1.3 Multimaterial multifunctional fiber

The first multimaterial multifunctional fiber-based neural probe was developed by the Anikeeva and Fink groups at MIT.[23] These fibers, fabricated using the multimaterial fiber drawing method, are capable of simultaneous *in vivo* optical stimulation, electrical recording, and drug delivery[23]. To achieve proper impedance matching for reliable electrical recording with high

signal-to-noise ratio, low melting point metal materials (e.g. Sn, BiSn) are the first choice due to their high electrical conductivity and compatibility with polymer fiber drawing process. Using a two-step fiber drawing process, fiber probes with 7-36 tin electrodes inside a polyetherimide (PEI) cladding were produced. The electrode size is less than 10 μm, and the overall probe size can be as small as 85 μm in diameter after etching the outer sacrificial layer. To enable simultaneous optical transmission and electrical recording, PC/COC core/shell structures were used to create the optical waveguides due to their large refractive index difference, and carbon-loaded polyethylene (CPE) was used as the recording electrodes. These fibers were implanted into the medial prefrontal cortex of transgenic mice (Thy1-ChR2-YFP). Optically-triggered neural activities were recorded using a single implanted device. These polymer-based fiber probes are much more flexible compared to silica fibers, with a bending stiffness as low as 4-7 N/m. Besides, they are also biocompatible, resulting in minimal tissue responses after being implanted in the mice brain for three months.[23]

Nevertheless, due to the low electrical conductivity of CPE, the size of CPE electrodes has to be large in order to have the overall impedance fall in the recording range, resulting in a poor spatial resolution of these probes. To overcome this challenge, many efforts have been made. Carbon nanofibers (CNFs) were introduced into the conventional CPE electrodes. During the thermal drawing process, unidirectional alignment of CNFs was achieved, resulting in drastically increased conductivity along the fiber longitudinal direction. Therefore, the electrode sizes can be reduced significantly without sacrificing the recording signal quality.[91] Similarly, graphite was employed into CPE to increase the electrical conductivity of the electrodes and improve the spatial resolution in a multifunctional fiber probe.[92]

Beyond brain interfacing, multimaterial multifunctional fibers are also ideal candidates for probing the spinal cord due to the mechanical compliance of these fibers. They have been used for optogenetic stimulation and electrical recording in the spinal cord of live animals.[93] To further enhance the mechanical performance, stretchable fibers have also been developed for simultaneous optical stimulation and electrical recording in the spinal cord.[94] The stretchable waveguide consists of COC elastomer (COCE, n = 1.51) as the core material and polydimethylsiloxane (PDMS, n = ~1.41 to 1.47) as the cladding. The electrical interface was created by dip coating conductive silver nanowires (AgNWs) onto the fiber surface. The mesh electrode of AgNWs was more resilient to bending and stretch deformation compared to conventional electrodes.

Chemical delivery, combined with electrical and optical interfaces, can offer additional control over the neural activities providing insights to neurological diseases.[95,96] Intracranial drug or viral factor delivery typically utilizes cannulas (metal tubes) or needles. Researchers have also developed a method of employing fiber guided cannula as the drug delivery channel.[97] However, integrating chemical delivery channels with electrical and optical fibers has been a challenge. To address this issue, Xie's group developed multifunctional neural probes by conformal attachment of nanoelectronic coating devices to the surface of a glass pipet[98], while other groups integrated microfluidic channels in the neural recording device using MEMS or microcontact printing fabrication methods.[96,99] These technologies involve multiple fabrication steps, and may introduce difficulty in scaling up to multiple channels. On the other hand, the multimaterial fiber drawing method can be adopted to scalably produce multifunctional probes with electrical, optical and chemical delivery functionalities.[23] Synaptic blockers cyanquixaline (CNQX) was infused into the brain region of interest via microfluidic channels inside the multifunctional fiber probe, and drug modulated neural activity was detected using the fiber electrodes under optical stimulation. This

multifunctional fiber probe with simultaneous electrical recording, optical stimulation, and drug delivery capabilities also enables optogenetics experiments in wild-type (non-transgenic) animals using a single-step surgery.[92] Traditionally, to conduct optogenetic experiments in wild-type animals, one needs to perform a first surgery during which viral vectors containing opsin genes are injected to a targeted brain region. After the gene expresses opsins in a few weeks, a second surgery is performed to implant the optical fiber and electrodes to the injection site for optogenetic stimulation and recording. A miniaturized multifunctional fiber probe with integrated microfluidic channels, optical waveguide, and microelectrodes can perform virus injection, optogenetic stimulation and recording in a freely behaving mouse with one-step surgery, minimizing the tissue damage and experimental challenges. This technology, combined with wireless communication and micropump technologies, can also open new opportunities in closed-loop systems for disease intervention and treatment.

The versatility in the design and fabrication of multimaterial fibers makes them advantageous for tissue engineering applications. Hollow-core fibers with various channel geometries were fabricated and used for nerve axonal guidance. Rectangular cores with microgrooves were shown to have superior nerve axonal guiding properties compared with other geometries[100]. Furthermore, to enhance the media exchange and oxygen flow across the scaffold for improved neurite outgrowth and cell survival, porous fiber scaffolds were produced using phase separation during the fiber drawing.[101] More recently, a porous fiber scaffold was developed using salt-leaching method after the fiber was drawn.[102] This fiber was also fused into a 3D printing system to create multichannel microporous scaffolds at centimeter scales. The 3D printing of porous fibers shows great promise for repairing injured spinal cord. In addition to geometrical guidance, many other methods have been shown to be effective in promoting neurite growth, such

as growth factor delivery[103], electrical stimulation[104], optogenetic stimulation, and the application of electric fields[105], all of which can potentially be adopted into a multimaterial fiber scaffold. Besides, simultaneous electrical recording can be used for monitoring the progress of nerve growth[106,107]. In the future, multimaterial scaffolding fibers with added electrical and optical modalities can provide an effective and scalable platform for nerve repair and regeneration.

1.4 Scope and organization

Despite the straightforward thermal-drawing fabrication method of integrating multimodal functionalities within a single device, multisite interfacing is still a big challenge in fiber-based neural interfaces compared with MEMS fabricated silicon devices. Surface patterning methods for creating multiple interface sites along the fiber surface is yet to be be developed. This can significantly enhance the applications of fiber-based neural interface devices.

Besides, there are few attempts for exploiting the multimaterial fiber probes in any disease models for either monitoring or treatment. Taking advantages of the electrical, optical, and fluidic properties of the fiber probes can potentially elucidate fundamentals regarding cell/tissue's inherent properties and facilitate the development of disease treatments. In light of the convergence fiber drawing method that overcomes the limitation of choosing materials that can be incorporated in the functional fiber, fiber technology for bio-related studies can be greatly enhanced.

Chapter 2 to Chapter 5 describe several recent developed platforms of integrating functional fibers with new modalities as well as applications in different scenarios, including the spatially expandable fiber-based probes as a multifunctional deep brain interface, nano-optoelectrodes integrated with flexible multifunctional fiber probes by high-throughput scalable fabrication, 3D bioprinting using hollow multifunctional fiber impedimetric sensors, and implantable optical fibers for delivering immunotherapies and tumor impedance measurement.

Chapter 6 will conclude the research achievements introduced from Chapter 2 to Chapter 5 and the outlook for future direction.

1.5 References

1 Buzsaki, G. Large-scale recording of neuronal ensembles. *Nat Neurosci* **7**, 446-451, doi:10.1038/nn1233 (2004).

2 Buzsaki, G., Anastassiou, C. A. & Koch, C. The origin of extracellular fields and currents--EEG, ECoG, LFP and spikes. *Nat Rev Neurosci* **13**, 407-420, doi:10.1038/nrn3241 (2012).

3 Hong, G. & Lieber, C. M. Novel electrode technologies for neural recordings. *Nature reviews. Neuroscience* **20**, 330-345, doi:10.1038/s41583-019-0140-6 (2019).

4 Frank, J. A., Antonini, M. J. & Anikeeva, P. Next-generation interfaces for studying neural function. *Nat Biotechnol* **37**, 1013-1023, doi:10.1038/s41587-019-0198-8 (2019).

5 Roberts, J. G. & Sombers, L. A. Fast-Scan Cyclic Voltammetry: Chemical Sensing in the Brain and Beyond. *Anal Chem* **90**, 490-504, doi:10.1021/acs.analchem.7b04732 (2018).

6 Puthongkham, P. & Venton, B. J. Recent advances in fast-scan cyclic voltammetry. *Analyst* **145**, 1087-1102, doi:10.1039/c9an01925a (2020).

7 Dziąbowska, K., Czaczyk, E. & Nidzworski, D. Application of electrochemical methods in biosensing technologies. *Biosens. Technol. Detect. Pathog. A Prosp. Way Rapid Anal* (2018).

8 Lisdat, F. & Schafer, D. The use of electrochemical impedance spectroscopy for biosensing. *Anal Bioanal Chem* **391**, 1555-1567, doi:10.1007/s00216-008-1970-7 (2008).

9 Krukiewicz, K. Electrochemical impedance spectroscopy as a versatile tool for the characterization of neural tissue: A mini review. *Electrochemistry Communications* **116**, 106742, doi:https://doi.org/10.1016/j.elecom.2020.106742 (2020).

10 Herbawi, A. S. *et al.* CMOS Neural Probe With 1600 Close-Packed Recording Sites and 32 Analog Output Channels. *J Microelectromech S* **27**, 1023-1034, doi:10.1109/Jmems.2018.2872619 (2018).

11 Jun, J. J. *et al.* Fully integrated silicon probes for high-density recording of neural activity. *Nature* **551**, 232-236, doi:10.1038/nature24636 (2017).

12 Lopez, C. M. *et al.* An Implantable 455-Active-Electrode 52-Channel CMOS Neural Probe. *Isscc Dig Tech Pap I* **56**, 288-+ (2013).

13 Raducanu, B. C. *et al.* Time Multiplexed Active Neural Probe with 1356 Parallel Recording Sites. *Sensors (Basel)* **17**, doi:10.3390/s17102388 (2017).

14 Scholvin, J. *et al.* Close-Packed Silicon Microelectrodes for Scalable Spatially Oversampled Neural Recording. *IEEE Trans Biomed Eng* **63**, 120-130, doi:10.1109/TBME.2015.2406113 (2016).

15 Steinmetz, N. A., Koch, C., Harris, K. D. & Carandini, M. Challenges and opportunities for large-scale electrophysiology with Neuropixels probes. *Curr Opin Neurobiol* **50**, 92-100, doi:10.1016/j.conb.2018.01.009 (2018).

16 Jayant, K. *et al.* Flexible Nanopipettes for Minimally Invasive Intracellular Electrophysiology In Vivo. *Cell Rep* **26**, 266-278 e265, doi:10.1016/j.celrep.2018.12.019 (2019).

17 Kozai, T. D. *et al.* Ultrasmall implantable composite microelectrodes with bioactive surfaces for chronic neural interfaces. *Nat Mater* **11**, 1065-1073, doi:10.1038/nmat3468 (2012).

18 LeChasseur, Y. *et al.* A microprobe for parallel optical and electrical recordings from single neurons in vivo. *Nat Methods* **8**, 319-325, doi:10.1038/nmeth.1572 (2011).

19 Luan, L. *et al.* Ultraflexible nanoelectronic probes form reliable, glial scar-free neural integration. *Sci Adv* **3**, e1601966, doi:10.1126/sciadv.1601966 (2017).
20 Vitale, F., Summerson, S. R., Aazhang, B., Kemere, C. & Pasquali, M. Neural stimulation and recording with bidirectional, soft carbon nanotube fiber microelectrodes. *ACS Nano* **9**, 4465-4474, doi:10.1021/acsnano.5b01060 (2015).
21 Vitale, F. *et al.* Fluidic Microactuation of Flexible Electrodes for Neural Recording. *Nano Lett* **18**, 326-335, doi:10.1021/acs.nanolett.7b04184 (2018).
22 Guan, S. *et al.* Elastocapillary self-assembled neurotassels for stable neural activity recordings. *Science Advances* **5**, doi:10.1126/sciadv.aav2842 (2019).
23 Canales, A. *et al.* Multifunctional fibers for simultaneous optical, electrical and chemical interrogation of neural circuits in vivo. *Nat Biotechnol* **33**, 277-+, doi:10.1038/nbt.3093 (2015).
24 Hubel, D. H. & Wiesel, T. N. Receptive fields of single neurones in the cat's striate cortex. *J Physiol* **148**, 574-591, doi:10.1113/jphysiol.1959.sp006308 (1959).
25 Mcnaughton, B. L., Barnes, C. A. & Okeefe, J. The Contributions of Position, Direction, and Velocity to Single Unit-Activity in the Hippocampus of Freely-Moving Rats. *Exp Brain Res* **52**, 41-49 (1983).
26 Gray, C. M., Maldonado, P. E., Wilson, M. & McNaughton, B. Tetrodes markedly improve the reliability and yield of multiple single-unit isolation from multi-unit recordings in cat striate cortex. *Journal of Neuroscience Methods* **63**, 43-54, doi:https://doi.org/10.1016/0165-0270(95)00085-2 (1995).
27 Voigts, J., Siegle, J. H., Pritchett, D. L. & Moore, C. L. The flexDrive: an ultra-light implant for optical control and highly parallel chronic recording of neuronal ensembles in freely moving mice. *Front Syst Neurosci* **7**, doi:10.3389/fnsys.2013.00008 (2013).
28 Wise, K. D., Angell, J. B. & Starr, A. An Integrated-Circuit Approach to Extracellular Microelectrodes. *Ieee T Bio-Med Eng* **Bm17**, 238-+, doi:Doi 10.1109/Tbme.1970.4502738 (1970).
29 Du, J., Blanche, T. J., Harrison, R. R., Lester, H. A. & Masmanidis, S. C. Multiplexed, high density electrophysiology with nanofabricated neural probes. *PLoS One* **6**, e26204, doi:10.1371/journal.pone.0026204 (2011).
30 Feiner, R. & Dvir, T. Tissue-electronics interfaces: from implantable devices to engineered tissues. *Nature Reviews Materials* **3**, doi:10.1038/natrevmats.2017.76 (2018).
31 He, F., Lycke, R., Ganji, M., Xie, C. & Luan, L. Review Ultraflexible Neural Electrodes for Long-Lasting Intracortical Recording. *Iscience* **23**, doi:10.1016/j.isci.2020.101387 (2020).
32 Salatino, J. W., Ludwig, K. A., Kozai, T. D. Y. & Purcell, E. K. Glial responses to implanted electrodes in the brain. *Nat Biomed Eng* **1**, 862-877, doi:10.1038/s41551-017-0154-1 (2017).
33 He, W., McConnell, G. C., Schneider, T. M. & Bellamkonda, R. V. A novel anti-inflammatory surface for neural electrodes. *Adv Mater* **19**, 3529-+, doi:10.1002/adma.200700943 (2007).
34 Zhong, Y. & Bellamkonda, R. V. Dexamethasone-coated neural probes elicit attenuated inflammatory response and neuronal loss compared to uncoated neural probes. *Brain Res* **1148**, 15-27, doi:10.1016/j.brainres.2007.02.024 (2007).
35 Wu, F., Im, M. & Yoon, E. in *2011 16th International Solid-State Sensors, Actuators and Microsystems Conference.* 966-969.

36 Someya, T., Bao, Z. & Malliaras, G. G. The rise of plastic bioelectronics. *Nature* **540**, 379-385, doi:10.1038/nature21004 (2016).

37 Jeong, J. W. *et al.* Soft materials in neuroengineering for hard problems in neuroscience. *Neuron* **86**, 175-186, doi:10.1016/j.neuron.2014.12.035 (2015).

38 Weltman, A., Yoo, J. & Meng, E. Flexible, Penetrating Brain Probes Enabled by Advances in Polymer Microfabrication. *Micromachines (Basel)* **7**, doi:10.3390/mi7100180 (2016).

39 Mercanzini, A. *et al.* Demonstration of cortical recording using novel flexible polymer neural probes. *Sensor Actuat a-Phys* **143**, 90-96, doi:10.1016/j.sna.2007.07.027 (2008).

40 Xu, H. *et al.* Acute in vivo testing of a conformal polymer microelectrode array for multi-region hippocampal recordings. *J Neural Eng* **15**, 016017, doi:10.1088/1741-2552/aa9451 (2018).

41 Williamson, A. *et al.* Localized Neuron Stimulation with Organic Electrochemical Transistors on Delaminating Depth Probes. *Adv Mater* **27**, 4405-4410, doi:10.1002/adma.201500218 (2015).

42 Angotzi, G. N. *et al.* A Synchronous Neural Recording Platform for Multiple High-Resolution CMOS Probes and Passive Electrode Arrays. *IEEE Trans Biomed Circuits Syst* **12**, 532-542, doi:10.1109/TBCAS.2018.2792046 (2018).

43 Berenyi, A. *et al.* Large-scale, high-density (up to 512 channels) recording of local circuits in behaving animals. *J Neurophysiol* **111**, 1132-1149, doi:10.1152/jn.00785.2013 (2014).

44 Boi, F. *et al.* Multi-shanks SiNAPS Active Pixel Sensor CMOS probe: 1024 simultaneously recording channels for high-density intracortical brain mapping. *bioRxiv*, 749911, doi:10.1101/749911 (2020).

45 Fiath, R. *et al.* Large-scale recording of thalamocortical circuits: in vivo electrophysiology with the two-dimensional electronic depth control silicon probe. *J Neurophysiol* **116**, 2312-2330, doi:10.1152/jn.00318.2016 (2016).

46 Torfs, T. *et al.* Two-dimensional multi-channel neural probes with electronic depth control. *IEEE Trans Biomed Circuits Syst* **5**, 403-412, doi:10.1109/TBCAS.2011.2162840 (2011).

47 Azemi, E., Lagenaur, C. F. & Cui, X. T. The surface immobilization of the neural adhesion molecule L1 on neural probes and its effect on neuronal density and gliosis at the probe/tissue interface. *Biomaterials* **32**, 681-692, doi:https://doi.org/10.1016/j.biomaterials.2010.09.033 (2011).

48 Rousche, P. J. *et al.* Flexible polyimide-based intracortical electrode arrays with bioactive capability. *IEEE Trans Biomed Eng* **48**, 361-371, doi:10.1109/10.914800 (2001).

49 Wu, F. *et al.* in *2013 Transducers & Eurosensors XXVII: The 17th International Conference on Solid-State Sensors, Actuators and Microsystems (TRANSDUCERS & EUROSENSORS XXVII).* 888-891.

50 Wei, X. *et al.* Nanofabricated Ultraflexible Electrode Arrays for High-Density Intracortical Recording. *Adv Sci (Weinh)* **5**, 1700625, doi:10.1002/advs.201700625 (2018).

51 He, F. *et al.* Multimodal mapping of neural activity and cerebral blood flow reveals long-lasting neurovascular dissociations after small-scale strokes. *Sci Adv* **6**, eaba1933, doi:10.1126/sciadv.aba1933 (2020).

52 Campbell, P. K., Jones, K. E. & Normann, R. A. A 100 electrode intracortical array: structural variability. *Biomed Sci Instrum* **26**, 161-165 (1990).

53 Fernandez, E. *et al.* Acute human brain responses to intracortical microelectrode arrays: challenges and future prospects. *Front Neuroeng* **7**, 24, doi:10.3389/fneng.2014.00024 (2014).

54 Rousche, P. J. & Normann, R. A. Chronic recording capability of the Utah Intracortical Electrode Array in cat sensory cortex. *J Neurosci Methods* **82**, 1-15, doi:10.1016/s0165-0270(98)00031-4 (1998).
55 Sahasrabuddhe, K. *et al.* The Argo: a high channel count recording system for neural recording in vivo. *J Neural Eng* **18**, 015002, doi:10.1088/1741-2552/abd0ce (2021).
56 Viventi, J. *et al.* Flexible, foldable, actively multiplexed, high-density electrode array for mapping brain activity in vivo. *Nat Neurosci* **14**, 1599-1605, doi:10.1038/nn.2973 (2011).
57 Khodagholy, D. *et al.* NeuroGrid: recording action potentials from the surface of the brain. *Nat Neurosci* **18**, 310-315, doi:10.1038/nn.3905 (2015).
58 Yu, K. J. *et al.* Bioresorbable silicon electronics for transient spatiotemporal mapping of electrical activity from the cerebral cortex. *Nat Mater* **15**, 782-791, doi:10.1038/nmat4624 (2016).
59 Chiang, C. H. *et al.* Development of a neural interface for high-definition, long-term recording in rodents and nonhuman primates. *Sci Transl Med* **12**, doi:10.1126/scitranslmed.aay4682 (2020).
60 Tybrandt, K. *et al.* High-Density Stretchable Electrode Grids for Chronic Neural Recording. *Adv Mater* **30**, e1706520, doi:10.1002/adma.201706520 (2018).
61 Lee, K. Y. *et al.* Development of a Polydimethylsiloxane-Based Electrode Array for Electrocorticography. *Adv Mater Interfaces* **7**, doi:10.1002/admi.202001152 (2020).
62 Kim, D. H. *et al.* Dissolvable films of silk fibroin for ultrathin conformal bio-integrated electronics. *Nat Mater* **9**, 511-517, doi:10.1038/nmat2745 (2010).
63 Kim, D. H. *et al.* Epidermal electronics. *Science* **333**, 838-843, doi:10.1126/science.1206157 (2011).
64 Khodagholy, D. *et al.* Organic electronics for high-resolution electrocorticography of the human brain. *Sci Adv* **2**, e1601027, doi:10.1126/sciadv.1601027 (2016).
65 Cheng, M. Y. *et al.* 3D probe array integrated with a front-end 100-channel neural recording ASIC. *J Micromech Microeng* **24**, doi:10.1088/0960-1317/24/12/125010 (2014).
66 Shobe, J. L., Claar, L. D., Parhami, S., Bakhurin, K. I. & Masmanidis, S. C. Brain activity mapping at multiple scales with silicon microprobes containing 1,024 electrodes. *Journal of Neurophysiology* **114**, 2043-2052, doi:10.1152/jn.00464.2015 (2015).
67 Rios, G., Lubenov, E. V., Chi, D., Roukes, M. L. & Siapas, A. G. Nanofabricated Neural Probes for Dense 3-D Recordings of Brain Activity. *Nano Lett* **16**, 6857-6862, doi:10.1021/acs.nanolett.6b02673 (2016).
68 Chung, J. E. *et al.* High-Density, Long-Lasting, and Multi-region Electrophysiological Recordings Using Polymer Electrode Arrays. *Neuron* **101**, 21-+, doi:10.1016/j.neuron.2018.11.002 (2019).
69 Obaid, A. *et al.* Massively parallel microwire arrays integrated with CMOS chips for neural recording. *Science Advances* **6**, doi:10.1126/sciadv.aay2789 (2020).
70 Ferro, M. D. *et al.* NeuroRoots, a bio-inspired, seamless Brain Machine Interface device for long-term recording. *bioRxiv*, 460949, doi:10.1101/460949 (2018).
71 Oxley, T. J. *et al.* Minimally invasive endovascular stent-electrode array for high-fidelity, chronic recordings of cortical neural activity. *Nat Biotechnol* **34**, 320-+, doi:10.1038/nbt.3428 (2016).
72 Fu, T. M., Hong, G., Viveros, R. D., Zhou, T. & Lieber, C. M. Highly scalable multichannel mesh electronics for stable chronic brain electrophysiology. *Proc Natl Acad Sci U S A* **114**, E10046-E10055, doi:10.1073/pnas.1717695114 (2017).

73 Zhou, T. *et al.* Syringe-injectable mesh electronics integrate seamlessly with minimal chronic immune response in the brain. *Proc Natl Acad Sci U S A* **114**, 5894-5899, doi:10.1073/pnas.1705509114 (2017).

74 Xie, C. *et al.* Three-dimensional macroporous nanoelectronic networks as minimally invasive brain probes. *Nature Materials* **14**, 1286-1292, doi:10.1038/Nmat4427 (2015).

75 Yang, X. *et al.* Bioinspired neuron-like electronics. *Nature Materials* **18**, 510-+, doi:10.1038/s41563-019-0292-9 (2019).

76 Musk, E. & Neuralink. An Integrated Brain-Machine Interface Platform With Thousands of Channels. *J Med Internet Res* **21**, e16194, doi:10.2196/16194 (2019).

77 Stradiotto, N. R., Yamanaka, H. & Zanoni, M. V. B. Electrochemical sensors: A powerful tool in analytical chemistry. *J Brazil Chem Soc* **14**, 159-173, doi:Doi 10.1590/S0103-50532003000200003 (2003).

78 Robinson, D. L., Hermans, A., Seipel, A. T. & Wightman, R. M. Monitoring rapid chemical communication in the brain. *Chem Rev* **108**, 2554-2584, doi:10.1021/cr068081q (2008).

79 Tan, C., Robbins, E. M., Wu, B. C. & Cui, X. T. Recent Advances in In Vivo Neurochemical Monitoring. *Micromachines-Basel* **12**, doi:10.3390/mi12020208 (2021).

80 Rezaei, B. & Irannejad, N. in *Electrochemical Biosensors* (ed Ali A. Ensafi) 11-43 (Elsevier, 2019).

81 Grieshaber, D., MacKenzie, R., Voros, J. & Reimhult, E. Electrochemical biosensors - Sensor principles and architectures. *Sensors-Basel* **8**, 1400-1458, doi:DOI 10.3390/s8031400 (2008).

82 Bennet, K. E. *et al.* A Diamond-Based Electrode for Detection of Neurochemicals in the Human Brain. *Front Hum Neurosci* **10**, 102, doi:10.3389/fnhum.2016.00102 (2016).

83 Naranjo-Hernandez, D., Reina-Tosina, J. & Min, M. Fundamentals, Recent Advances, and Future Challenges in Bioimpedance Devices for Healthcare Applications. *J Sensors* **2019**, doi:10.1155/2019/9210258 (2019).

84 Bera, T. K. Bioelectrical Impedance Methods for Noninvasive Health Monitoring: A Review. *J Med Eng* **2014**, 381251, doi:10.1155/2014/381251 (2014).

85 Koutsouras, D. A. *et al.* Simultaneous monitoring of single cell and of micro-organ activity by PEDOT:PSS covered multi-electrode arrays. *Mat Sci Eng C-Mater* **81**, 84-89, doi:10.1016/j.msec.2017.07.028 (2017).

86 Williams, J. C., Hippensteel, J. A., Dilgen, J., Shain, W. & Kipke, D. R. Complex impedance spectroscopy for monitoring tissue responses to inserted neural implants. *Journal of Neural Engineering* **4**, 410-423, doi:10.1088/1741-2560/4/4/007 (2007).

87 Halonen, S., Kari, J., Ahonen, P., Kronstrom, K. & Hyttinen, J. Real-Time Bioimpedance-Based Biopsy Needle Can Identify Tissue Type with High Spatial Accuracy. *Ann Biomed Eng* **47**, 836-851, doi:10.1007/s10439-018-02187-9 (2019).

88 Park, J. *et al.* Biopsy Needle Integrated with Electrical Impedance Sensing Microelectrode Array towards Real-time Needle Guidance and Tissue Discrimination. *Sci Rep-Uk* **8**, doi:10.1038/s41598-017-18360-4 (2018).

89 Morin, M. *et al.* Skin hydration dynamics investigated by electrical impedance techniques in vivo and in vitro. *Sci Rep* **10**, 17218, doi:10.1038/s41598-020-73684-y (2020).

90 Ruiz-Vargas, A., Ivorra, A. & Arkwright, J. W. Design, Construction and Validation of an Electrical Impedance Probe with Contact Force and Temperature Sensors Suitable for in-vivo Measurements. *Sci Rep* **8**, 14818, doi:10.1038/s41598-018-33221-4 (2018).

91 Guo, Y. Y. *et al.* Polymer Composite with Carbon Nanofibers Aligned during Thermal Drawing as a Microelectrode for Chronic Neural Interfaces. *Acs Nano* **11**, 6574-6585, doi:10.1021/acsnano.6b07550 (2017).
92 Park, S. *et al.* One-step optogenetics with multifunctional flexible polymer fibers. *Nat Neurosci* **20**, 612-+, doi:10.1038/nn.4510 (2017).
93 Lu, C. *et al.* Polymer Fiber Probes Enable Optical Control of Spinal Cord and Muscle Function In Vivo. *Advanced Functional Materials* **24**, 6594-6600, doi:10.1002/adfm.201401266 (2014).
94 Lu, C. *et al.* Flexible and stretchable nanowire-coated fibers for optoelectronic probing of spinal cord circuits. *Sci Adv* **3**, e1600955, doi:10.1126/sciadv.1600955 (2017).
95 Dagdeviren, C. *et al.* Miniaturized neural system for chronic, local intracerebral drug delivery. *Sci Transl Med* **10**, doi:10.1126/scitranslmed.aan2742 (2018).
96 Jeong, J. W. *et al.* Wireless Optofluidic Systems for Programmable In Vivo Pharmacology and Optogenetics. *Cell* **162**, 662-674, doi:10.1016/j.cell.2015.06.058 (2015).
97 Aravanis, A. M. *et al.* An optical neural interface: in vivo control of rodent motor cortex with integrated fiberoptic and optogenetic technology. *J Neural Eng* **4**, S143-S156, doi:10.1088/1741-2560/4/3/S02 (2007).
98 Zhao, Z. T. *et al.* Nanoelectronic Coating Enabled Versatile Multifunctional Neural Probes. *Nano Lett* **17**, 4588-4595, doi:10.1021/acs.nanolett.7b00956 (2017).
99 Lee, H. J. *et al.* A multichannel neural probe with embedded microfluidic channels for simultaneous in vivo neural recording and drug delivery. *Lab Chip* **15**, 1590-1597, doi:10.1039/c4lc01321b (2015).
100 Koppes, R. A. *et al.* Thermally drawn fibers as nerve guidance scaffolds. *Biomaterials* **81**, 27-35, doi:10.1016/j.biomaterials.2015.11.063 (2016).
101 Grena, B. *et al.* Thermally-drawn fibers with spatially-selective porous domains. *Nat Commun* **8**, doi:10.1038/s41467-017-00375-0 (2017).
102 Shahriari, D. *et al.* Scalable Fabrication of Porous Microchannel Nerve Guidance Scaffolds with Complex Geometries. *Adv Mater* **31**, e1902021, doi:10.1002/adma.201902021 (2019).
103 Ikeda, M. *et al.* Acceleration of peripheral nerve regeneration using nerve conduits in combination with induced pluripotent stem cell technology and a basic fibroblast growth factor drug delivery system. *J Biomed Mater Res A* **102**, 1370-1378, doi:10.1002/jbm.a.34816 (2014).
104 Al-Majed, A. A., Tam, S. L. & Gordon, T. Electrical stimulation accelerates and enhances expression of regeneration-associated genes in regenerating rat femoral motoneurons. *Cell Mol Neurobiol* **24**, 379-402, doi:DOI 10.1023/B:CEMN.0000022770.66463.f7 (2004).
105 Thompson, D. M., Koppes, A. N., Hardy, J. G. & Schmidt, C. E. Electrical Stimuli in the Central Nervous System Microenvironment. *Annu Rev Biomed Eng* **16**, 397-430, doi:10.1146/annurev-bioeng-121813-120655 (2014).
106 Musick, K. M. *et al.* Chronic multichannel neural recordings from soft regenerative microchannel electrodes during gait. *Sci Rep-Uk* **5**, doi:10.1038/srep14363 (2015).
107 Rodriguez, F. J. *et al.* Polyimide cuff electrodes for peripheral nerve stimulation. *J Neurosci Meth* **98**, 105-118, doi:Doi 10.1016/S0165-0270(00)00192-8 (2000).

Chapter 2
Spatially expandable fiber-based probes as a multifunctional deep brain interface

2.1 Introduction

Implantable neural interface devices at a single-unit resolution play an indispensable role in understanding the functional networks in the brain and treating neurological diseases1-9. Over the past decades, significant progress has been made in developing highly multiplexed, flexible, and biocompatible neural probes with a single unit resolution for chronic implantation10-17. Despite the recent achievement of high resolution and high channel count in these devices10,18-23, it remains a major challenge to develop a seamless interface that can map three-dimensional (3D) brain activity across distant regions in the deep brain while minimizing the tissue damage.

At present, indirect methods such as fMRI, MEG, and EEG are utilized to illustrate both the signal pathway across multiple brain regions and the underlying brain circuitry24,25. These technologies, however, lack single-unit spatial resolution. Alternatively, optical imaging of genetically encoded calcium and voltage sensors are widely used26-29, which are advantageous for mechanistic study in animals but are difficult to translate to humans in the short term. To bridge this technological gap, two-dimensional microECoG and NeuroGrid devices have been developed to enable high-resolution recording across the entire cortical region18,30,31. Ultraflexible mesh electrodes have been injected into the deep brain to achieve a long-term stable recording with a minor foreign body response32-34, but the recording site is limited to the vicinity of the injection point. Several types of stereo-encephalography electrodes35 and multi-shank probes36-38 have been developed to probe subcortical tissues, however, the tissue damage arising from multiple implantation sites significantly limits their spatial coverage and their neuroscience applications. A 3D multisite deep

brain neural probe with minimal implantation damage would overcome many of these limitations and is described here.

In addition to mapping the electrophysiological signals within the brain, multifunctional neural probes that are capable of modulating the local neural activity provide a powerful technique for studying the brain circuitry39-43. Following the development of optogenetics, optical waveguides and micro-LEDs have been integrated into various electrical recording probes to achieve bidirectional neural interfacing44-52, which has facilitated the study of brain function relative to behavior. Moreover, localized chemical delivery is another useful method not only for interrupting local brain activities3, but also for in vivo cell-type identification53. To that end, multifunctional fiber-based neural probes have recently been developed using a scalable thermal drawing process, which allows for simultaneous optical stimulation, electrical recording, and drug delivery in vivo54,55. However, the interfacing sites in these fiber-based neural probes have been restricted to a single location (at the fiber tip) so far, making the broad application of these probes unfeasible. Integrating the optical, chemical, and electrical functionalities in a minimally invasive and 3D probe within the deep brain would provide a versatile and powerful platform for basic neuroscience and clinical applications.

To achieve this goal, we have developed spatially expandable multifunctional fiber-based probes that can interface with neurons using electrical, optical, and chemical modalities simultaneously, while providing a 3D coverage of the deep brain tissue. To create multisite interfaces in each probe (i.e. depth-dependent probes), we expose electrode recording sites, microfluidic channel openings, and waveguide windows at spaced locations along the fiber length using a femtosecond laser micromachining technique. To realize the probe array expansion after implantation, a scaffold with helix hollow channels was used to direct multifunctional fiber probes

into brain tissue at specified angles. Chronic recordings validate that these fibers can provide long term neuronal readout with a single-unit resolution at multiple locations. Furthermore, we demonstrate that these 3D multifunctional probes can be used to modulate neural activities in transgenic mice and record distinct brain activities from spaced electrodes. Finally, we are able to detect varying electrographic activities among different brain regions during ictal and interictal periods enabling the detection of seizure foci in a mouse model of chronic epilepsy. Our data suggest that this 3D multiplexed brain interface has the potential to allow for multimodal manipulation and analysis of brain circuitry activity between brain regions under the physiological and pathological state.

2.2 Results and discussion

2.2.1 Depth-dependent multifunctional fibers

In this study, a variety of fiber structures were fabricated using a thermal drawing process (TDP) as previously reported[54-56]. A representative "preform" fabrication process to create a multifunctional fiber-based probe (Fiber S1) is shown in **Figure 2.1a**. The waveguide in the center consists of polycarbonate (PC, refractive index $n_{PC} = 1.586$) and polyvinylidene difluoride (PVDF, refractive index $n_{PVDF} = 1.426$) as the core and the shell, respectively. Six grooves were machined next to the waveguide, two of which were inserted with BiSn metal alloy as the electrodes while the other four remained open as fluidic channels. To enable a stable drawing process, a sacrificial layer (PC) was added as the outer layer of this preform, which was etched away after fiber drawing. This macroscopic "preform" was then heated and drawn into a ~ 200-meter-long fiber with preserved cross-sectional structure and a 50-300-fold reduction in diameter (**Figure 2.1b**)**.** The cross-sectional image of the Fiber S1 is shown in **Figure 2.2a**. Similarly, Fiber 1 (F1) with one

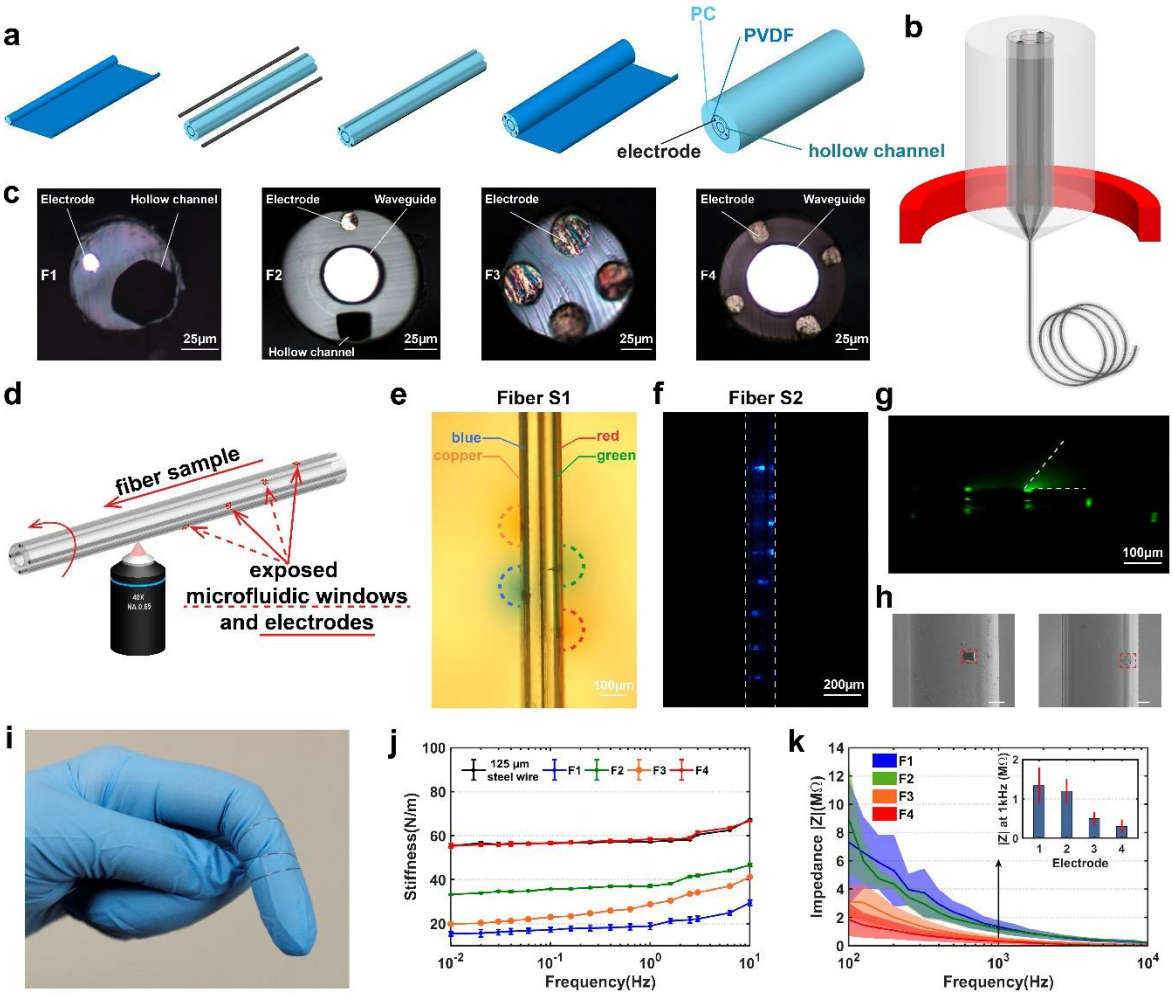

Figure 2.1 Depth-dependent multifunctional fiber probe. (a) A representative multifunctional fiber preform fabrication process (Fiber S1). (b) A schematic of the Fiber S1 thermal drawing process. (c) Cross-sectional images of fibers used in this study, electrode (BiSn). (d) A schematic of femtosecond laser micromachining process on Fiber S1. (e-h) Validation of the exposed microfluidic, optical excitation, and electrical windows: e, four microfluidic windows were created on the four hollow channels of Fiber S1 and four different food colors were injected into the four channels respectively while the fiber was embedded in brain phantom; f, an optical image showing the eight optical excitation sites fabricated on the eight waveguides of Fiber S2; g, optical microscope image of the exposed Fiber S2 immersed in a drop of fluorescein excited by a 473 nm laser; h, SEM images of the exposed microfluidic windows and electrodes (scale bar: 50 μm). (i) A photograph of functional fibers. (j) Bending stiffness measurements of Fiber F1-4. (k) Impedance measurements of the BiSn electrodes in Fiber F1-4. All error bars and shaded areas in the figure represent the standard deviation.

electrode and one microfluidic channel, Fiber 2 (F2) with one electrode, one microfluidic channel, and one waveguide, Fiber 3 (F3) with four electrodes, and Fiber 4 (F4) with four electrodes and one waveguide were fabricated via TDP (**Figure 2.1c**), which were used in the following animal

experiments. Furthermore, we integrated eight waveguides, four electrodes, and one hollow channel within a single fiber (Fiber S2) using a two-step fiber drawing process, and the cross-sectional image of this Fiber S2 is shown in **Figure2.2b**.

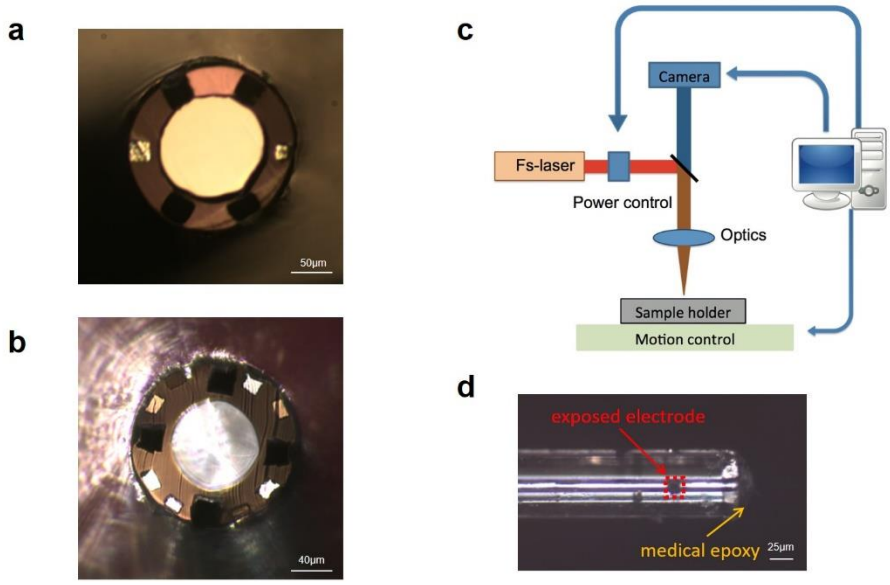

Figure 2.2 Depth-dependent fiber probes (Fiber S1-2). (a) A cross-sectional image of the Fiber S1. (b) A cross-sectional image of the Fiber S2. (c) A detailed illustration of the femtosecond laser micromachining platform. (d) A microscope image of the exposed electrodes. To expose multiple optical, electrical, and microfluidic interfacing sites along the fiber length, we used a femtosecond laser micromachining technique. In this technique, a solid-state ultrafast laser based on titanium doped sapphire (Ti: Sapphire) was utilized, which is capable of generating laser pulses of < 10 fs at a wavelength of 800 nm. Our custom-built platform was also capable of rotating the fiber sample during micromachining, enabling 3D patterning along the fiber length (**Figure 2.1d**, a more detailed illustration is shown in **Figure 2.1c**). To validate the functionality of the exposed microfluidic and electrical interfacing sites, we created four 20 μm x 20 μm windows on the four microfluidic channels of Fiber S1, respectively, with a 250 μm spacing. This fiber, whose tip was sealed using epoxy to prevent fluidic or electrical leakage at the tip end, was then inserted into a

brain phantom (0.6% agarose gel) with four different food colors (1 µl each) injected into these four microfluidic channels, respectively. **Figure 2.1e** shows the successful delivery of food colors to four different depths along the fiber.

Beyond exposing the microfluidic channels of Fiber S1, we also created eight 20 µm x 20 µm optical excitation sites with a spacing of 150 µm on the eight waveguides of Fiber S2. We then coupled this micromachined Fiber S2 to a laser source with a wavelength of 473 nm as shown in **Figure 2.1f**. The light in the optical waveguides is scattered out at the selected locations by ablating partially the cladding and core with the femtosecond micromachining process. Although the light scattering from the eight exposed windows has similar intensity, the directionality in 3D due to their different locations around the fiber circumference causes the windows facing backwards to appear dimmer in the image. In order to have a better understanding of the illumination volumes from these exposed optical excitation sites, we immersed the fiber in a drop of fluorescein solution which emits green light under blue excitation (1% Uranine, Carolina Biological Supply Company). The image shown in **Figure 2.1g** was taken by an optical microscope and the excitation light was filtered out. Furthermore, we also simulated the light scattering using COMSOL Multiphysics© 5.5 equipped with frequency-domain electromagnetic wave solver to validate the fluorescein image (**Figure 2.3**). The dimension and geometry in the simulation were determined by the actual structure of the fabricated fiber which consists of a waveguide with an 11.5 µm-thick PC core and a 5 µm-thick PMMA cladding. The exposed window is 20 µm x 20 µm in widths and 7.5 µm in depth with ~15º tapering. To mimic the actual surface morphology of a femtosecond laser processed surface, the side and bottom of the exposed window are roughened (R_a=0.5 µm and 1µm for the side and bottom, respectively). The waveguide core is illuminated evenly with a 473 nm light and the corresponding refractive index of different layers are 1.6023 (PC),1.4976 (PMMA)

and 1.3361 (water). From both the fluorescein image and the simulation result, we can observe light scattered from the exposed window with an angle of 50°. There is also some light scattering towards the center of the fiber. However, their intensities are reduced by multiple scatterings and reflections by the electrodes and the hollow channel, and therefore the light intensity emitted from the surface of exposed optical windows is dominant near that area.

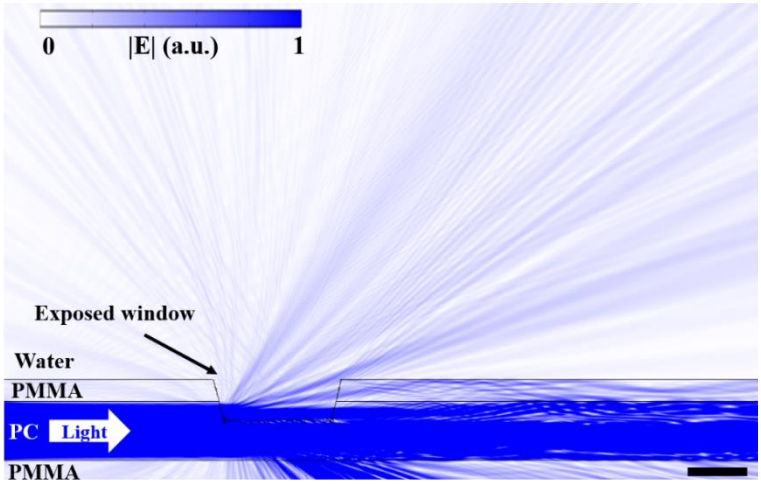

Figure 2.3 2D simulation of the scattered light intensity from a femtosecond-laser exposed waveguide.

Similarly, functional fiber (F3) with four electrodes exposed at a spacing of 50 µm and a size of 20 µm x 20 µm is shown in **Figure 2.2d**. We further verify the exposed microfluidic window and the exposed electrode by Scanning Electron Microscope (SEM) as shown in **Figure 2.1h**, respectively. The electrical performance of the exposed electrodes is validated using impedance measurements as shown in **Figure 2.4**.

We also evaluated the mechanical, electrical, and optical properties of our flexible fiber-based probes. As shown in **Figure 2.1i**, the fibers can be easily wrapped around a finger, exhibiting high flexibility. Indeed, most fiber-based probes (F1, F2, and F3) present significantly reduced bending stiffness compared to conventional stainless steel wires (with a diameter of 125 µm) (**Figure 2.1j**). Even F4 (at a diameter of 250 µm) shares similar bending stiffness with the steel

wire which is much thinner than F4. The impedance of the fiber probes at 1 kHz is found to be 1.3±0.5 MΩ for F1, 1.2±0.3 MΩ for F2, 490±160 KΩ for F3, and 300±170 KΩ for F4, making the fibers good candidates for spike recording (**Figure 2.1k**). The optical transmission spectrum was obtained at a wavelength range of 400 – 700 nm, showing broad transmission across the visible range. The transmission loss measured using cut-back method is 0.99±0.03 dB/cm (F2, R^2=0.99308, n=3) and 1.31±0.03 dB/cm (F4, R^2=0.99274, n=3) at a wavelength of 473 nm (the excitation peak of channelrhodopsin 2 (ChR2)), indicating that the probes allow sufficient light transmission for optogenetic applications. The bending test at 90º angle and radii of curvature of 1.6-7.9 mm shows no significant bending loss under these deformation conditions (**Figure 2.5**).

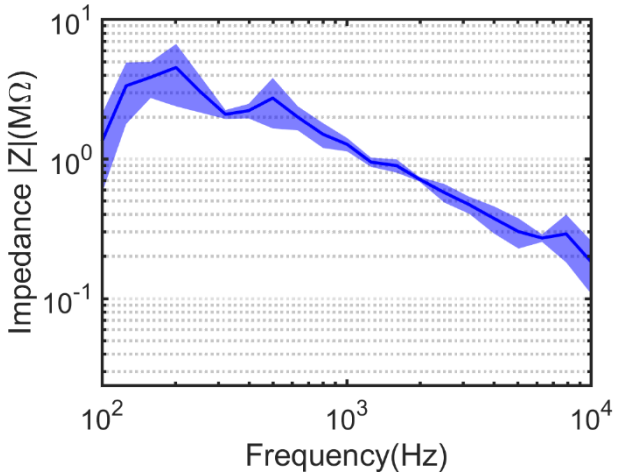

Figure 2.4 EIS measurement of the exposed electrode of Fiber F3. The impedance spectrum of this exposed electrode of Fiber F3 confirmed the successful exposure of the electrode after femtosecond laser micromachining.

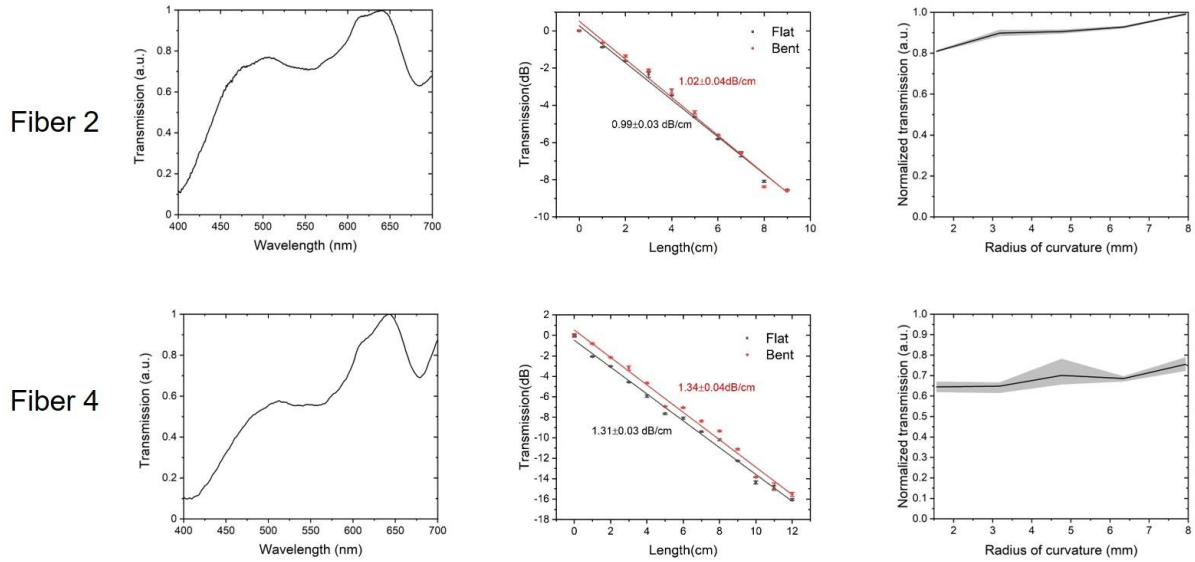

Figure 2.5 Characterization of optical properties of Fiber F2 and Fiber F4. The optical transmission spectrum was obtained at a wavelength range of 400 – 700 nm, showing broad transmission across the visible range (normalized to the maximum value). The transmission loss measured using cut back method is 0.99±0.03 dB/cm (F2, R2=0.99308, n=3) and 1.31±0.03 dB/cm (F4, R2=0.99274, n=3) at a wavelength of 473 nm. And the bending test at 90º angle and radii of curvature of 1.6-7.9 mm shows no significant bending loss under these deformation conditions.

2.2.2 Spatially expandable multifunctional fiber-based probes

Beyond micromachining to create depth-dependent multifunctional interfaces along a single fiber, helical scaffolding fibers were developed for producing spatially expandable fiber probes. To prepare the preform, four PC tubes (with an inner diameter of 9.53 mm and an outer diameter of 12.7 mm) were bundled together and then wrapped with a thin layer of PC (thickness = 300 μm). After consolidation at 200 ºC for ten minutes, four round holes and one square hole were formed in this preform (**Figure 2.6a**). Using a customized preform feeding stage that enables simultaneous translational and rotational motion of the preform, we were able to draw helical scaffolding fibers in a controllable manner (**Figure 2.6b**). Seven different rotational speeds, 60 r/min, 69 r/min, 93 r/min, 108 r/min, 129 r/min, 147 r/min, and 162 r/min, were employed in this study and the optical images of the side views of the scaffolding fibers drawn at these different rotational speeds are shown in **Figure 2.6c**. We can observe that as the rotational speed increases,

the pitch decreases. **Figure 2.6d** demonstrates the relatively linear relationship between the pitch of the scaffolding fiber and the rotational speed, and the average pitch are 23.2 mm, 22.0 mm, 19.3 mm, 15.7 mm, 12.0 mm, 9.0 mm, and 6.7 mm corresponding to each rotational speed, respectively. The cross-sectional geometry of this scaffolding fiber was examined using SEM as shown in **Figure 2.6e**. This unique fabrication method also allows us to scale up the numbers of channels in a single scaffolding fiber, such as seven channel-scaffolding fiber as shown in **Figure 2.6f**.

After the scaffolding fiber is fabricated, an array of multifunctional fibers was inserted into the hollow channels of the scaffold. The scaffolding fiber is used to guide individual functional fibers as well as to alter the direction of the inserted fibers when exiting the scaffold. As illustrated in **Figure 2.6(g-h)**, the employment of the spatially expandable fiber probes involves two steps during the implant surgery. First, we lower the scaffold to a predetermined depth of the brain and apply Metabond® to fix the scaffolding fiber on the skull (**Figure 2.6g**). Second, we further extrude the multifunctional fiber arrays through the scaffold by a calculated length until they reach their targeted locations (**Figure 2.6h**) and fix the whole device onto the skull using a dental cement. The penetration depth of the fiber is controlled by the depth of the scaffolding fiber, the extrusion length of the inserted fiber, as well as the extrusion angle of the scaffold. The location of the inserted fiber can be further confirmed by the equation shown in **Figure 2.6i**. For the fiber inserted into the center hole, it will stay straight when exiting the scaffold. The center point of the helix bottom is set to be the origin of the coordinates. The scaffolding fiber (**Figure 2.6e**) comprises four helixes that intersect with the XY plane at (a, 0, 0), (0, a, 0), (-a, 0, 0), and (0, - a, 0), respectively. For the Helix A ($a\cos\theta$, $a\sin\theta$, $h\theta/2\pi$), a is the radius, θ is the twisting angle of the scaffolding fiber, and h is the pitch of this circular helix. L is the length of the inserted fiber that is in direct contact with brain tissue. The point of the inserted fiber that intersects with the XY plane

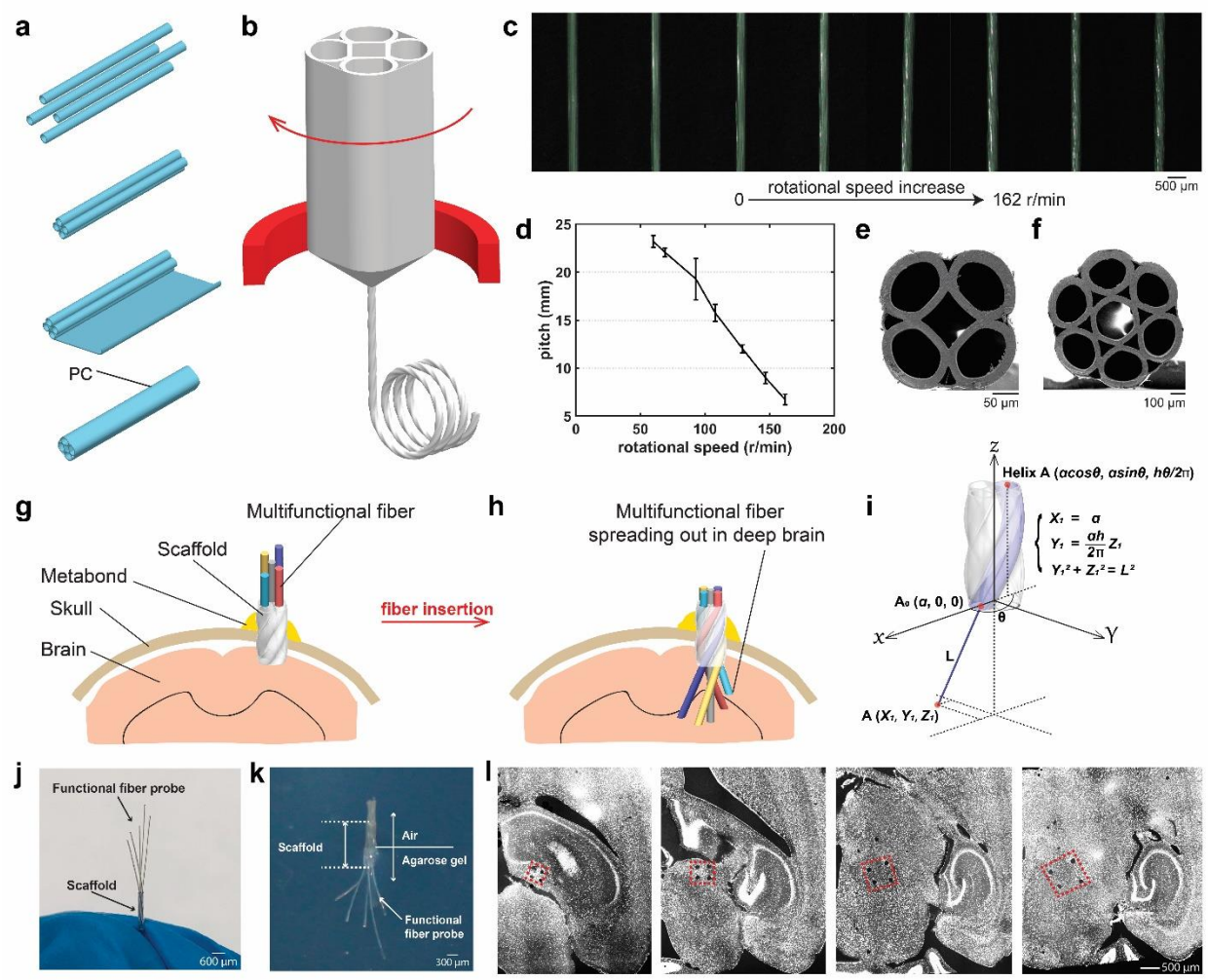

Figure 2.6 Spatially expandable multifunctional fiber-based probes. (a) Scaffolding fiber preform fabrication process. (b) Fiber drawing process with customized rotational feeding stage. (c) Side-view optical images of the scaffolding fibers drawn at different rotational speeds. (d) Plot showing the relatively linear relationship between the pitch and the rotational speed utilized in this study. (e, f) SEM images of the scaffolding fibers with 5 and 7 hollow channels. (g-i) Schematics of the employment of the spatially expandable functional fiber probes: g, scaffolding fiber is inserted into the brain and affixed by Metabond®; h, functional fiber probes are further inserted into the brain tissue through the scaffolding fiber; i, mathematical model of the locations of the inserted fiber probes. (j) Pre-validation of the expansion of the inserted functional fiber probes before implant surgeries. (k) Validation of the expandable fiber probes in the brain phantom. (l), Transverse DAPI-stained brain slices from the mouse with the spatially expandable fiber probes implanted for one week (n=10). Representative images are shown taken from 10 animals. All error bars in the figure represent the standard deviation.

is defined as A_0 (a, 0, 0) and the endpoint of the inserted fiber is defined as A (X_1, Y_1, Z_1). As the inserted functional fiber that exits the scaffold will naturally form a tangent line to the Helix A, X_1 equals a. Based on a given value of a, L, θ, and h, the coordinates of the endpoint of the inserted

fiber A (X_1, Y_1, Z_1) can be calculated by two θ-independent equations: $Y_1 = \frac{ah}{2\pi} Z_1$ and ${Y_1}^2 + {Z_1}^2 = L^2$. Similarly, the locations of the inserted fiber that comes from Helix B (*-asinθ*, *acosθ*, *hθ/2π*), Helix C (*-acosθ*, *-asinθ*, *hθ/2π*), and Helix D (*asinθ*, *-acosθ*, *hθ/2π*) that intersects with XY plane at B (0, *a*, 0), C (*-a*, 0, 0), and D (0, *-a*, 0) are ($-\frac{ah}{2\pi} Z_2$, *a,* Z_2), (*-a*, $-\frac{ah}{2\pi} Z_3$, Z_3), and ($\frac{ah}{2\pi} Z_4$, *-a*, Z_4), respectively. Further calculation is needed for transferring the coordinates to the commonly used ones relative to bregma depending on how the scaffolding fiber is placed. As these coordinates suggest, we can observe a pattern that the diagonal lines of these four points are perpendicular to each other in the XY plane and the intersect point of these two diagonal lines would determine where the scaffolding fiber should be placed in the XY plane.

Before implanting the probes into animals, we will first insert all the functional fiber probes into the channels of the scaffolding fiber individually and move the scaffolding fiber up and down to confirm the expansion of the functional fibers as shown in **Figure 2.6j**. To visualize the spatial expansion of fiber probes through the scaffolding fiber, we inserted the scaffolding fiber to a brain phantom (0.6% agarose gel), followed by the further insertion of the functional fiber probes as shown in **Figure 2.6k**. To further confirm the location of the expanded fiber probes, we implanted the scaffolding fiber and functional fiber probes into the thalamus region of the mouse brain (n = 10) for one week and stained the transverse brain slices (50 μm thickness) for cell nuclei using DAPI. We can clearly observe the damage caused by the scaffolding fiber as well as the functional fiber probes from the implants as shown in **Figure 2.6l**. We can also track the trace of the expanded fiber probes and observe that the distance between the inserted functional fiber probes increases from slice to slice. The square shape formed by the four damage points rotated evenly from brain slice to slice which fits the expectation of linear insertion of the functional fiber probes when exiting the scaffolding fiber. Based on the damage points from the stained brain slices, we found

that the expanded fiber probes can reach the targeted region with an average success rate of 81.3% per site (number of successful sites/number of total sites) and 60% per animal (number of successfully targeted animals/number of animals).

As the previous results showed, the angle of the inserted functional fiber can be further tuned by adjusting the rotational speed during the thermal drawing of the scaffolding fiber, which indicates that the scaffolding fiber can guide the functional fiber into arbitrary locations in the deep brain. Furthermore, utilizing scaffolding fiber with more hollow channels and combining it with depth-dependent probes would allow us to sample dense brain regions in three dimensions.

2.2.3 Spike recording and burst-suppression recording using spatially expandable fiber probes

To evaluate the functionality of the spatially expandable fiber probes in recording localized brain activities with certain distances, we implanted fiber probes with 5 individual branches (Fiber F1) into the different parts of the hippocampus of wild type mice (n=5) as schematized in **Figure 2.7a**. **Figure 2.7b** shows a mouse with these fiber probes implanted for 5 weeks. The recording was conducted in these mice under continuous anesthesia induced and maintained by isoflurane. Two out of the five implanted fiber probes detected spike activities 5 weeks post-implantation (**Figure 2.7c-h**). The electrophysiological signals recorded 5 weeks after implantation were

bandpass-filtered to examine the local field potential (LFP, 0.3-300 Hz) and spiking activity (0.3-5 kHz). On one electrode, we found one distinct cluster of spikes *via* principal component analysis (PCA). This spike activity is most likely axonal, as indicated by the sharp voltage drop and short duration waveforms (**Figure 2.7c**)[57] and its peak and repolarization voltages are shown in **Figure 2.7d**. The other electrodes captured spiking activity from multiple neurons, from which two spike

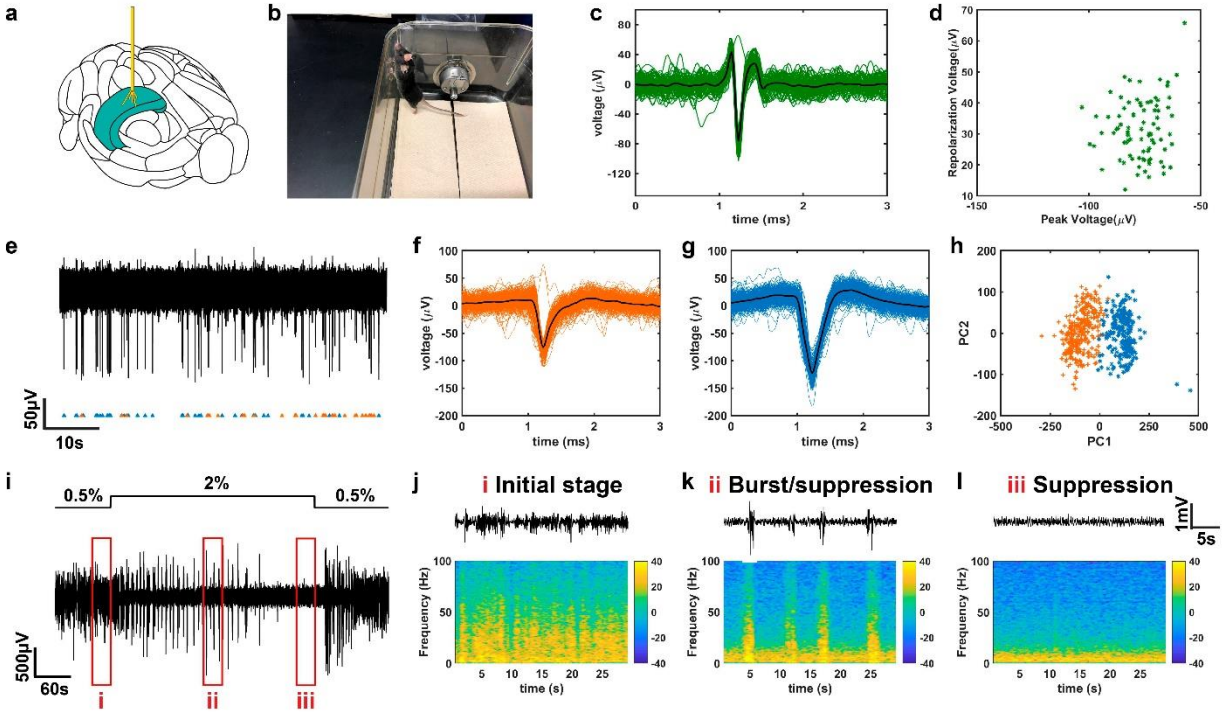

Figure 2.7 Spontaneous activity investigation by spatially-expanded functional fiber probes (F1, n=5). (a) An illustration of the spatially-expanded fiber probe targeting the hippocampus region in a mouse brain. (b) A photograph of a wild type mouse with small electrodes implanted for 5 weeks. (c) A single cluster segregated 5 weeks after implantation from electrode one and (d) it's peak voltage and repolarization voltage. (e-h) Filtered endogenous activity 5 weeks after implantation from electrode two containing two separable units. (f-g) Action-potential shapes of the two units. (h) Principal-component analysis (PCA) of the two units. (i) Local filed potentials recordings 8 weeks after implantation from electrode one with the alternating anesthesia level (0.5-2% v/v isoflurane). (j-l) Different levels of LFP activity recorded under the varying concentration of isoflurane, where (j) shows the initial stage (before the increase of isoflurane level), (k) shows burst/suppression stage (transition period) and (l) shows suppression stage (deep anesthesia period). Representative images are shown taken from 5 animals.

clusters can be well isolated *via* PCA (**Figure 2.7e-h**), where the quality of the isolation was

assessed by L-ratios and isolation distance (0.0084 and 147.5, respectively). Thus, based on the recording obtained from these two spaced electrodes, we could detect very different activity patterns with our spatially expandable fiber probes providing useful insights for future investigation of brain functions.

We also altered the isoflurane levels during recording (0.5-2% v/v) and observed characteristic time and dosage-dependent changes in the LFP (**Figure 2.7i-l**) 8 weeks post-implantation. Fig. 3j depicts the power spectrum of LFP obtained under a lower level of anesthesia (0.5% v/v isoflurane). After the concentration of isoflurane was adjusted to 2% v/v, we observed burst suppression (**Figure 2.7k**), a hyperexcitable brain state induced by gas anesthetics where alternating high voltage activities (burst) and flatline (suppression) periods appear quasiperiodically[58,59] (**Figure 2.7j**). When the animal was in deep anesthesia, a general suppression of the LFP occurred (**Fig. 3l**). Both respiration rate and responsiveness to toe pinch decreased as the anesthetic level was increased. During deep anesthesia (i.e., suppression), there was a loss of toe pinch withdrawal. The LFP activity returned to the level as measured during the initial stage of recording once the concentration of isoflurane was decreased to 0.5% v/v. Four electrodes out of the five implanted fiber probes presented similar results during the administration of isoflurane (**Figure 2.8**).

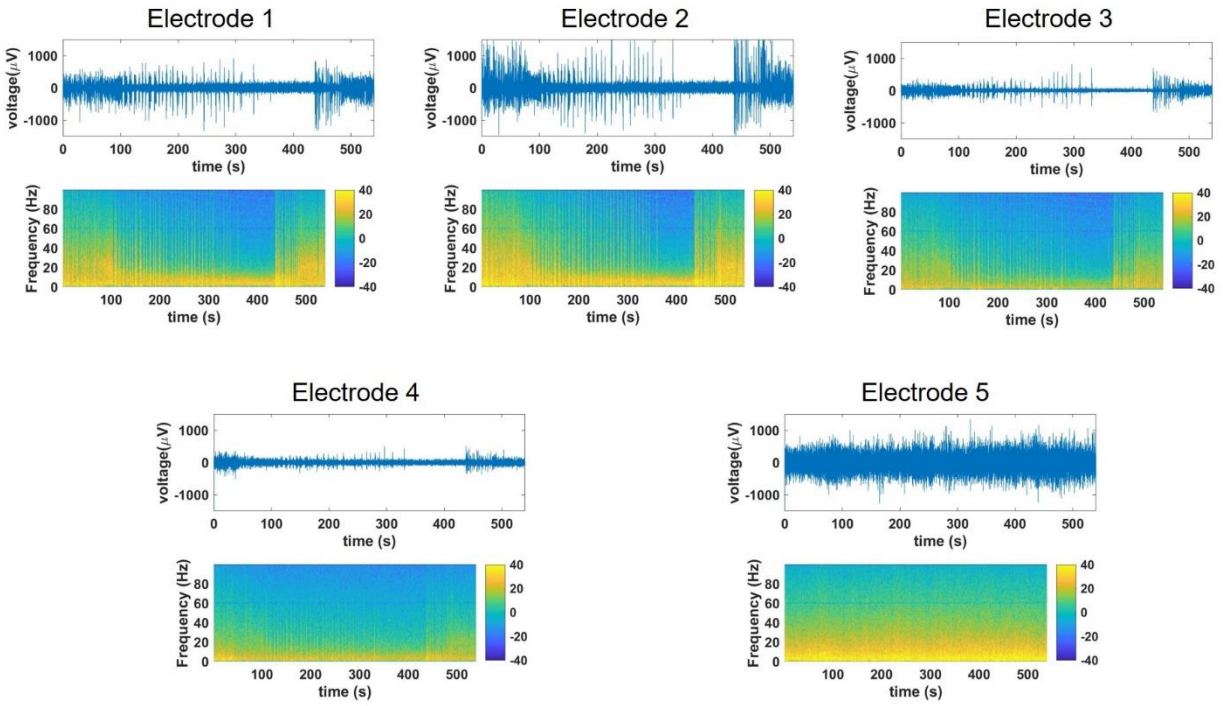

Figure 2.8 LFP recordings from spatially expandable fiber probes. The fibers were implanted in the hippocampus region of the wild type mouse brain with altered isoflurane levels during recording (0.5-2% v/v). Electrodes 1-4 showed similar results.

2.2.4 Optogenetic control and electrophysiological readout with implanted fibers

In this study, we first exposed Fiber F4's four electrodes via femtosecond micromachining with a spacing (distance between neighboring electrodes) of 0.5 mm, 1.1 mm, and 0.9 mm from top to bottom. The waveguide in the fiber probe was coupled to a silica optical fiber using a direct ferrule-to-ferrule coupling, which was connected to a laser source with a wavelength of 473 nm. The electrodes were connected to the headstage of the recording system via pin-connectors for electrical readout. These depth-dependent fiber probes were implanted into *Thy1-ChR2-YFP* mice, with four electrodes designed to target the cortex, the hippocampus, and two places in the thalamus, and the optical stimulation was delivered at the bottom of this fiber probe (n=5, **Figure 2.9a**). Laser pulses at frequencies of 10 Hz, 20 Hz, and 100 Hz with a pulse width of 5 ms and a power density of 7.3 mW/mm^2 were applied and all the four electrodes detected optically evoked neural activities corresponding to 10 Hz laser pulses 5 months after implantation (**Figure 2.9b**). After

normalization of the peak-to-peak value of the optically excited signals, we observed that electrode four which was the closest to the stimulation site detected optically excited signals with the highest amplitude systematically (**Figure 2.10a**). We also conducted the same stimulation and recording experiments in a perfused brain (**Figure 2.11**) confirming the signals we detected were not artifacts.

We also performed optical stimulation at different brain regions along the depth- dependent fibers and recorded distinct brain activities from spaced electrodes. To our knowledge, both the size of the optical window and the light intensity will have effects on the optically evoked signal. Thus, we have exposed the optical windows with the same sizes on the side of the fiber probes at different depth to ensure the same excitation area and similar light intensity. In this specific experiment, we exposed the four electrodes of the Fiber F4 with a spacing of 0.5 mm, 0.8 mm, 1.2 mm from top to bottom to target the brain regions of cortex, CA1, CA3, and thalamus. In the meantime, the optical window is exposed on the side of the fiber right next to the top (cortex, n=6), middle (CA1, n=5) or bottom (thalamus, n=6) electrode to elucidate the neural activity from the same brain region with different optical excitation sites. The measured light efficiency from the laser source to the exposed window is 0.67% (**Figure 2.12**), and the power density in our experiments is 9.1 mW/mm^2. To block the light leakage from the bottom tip of the fiber, we applied sufficient black epoxy to cover the tip of the fiber probes. We found that the electrode closest to the optical excitation site detected the optically evoked signal with the highest amplitude (**Figure 2.13**), consistent with our other optical stimulation and recording results (**Figure 2.9b**). Furthermore, we employed spatially expandable fiber probes (five F2 probes with a scaffolding fiber) to the brain region of the thalamus and only fiber one was connected to the laser source while the others were simply connected for electrical readout (n=5, **Figure 2.9c**). Similarly, laser

pulses with a pulse width of 5 ms, a power density of 7.3 mW/mm^2, and frequencies of 10 Hz, 20 Hz, and 100 Hz were delivered to the thalamus region right next to electrode one. All five fiber probes detected optically excited neural activities with 10 Hz laser pulses 3 months post implantation (**Figure 2.9d**) and electrode one observed the highest peak-to-peak amplitude with normalization (**Figure 2.10b**).

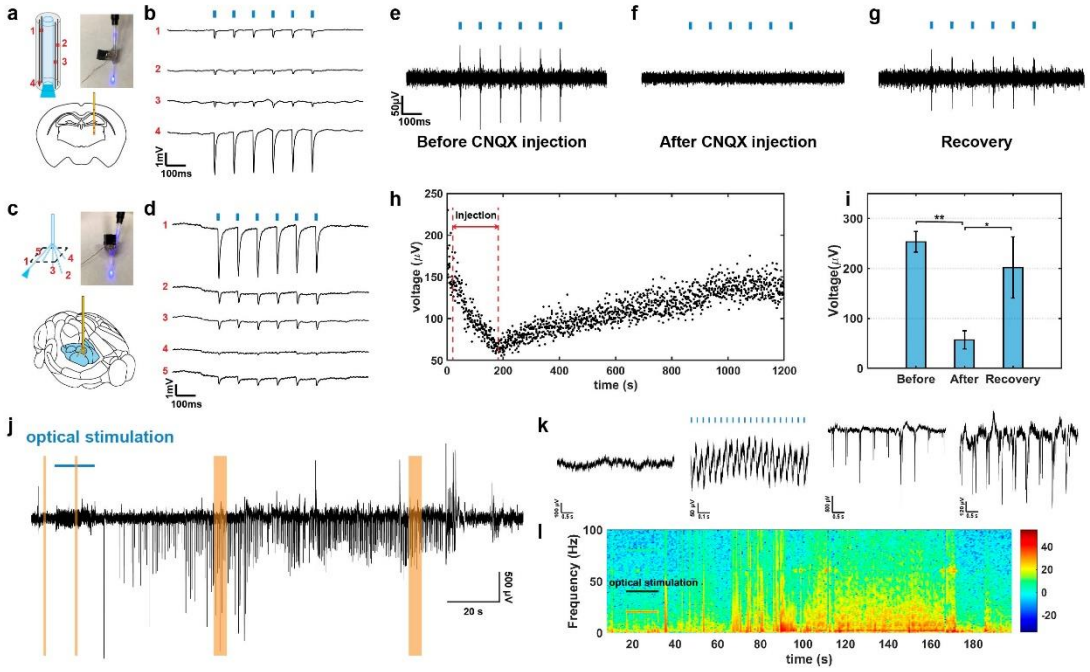

Figure 2.9 Simultaneous multisite optogenetic stimulation, electrical recording, and drug delivery. (a) An illustration of the depth-dependent multimodal fiber probe targeting cortex, hippocampus and thalamus regions in a transgenic Thy1-ChR2-YFP mouse brain and a photograph of the assembled device coupled to the 473 nm laser. (b) Unfiltered electrophysiological recording from depth-electrodes 1-4 during optogenetic stimulation (10 Hz, 5ms pulse width, 7.3 mW/mm2) 5 months after implantation (n=5). (c) An illustration of the spatially-expanded multimodal fiber probe targeting the thalamus region in a transgenic Thy1-ChR2-YFP mouse brain and a photograph of the assembled device coupled to the 473 nm laser. (d) Unfiltered electrophysiological recording from electrodes 1-5 during optogenetic stimulation (10 Hz, 5ms pulse width, 7.3 mW/mm2) 3 months after implantation (n=5). (e-g) Filtered (0.3 - 5 kHz) electrophysiological recording from a F2 multifunctional probe (e) before, (f) 30 s after and (g) 1180 s after CNQX administration through the multifunctional fiber during optogenetic stimulation (10 Hz, 5ms pulse width, 7.3 mW/mm2). (h) Peak-to-peak amplitude values of each detected optically evoked spiking activity show a decrease in amplitude induced by CNQX administration and a gradual recovery phase after the termination of CNQX delivery. (i) Comparison of the mean peak-to-peak amplitude values measured before, during and, after CNQX injection (Repeated measure one-way ANOVA Tukey's multiple comparisons test, **p<0.01

(Before vs. After, p=0.0044), *p<0.05 (After vs. Recovery, p=0.0134), n=3). (j) Seizure-like afterdischarges were induced by repetitive optical stimulation (20 Hz, 5ms pulse width, 7.3 mW/mm2) using spatially expandable fiber probes (n=10). (k) Zoomed in details of the recording results highlighted in Figure 2.9j. (l) Power spectrum density plot of the representative trace shown in Figure 2.9j. Representative images are shown taken from ⩾ 3 animals analyzed per each experimental group. All error bars in the figure represent the standard deviation.

To assess the chemical delivery function in conjunction with the electrical recording and optical stimulation capabilities, the F2 probe's hollow channel was connected to a miniaturized tubing and implanted to the thalamus region of *Thy1-ChR2-YFP* mice. 2.5 µl of the synaptic blocker 6-cyano-7-nitroquinoxaline-2,3-dione (CNQX, 0.1 mM, 80nl/s) was injected intracranially to the thalamus region through a microfluidic channel of the F2 probe (n=3). We bandpass-filtered the signals from 300 to 5000 Hz to study the activities of optically stimulated neurons. Before CNQX injection, optically evoked neural activities (10 Hz, 5-ms pulse width, 7.3 mW/mm^2) were observed consistently (**Figure 2.9e**). After CNQX injection, we observed no responsive neural activities corresponding to laser pulses (**Figure 2.9f**) and neurons started to respond to laser pulses after several minutes of recovery (**Figure 2.9g**). We calculated the peak-to-peak amplitude of each optically evoked neural activity during the entire experiment and we can observe the gradual decrease and increase of the amplitude which represents the drug intervention and recovery processes, respectively (**Figure 2.9h**). We also observed a reduced peak-to-peak amplitude of the recovered signals compared to those before drug injection (**Figure 2.9i**: repeated measure one-way ANOVA Tukey's multiple comparisons test, **p<0.01 (Before vs. After, p=0.0044), *p<0.05 (After vs. Recovery, p=0.0134, n=3). The data shown in **Figure 2.9e-i** were bandpass-filtered in the frequency range of 0.3-5 kHz while the unfiltered raw data still presents optically stimulated signal before and after CNQX injection (**Figure 2.14**), which indicates that CNQX only affected neurons close to the microfluidic channel while the neighboring neurons that were not in contact with CNQX still responded to laser pulses.

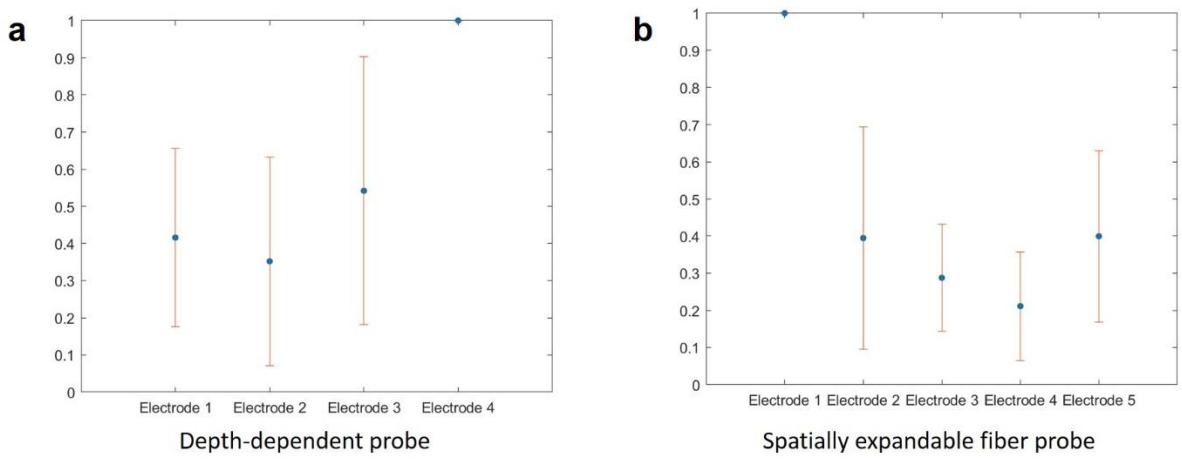

Figure 2.10 Normalization of the recording results from depth-dependent probes and spatially expandable fiber probes. (a) Normalized optically stimulated results from depth-dependent probes indicate that the electrode four which was the closet to the optical stimulation site detected the highest signal in average. (b) Normalized optically stimulated results from spatially expandable fiber probes indicate that the electrode one which was the closet to the optical stimulation site detected the highest signal in average. All error bars in the figure represent the standard deviation.

To further demonstrate the multifunctional capability of the fiber probes, we have also employed the spatially expandable fiber probes (fiber F2) for seizure induction via repetitive optical stimulation and simultaneous electrical recording. It has been previously reported that repetitive optical stimulation can perturb the normal hippocampal activity to induce seizure-like afterdischarges[60]. Here, we implanted the spatially expandable fiber probes (Fiber F2) to target the brain regions of cortex and hippocampus (rostral CA1, caudal CA1, and CA3) and performed repetitive optical stimulation to one location (rostral CA1) to induce seizure-like afterdischarges (n=10). During the stimulation, both 10 Hz and 20 Hz light pulses were delivered for 10-30 seconds at a pulse width of 5-15 ms and multiple optical stimulation trials were performed. We can observe that large spikes appeared following optical stimulation and gradually became synchronous in all these four areas (**Figure 2.9j-l** and **Figure 2.15**). These seizure-like afterdischarges continued for a duration of 7.5-131.5 s without any optical stimulation. These results show that our

multifunctional spatially expandable fiber probes allow for the manipulation and recording of neural activities across multiple brain regions, which can be useful for both basic neuroscience and disease applications.

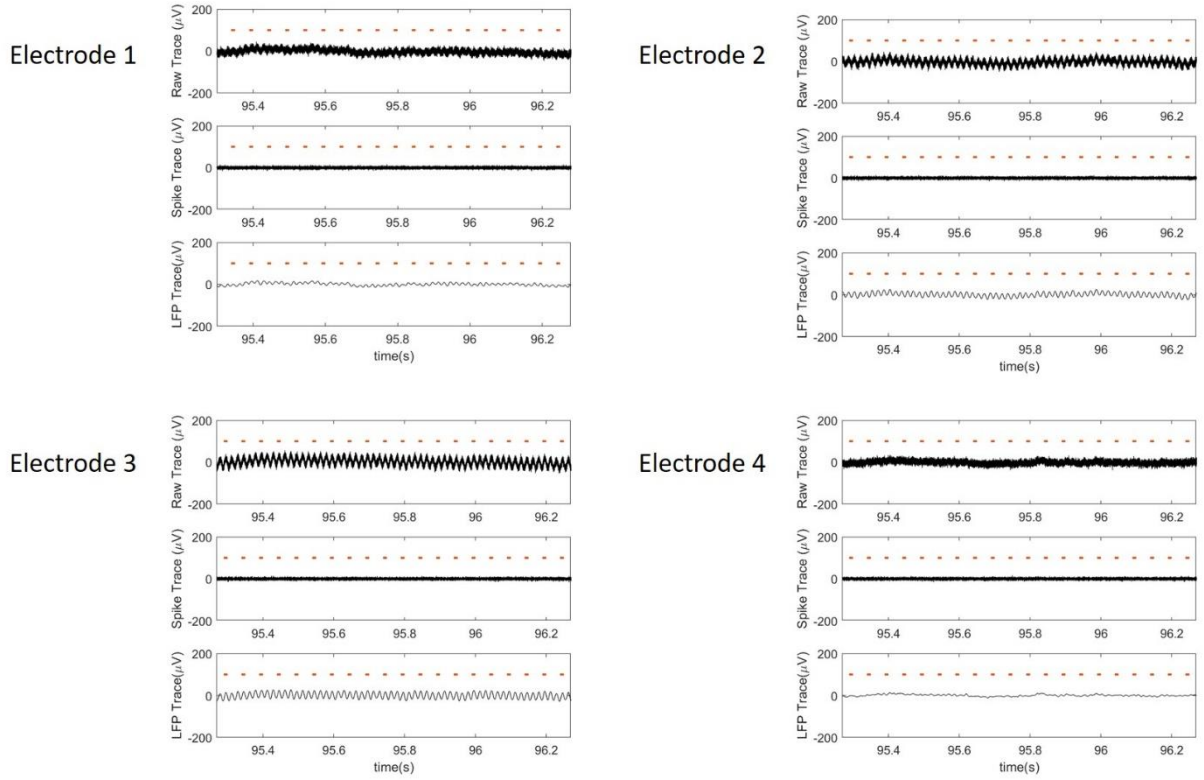

Figure 2.11 Recordings from a perfused brain with optical stimulation of 10 Hz by the depth-dependent fiber probes. No optically evoked signals recorded from these four electrodes confirmed the fact that the recording results we collected in live animals were not artifacts.

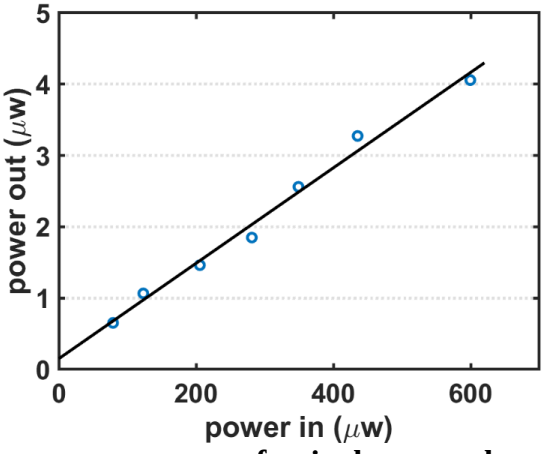

Figure 2.12 Light efficiency measurement of a single exposed optical window.

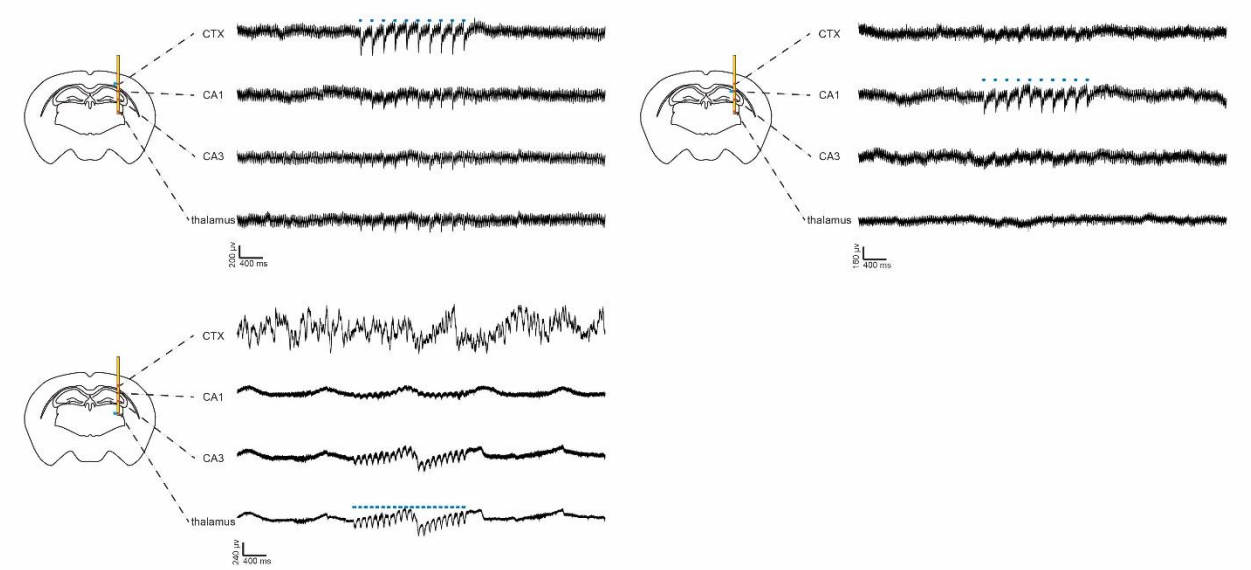

Figure 2.13 Simultaneous optical stimulation and electrical recording in Thy1 mouse using the depth-dependent fiber probes. The four electrodes are located at the cortex, CA1, CA3, and thalamus regions, and light is delivered at the side of the fiber adjacent to the electrodes targeting cortex, CA1, and thalamus regions, respectively. The blue dashed lines indicate the laser pulses.

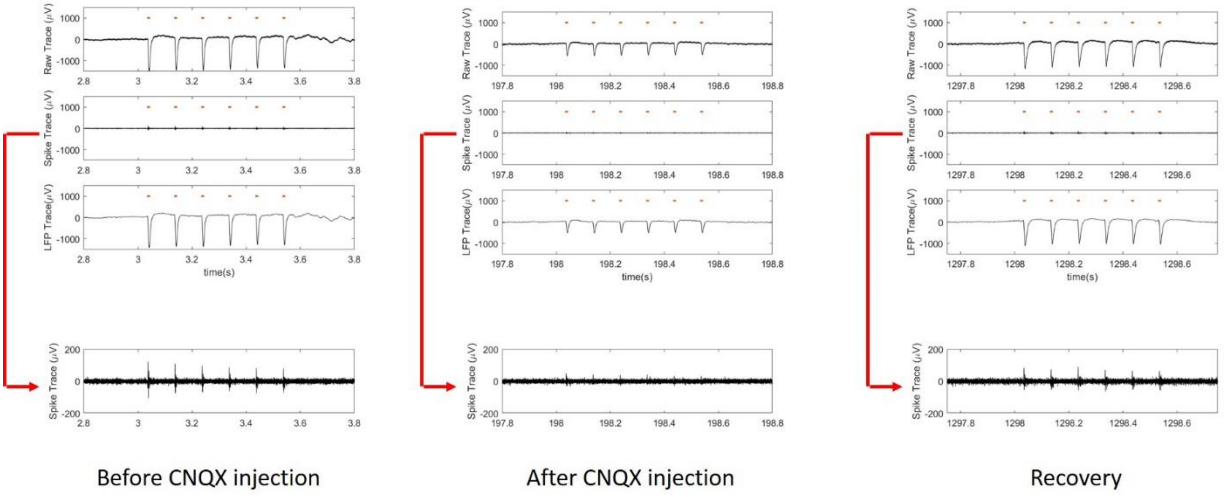

Figure 2.14 Unfiltered, Spike-filtered, and LFP filtered recording results before, during and after CNQX administration in a transgenic Thy1-ChR2-YFP mouse brain. We can observe that the spike-filtered recording had no optically evoked signal immediately after CNQX injection while the raw data still presented the optically evoked signal in the whole time, which indicates that CNQX only affected neurons close to the microfluidic channel while the neighboring neurons that were not in contact with CNQX still responded to laser pulses.

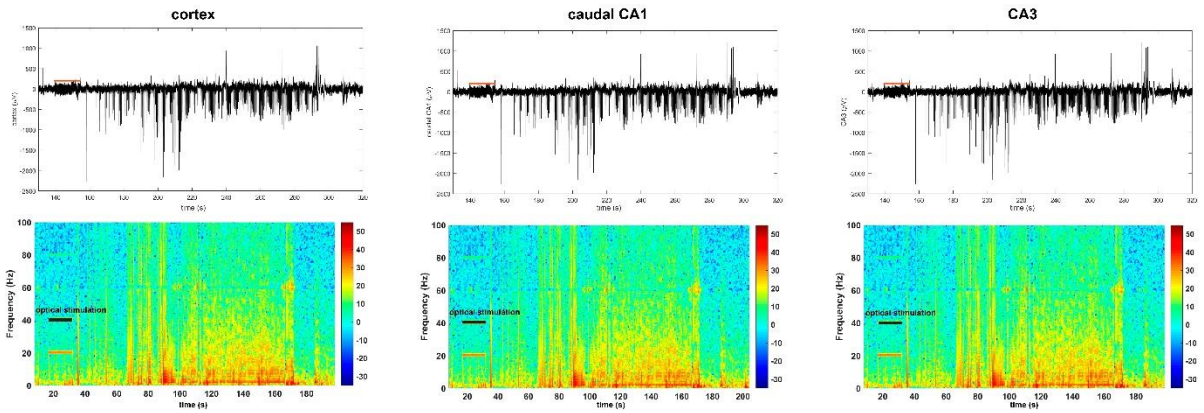

Figure 2.15 Similar brain activity of the seizure-like afterdischarges detected by other three brain regions.

2.2.5 Multisite in vivo recordings by fiber probes in a mouse model of infection-induced epilepsy

We also investigated the utility of depth-dependent fiber probes and spatially expandable fiber probes for studying dynamic spatiotemporal structure of seizure using a mouse model of viral infection-induced temporal lobe epilepsy. In this model, wild type mice infected intracortically with Theiler's murine encephalomyelitis virus (TMEV) show acute behavioral seizures during the first week of infection, exhibit clinically relevant pathological and physiological changes in the hippocampus, survived the infection and later develop chronic epilepsy after approximately two months of infection[61,62]. Detection of seizures in this model has been reported previously by video encephalography (vEEG) studies that used traditional stainless steel electrodes implanted either epidurally[63] or in the dentate gyrus[61]. These studies were limited by their use of single-channel recording, and thus, could not provide information on the brain regions implicated in seizure generation and propagation. Our multisite fiber-based probes could be very useful to detect network activity from various regions while minimizing damage to the brain.

We implanted depth-dependent fiber probes in mice either vertically (F3) to the skull (straight implant) for targeting cortex (CTX), CA1 and CA3 areas of hippocampus, and

hypothalamus (HY) (straight implant, n=3), or at an angle (F3) to the skull (angular implant, n=4) for targeting CTX, CA1, CA3, and amygdala (AMG) (**Figure 2.16b and Figure 2.16f**). The spatially expandable fiber probes were implanted to target CA1, CA3, and thalamus **(Figure 2.16j)**. The CA1 region of the hippocampus is highly susceptible to TMEV-induced cell death with a partial or complete loss of pyramidal cell layer, whereas the pyramidal neurons in the area CA3 remain largely intact during acute seizures[64]. The neuronal circuitry in the CA3 region becomes hyperexcitable during epileptogenesis following TMEV infection[65]. Therefore, two electrodes of the fiber probe were inserted into the CA1 and CA3 regions to detect any difference in the field potential in these two regions. The remaining electrodes were targeted to cortex, amygdala, and hypothalamus to detect generalized electrographic activity during the propagation of seizures. **Figure 2.16a** shows an example of EEG recording obtained by a depth-dependent fiber probe implanted in the amygdala of TMEV-infected mouse. Various electrographic features associated with seizures such as preictal spiking, the gradual evolution of amplitude and frequency of spikes during the ictal phase, post-ictal spiking and post-ictal suppression were detected by the fiber probe. Representative EEG traces from each brain region during a convulsive seizure and their corresponding frequency distributions are shown in **Figure 2.17** (**straight implant**) and in **Figure 2.16 (g-h)** (**angled implant**). Similarly, **Figure 2.16 (c-d)** shows EEG traces and their corresponding frequency distributions for a nonconvulsive seizure (**straight implant**). The power spectrum of electrographic discharges during the ictal period was computed to compare seizure severity between the brain regions tested (**Figure 2.16e and 2.16i, Figure 2.17)**. For a straight implant, mean powers of signals recorded from CTX, CA3, and HY were almost identical for convulsive seizures, whereas cortex showed significantly higher activity during nonconvulsive seizures compared to other brain regions (**Figure 2.16e**: CTX vs. CA1 – $^{*}p<0.05$, $^{**}p<0.01$,

$^{***}p<0.001$, $^{****}p<0.0001$; CTX vs. CA3 – $^{‡}p<0.05$, $^{‡‡}p<0.01$; CTX vs. HY – $^{\#}p<0.05$, $^{\#\#}p<0.01$; n=14 seizures). For angular implant, mean powers of signals detected by electrodes implanted in CA3 and amygdala were significantly higher than signal intensity in cortex and CA1 (**Figure 2.16i**: CA1 vs. CA3 and CA1 vs. AMG – $^{††††}p<0.0001$; CTX vs. AMG – $^{\#}p<0.05$, $^{\#\#}p<0.01$; n=20 seizures). The mean power of signal recorded from CA1 was significantly lower than that from other brain regions for convulsive seizures detected by both straight and angled implants, which reflects TMEV-induced neuronal damage predominantly in the CA1 region (**Figure 2.16l and Figure 2.16m**). Similarly, the spatially expandable fiber probes also detected robust electrographic activity in CA3 compared to CA1 (**Figure 2.16k**, n=12 seizures, n=3 animals).

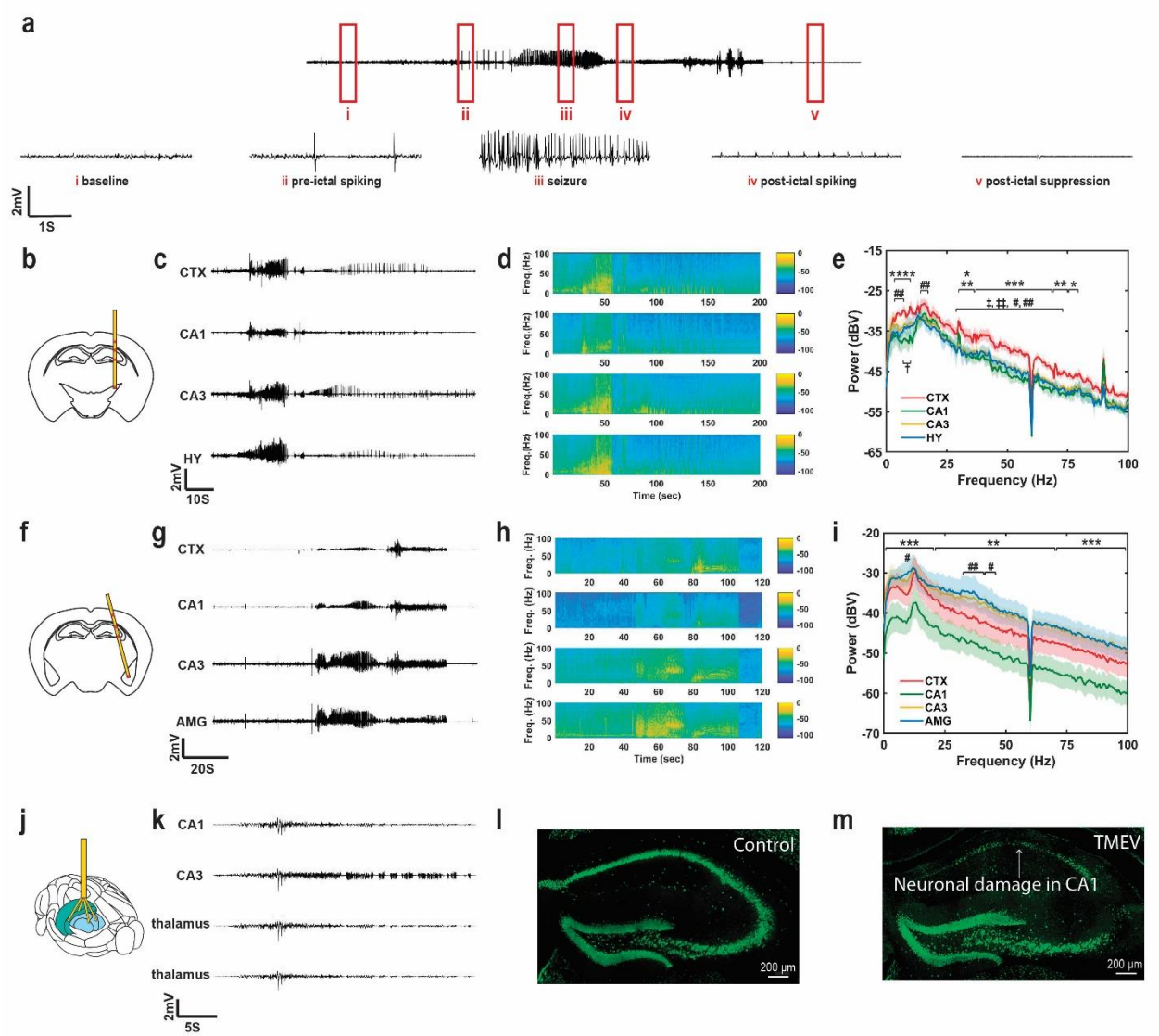

Figure 2.16 Multisite recording of seizure activity in various brain regions in a mouse model of infection-induced epilepsy. (a) An example of electrographic recording by a fiber probe implanted in the amygdala of a TMEV-infected mouse is shown. Various stages of mouse behavior before, during and after convulsive seizure are identified in red rectangles and the corresponding magnified traces are depicted below: baseline (non-ambulatory physiological stage), pre-ictal spiking (periodic electrographic discharges before or during seizure initiation), seizure (high frequency spikings during fully generalized tonic-clonic seizure), post-ictal spiking (periodic electrographic discharges immediately after seizure), and post-ictal suppression (behavioral arrest following convulsive seizure). (b) Diagram of coronal section of a mouse brain shows the location of depth-dependent fiber probes in cortex (CTX), CA1 and CA3 regions of the hippocampus, and hypothalamus (HY) as indicated by red marks along with the probe assembly (straight implant, n=3). (c-d) Representative traces of electrographic recordings from CTX, CA1, CA3, and HY during a non-convulsive seizure and their corresponding frequency distribution (straight implant). (e) Power spectrum density plot for non-convulsive seizures show that mean power of signal recorded from CTX was significantly higher compared to mean power from other brain regions

for various frequency bands between 1-100 Hz (Two-way ANOVA, Tukey's multiple comparisons test; CTX vs. CA1 – *p<0.05, **p<0.01, ***p<0.001, ****p<0.0001; CTX vs. CA3 – ‡p<0.05, ‡‡p<0.01; CTX vs. HY – #p<0.05, ##p<0.01; n=14 seizures). (f) Diagram of the coronal section of a mouse brain shows the location of depth-dependent fiber probes in the cortex (CTX), CA1, CA3, and amygdala (AMG) as indicated by red marks along with the probe assembly (angular implant, n=4). (g-h) Representative traces of electrographic recordings from CTX, CA1, CA3, and AMG during a convulsive seizure and their corresponding frequency distribution (angular implant). (i) Power spectrum density plot for convulsive seizures show significantly higher mean power of signal recorded from CA3, AMG and CTX compared to that in CA1 between 1-100 Hz (Two-way ANOVA, Tukey's multiple comparisons test; CA1 vs. CA3 and CA1 vs. AMG – ††††p<0.0001; CA1 vs. CTX – **p<0.01, ***p<0.001; n=20 seizures). (J) Diagram of a mouse brain showing the location of two spatially expandable fiber probes implanted in CA1 and CA3 regions of the hippocampus and the other two in the thalamus (n=3). (K) Similar to depth-dependent fiber probes, representative traces of electrographic recordings from the hippocampus and thalamus obtained by spatially expandable fiber probes indicate higher network activity in the CA3 region. (l-m) Immunohistochemical staining of nuclear neuronal protein (NeuN, in green) in brain slices shows the neuronal loss in the CA1 region of the TMEV-infected mouse with seizures (m) compared to the sham-injected control mice (l). The loss of neurons in the CA1 region may explain the lower power of electrographic activity detected by fiber probes in CA1. Representative images are shown taken from $\geqslant$ 3 animals analyzed for each experimental group and were chosen to reflect the mean value of quantitative data. All shaded areas in the figure represent the standard deviation.

Both clinical and animal studies have identified a crucial role of the amygdala, a part of the temporal lobe, in epileptogenesis[66]. A large number of patients with temporal lobe epilepsy (TLE) shows extensive neuropathology in the amygdala, in addition to hippocampal damage. Animal studies suggest that the amygdala is even more susceptible to the generation of seizures than the hippocampus, which may explain faster development of electrical kindling-induced seizures in the amygdala than in the hippocampus. In addition, anxiety and depression are common comorbidities associated with TLE, and the neuronal circuitry in the amygdala and hippocampus is strongly associated with the pathophysiology of anxiety and depression[67]. Indeed, TMEV-infected epileptic mice also show anxiety behavior. Therefore, severe electrographic activity detected in the amygdala and the CA3 region of the hippocampus during TMEV-induced convulsive seizures provides a basis for further investigation of changes in network connectivity between the amygdala and hippocampus in this model.

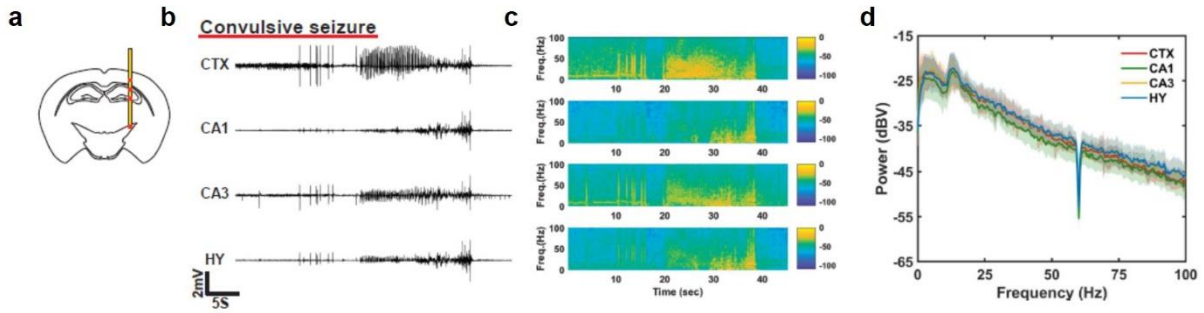

Figure 2.17 Convulsive seizure detected by depth-dependent fiber probe (straight implant). (a). Diagram of coronal section of a mouse brain shows the location of depth-dependent fiber probes in cortex (CTX), CA1 and CA3 regions of hippocampus, and hypothalamus (HY) as indicated by red marks along with the probe assembly (straight implant). (b-c). Representative traces of electrographic recordings from CTX, CA1, CA3, and HY during a non-convulsive seizure and their corresponding frequency distribution. (d). Power spectrum density plot for convulsive seizures shows no difference in mean power of signal recorded from different regions.

2.2.6 Evaluation of fiber probe and stainless steel microwire biocompatibility using immunohistochemistry

Reactive tissue response to our multifunctional fiber-based probe was assessed using immunohistochemical analysis of surrounding brain tissue from mice implanted for four-weeks with either a multifunctional probe Fiber F1 or a conventional stainless steel probe (n=3). The presence of glial fibrillary acidic protein (GFAP) was used to assess astrocyte reactivity to the probe, ionized calcium-binding adaptor molecule 1 (Iba1) was used as a marker of microglial response, and lastly, the neuron-specific protein NeuN was used to analyze neuronal density. Representative images from the multifunctional probe and stainless steel probe are presented in **Figure 2.18**. Neuronal density, microglia density, and astrocyte reactivity were compared between all groups, and no significant difference was observed, as shown in **Figure 2.18e-g**. We also validated the biocompatibility of the Fiber F2 by implanting the Fiber F2 probe or stainless steel wire into the hippocampus region of wild type mice for four weeks (n=3) as shown in **Figure 2.19**.

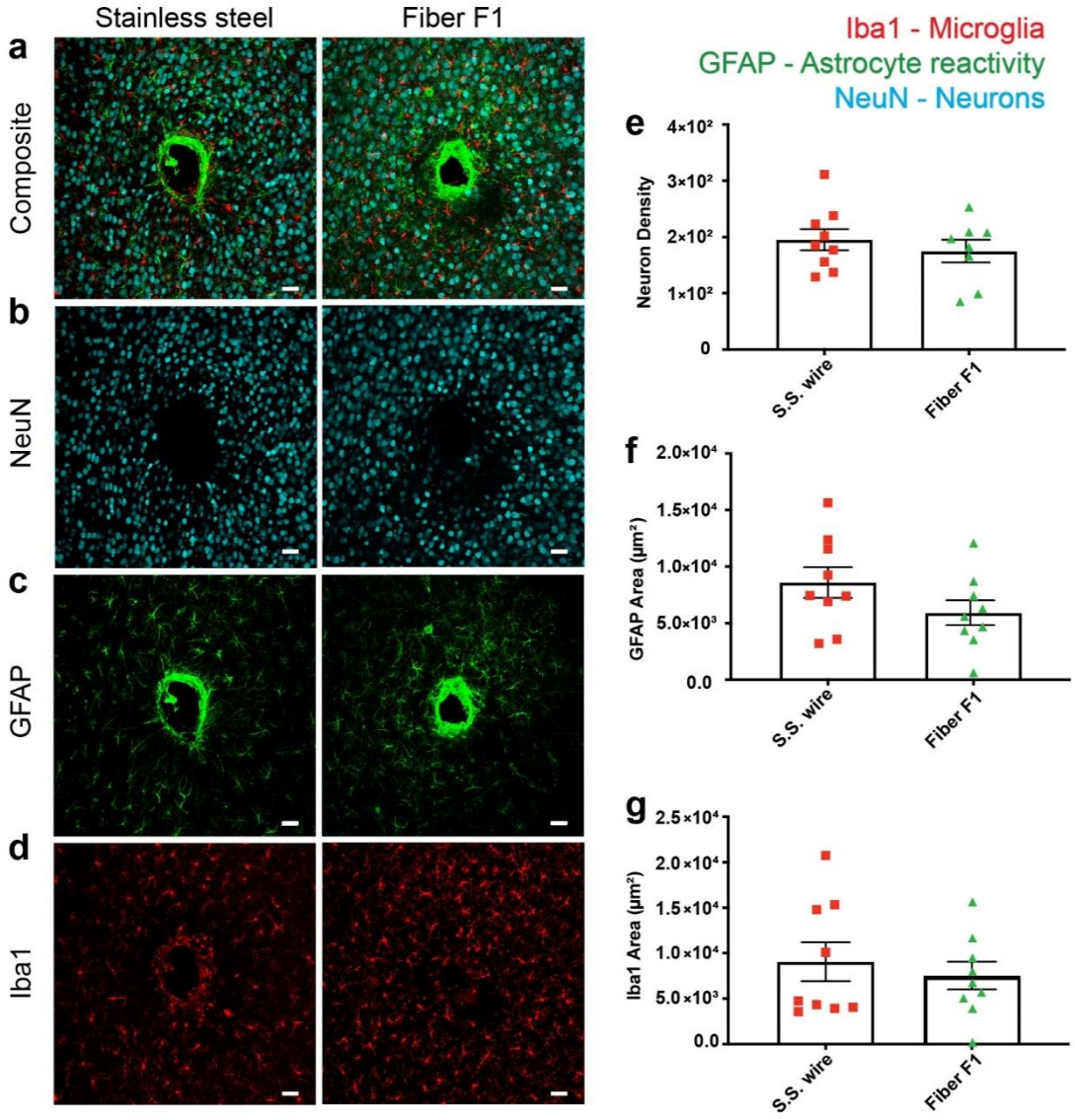

Figure 2.18 Biocompatibility study of the functional fiber probes (Fiber F1) and stainless steel wire. (a−d) Immunohistochemical comparison of tissue reaction to chronically implanted Fiber F1 (n=3) and conventional stainless steel probes (n=3) after four-week implantation. Neurons were labeled with NeuN (cyan), astrocytes with GFAP (green), and microglia with Iba1 (red). (Maximum intensity projections of 50 optical sections covering entire slice thickness taken at the implantation site). (b,e) Neuron density, calculated by counting NeuN labeled neurons, was not significantly different between the groups. (c,f) Astrocyte and microglia (d,g) reactivity, measured as the area of GFAP- or Iba1-positive cells respectively, were not significantly different between groups. Significance was determined by student's t-test. Error bars on bar graphs reflect the standard deviation. Two-to-three brain slices from each mouse (n=3) per experimental group were used for immunohistochemical analysis. Representative images were chosen to reflect the mean value of quantitative data. (Scale bar: 40 µm)

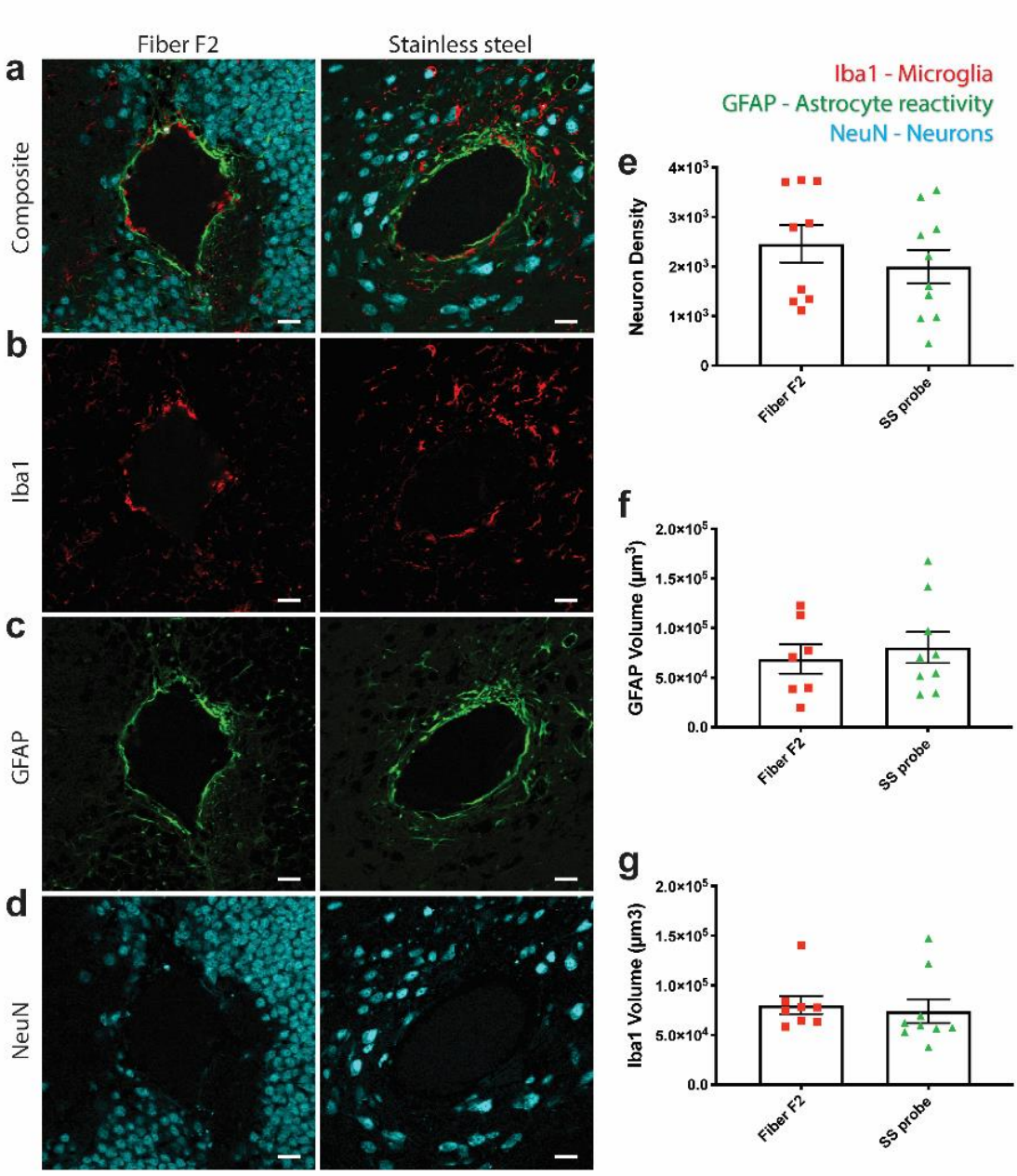

Figure 2.19 Immunohistochemical comparison of tissue reaction to chronically implanted multimodal Fiber F2 and conventional stainless steel probes after four-week implantation. (a−d) Single confocal optical sections were taken at electrode implantation site. Neurons were labeled with NeuN (cyan), astrocytes with GFAP (green), and microglia with Iba1 (Red). (d,e) Neuron density, calculated by counting NeuN labeled neurons, was not significantly different between the groups. (c,f) Astrocyte and microglia (b,g) reactivity, measured as the volume of GFAP- or Iba1-positive cells respectively, was not significantly different between groups. Significance was determined by student's t-test. Error bars on bar graphs reflect the standard deviation. (Scale bar: 40 µm)

2.3 Materials and methods

Multifunction fiber fabrication Many fiber structures have been prepared in this study. They all start from the preform fabrication which we described in detail below. After the preform fabrication, the macroscopic preform was put into a customized furnace. With controlled temperature and stress, the preform was drawn into thin fibers. The temperature we used during fiber drawing are 140 °C (top), 285 °C (middle), and 110 °C (bottom).

For fibers used as spatially expandable probes to detect seizure activity (F1), two rectangular grooves were machined on the PC rod, one of them was filled by a BiSn electrode while the other one remained hollow as a fluidic channel. Then the pre-structured rod was wrapped with a few layers of PVDF and an additional PC layer which subsequently formed a preform after the consolidation process.

For spatially expandable fiber probes with optical stimulation capability (F2), a thin layer of PVDF and a relatively thicker layer of PC were added to a PC rod. Two grooves were then machined on this thicker PC layer while one of them was filled by the BiSn electrode. Two layers of PVDF and PC were subsequently wrapped around the rod and put in the oven for the consolidation process.

For fibers with four electrodes to probe for the seizure activities in wild-type mice (F3), four rectangular grooves were machined on a PC rod and all of them were filled with BiSn electrodes. Then a few layers of PVDF and PC were wrapped around the structure and then consolidated.

For fibers used in the *Thy1-ChR2-YFP* mice (F4), we first rolled five layers of PVDF film (Mcmaster) and polycarbonate films (laminated plastics) onto a PC rod (Mcmaster), which subsequently formed a solid rod after the consolidation process in vacuum at 200 ºC. Next, we machined four rectangular grooves (2mm x 2mm) on the solid PC layer which were filled by the BiSn (Indium Corporate) electrodes. Then, a few layers of PVDF were rolled onto the electrode-filled rod to form the insulating layer, which was then followed by additional layers of PC for the stable thermal drawing process.

For fibers used in the demonstration of a multifunctional fiber with multisite drug delivery capability (Fiber S1), a thin layer of PVDF followed by layers of PC films were first rolled onto a

PC rod. After the consolidation of the films, six grooves were machined on the outer PC layer and two of them were filled with the BiSn electrodes. Then additional PVDF and PC layers were added to the rod to form the complete preform structure.

For fibers with eight waveguides, four electrodes, and one hollow channel (Fiber S2) a two-step drawing process was used. We first drew a rectangular waveguide fiber consisting of a PC core and a PMMA cladding. Then twelve grooves were machined on a PC tube (fabricated by wrapping PC films onto a Teflon rod and consolidating then), and four of them were inserted with CPE (conductive polyethylene) electrodes while the other eight were filled with the waveguide fibers. After that, additional PVDF and PC layers were wrapped onto the PC rod and consolidated.

For spatially expandable fiber probes fabrication, obtaining proper scaffolding fiber is crucial. This was achieved by putting four or seven PC tubes together with a thin layer of PC films as protection. Taking the advantages of the rotating motor on our customized fiber drawing tower, the fiber formed a helix structure due to the rotational degree of the rotating motor. The rotating motor was controlled by a motor and the rotational speed varies corresponding to the voltage applied to the motor. The voltage used in this study include 0, 3.3 V, 4.1 V, 5.0 V, 5.7 V, 6.5 V, 7.2 V, and 8.0 V, resulting in rotational speed of 0, 60 r/min, 69 r/min, 93 r/min, 108 r/min, 129 r/min, 147 r/min, and 162 r/min, respectively.

Electrochemical Impedance Spectrum First, fiber probes of two centimeters were prepared and the inner electrodes were electrically connected to the copper wire (connecting details in Neuro Probes Assembly). The impedance Spectrum results were acquired via a potentiostat (Interface 1010E, Gamry Instruments). During the measurements, two-electrode experiments were performed with fiber probes as a working electrode, Pt wire (Basi) as counter electrode and reference electrode and 1x phosphate-buffered saline (PBS, Thermo Fisher) as electrolyte by an AC voltage of 10mV (10 Hz – 100 kHz).

Stiffness measurements The stiffness test was carried out using a dynamic mechanical analyzer (DMA Q800, TA Instruments) installed with the single cantilever module. The tested fiber length is 10 mm, which equals to the distance between the fixed and movable clamps. The vibrating magnitude is 20 μm. We tested the stiffness of the fibers together with steel wire as the comparison

group under different frequencies ranging from 0.01Hz to 10 Hz. Three repeated measurements of each sample sets were taken at a temperature of 37°C.

Optical properties characterization To obtain the optical transmission spectra, we connected a halogen light source (DH1000, Ocean Optics) to the optical waveguide using the ferrule-to-ferrule coupling method. The transmitted light was collected at the other side of the fiber with a fiber-coupled spectrometer (Flame, 200-1,025nm, Ocean Optics). The transmission spectra are normalized by a light source spectrum. To quantify the transmission loss, the fiber probe ferrule end was coupled to a silica fiber patchcord by a mating sleeve (Thorlabs) which was air-coupled to a DPSS laser (Laserglow Technologies, 100 mW maximum power, wavelength λ = 473 nm) and the light output was measured by a power meter (Thorlabs) with a photodetector (Thorlabs) attached. Measurements were taken of fiber length of 1 - 10 cm, radii of curvature 1/8, 1/4, 3/8, 1/4, and 5/8 inch at a bending angle of 0° and 90°.

Femtosecond laser micromachining The fiber was immersed in dichloromethane for two minutes to remove the sacrificial outer PC layer before the micromachining process. The femtosecond(fs) laser used in the fabrication is a Ti: Sapphire NIR-fs pulsed laser (Coherent Libra series) with 800 nm emission wavelength, ~100 fs pulse width, and 3mm- beam-waist linear polarized Gaussian beam. A Nikon dry objective (20×, NA=0.4) was used to focus the laser beam on the fiber. The size of the focal area, D, is estimated at about 1.7 μm in diameter via $D=2\lambda f/\pi w_0$, where λ is the wavelength of the laser in the medium, f is the focal length of the lens, and w 0 is the input beam waist. The fiber was then mounted in an assembled motorized stage with a three-axis translation movement (ASI LX-4000 and Newport UTM50CC) and one-axis rotation around fiber axial direction (Thorlabs PRM1Z8). The fiber was fixed under tension to avoid wobbling during the fabrication. Since the laser beam only evaporates the material in the focal area, micro-channel can be formed at any selected location by scanning the focused laser beam layer-by-layer from the surface. The average power used in the fabrication was 0.5 mW with the laser repetition frequency of 100 Hz. The scanning speed was 0.4 mm/s and the overlapping between each trace was around 1 μm. A reflected light microscopic system using the same objective was also implemented to monitor the fabrication in real-time. To characterize exposed microfluidic windows, 1 μl each of four different diluted food color dye (red, green, blue and copper, Wilton) was injected to separate microfluidic channels in the fiber through tubing connected to a standard precision injection

apparatus (100 nl/s, NanoFil Syringe and UMP-3 Syringe pump, World Precision Instruments) while the fiber probe was embedded in 0.6% agarose gel (see details of tubing connection in Multifunctional Neuro Probes Assembly).

Light scattering pattern measurement The fiber was immersed in a drop of fluorescein solution (1% Uranine, Carolina Biological Supply Company) and excited by a 473 nm laser via butt coupling. The image was taken by an optical microscopy and the excitation light was filtered.

Simulation of the exposed waveguide The simulation was run by COMSOL Multiphysics© 5.5 equipped with frequency-domain electromagnetic wave solver on a workstation. Due to our limited computing power, two-dimensional simulation was preformed and it is enough to provide a qualitative evaluation. The dimension and geometry were determined by the microscopic image of the fabricated fiber. The waveguide has 11.5 μm thick PC core and 5 μm thick PMMA cladding. The exposed window is 20 μm x 20 μm wide and 7.5 μm depth with ~15^{o} tapering. The side and bottom of the exposed window are roughened (R_a=0.5 μm and 1μm for side and bottom respectively) to mimic the actual surface morphology of a femtosecond laser processed surface. The waveguide core is illuminated evenly with a 473 nm light and the corresponding refractive index of different layers are 1.6023 (PC),1.4976 (PMMA) and 1.3361 (water).

Multifunctional Neuro Probes Assembly For depth-dependent fiber probes used in *Thy1-ChR2-YFP* mice, the fiber probe was first put into the fiber optical ferrule and affixed by a retaining compound (LOCTITE) after micromachining process. Then the ferrule top part was polished by optical polishing papers from the roughness of 30um to 1um. Next, for electrical connection with the electrodes embedded in the fiber probe, the electrodes were exposed manually at different locations along the fiber length by a razor blade and silver paint (SPI Supplies) was applied to the manually exposed site individually. Then copper wires were wrapped around the fiber probe and additional silver paint was applied for a better connection. The wires were soldered to the pin connectors (Sullins Connector Solutions) while a stainless steel wire was soldered as a ground wire. Besides, 5-min epoxy (Devcon) was applied to the electrical and optical interface for affixation and electrical insulation. In the last step, we applied medical epoxy on the fiber probe tip area to prevent double exposure of the electrode during the electrophysiology recording process.

For spatially expandable fiber-based neural probes assembly, the sacrificial layer of the fiber probe was removed by dichloromethane immersion. To build microfluidic interfaces, the hollow channel of the fiber probe was exposed manually and then the fiber probe was inserted into the ethylene vinyl acetate tubing (0.5mm inner diameter) with the help of a needle syringe, resulting in the perpendicular positions of fiber probe and tubing with fiber probe's microfluidic exposure site placed in the tubing center. Then 5-min epoxy was applied around the connection site to prevent leakage during microfluidic infusion to the fiber probe through the tubing. The electrical and optical interface connection was established via the methods described above. After the soldering process, fiber probes were inserted to the 5-channel scaffolding fiber manually and followed by the affixation process of the whole device with 5-min epoxy.

After the devices are fabricated, we will test their electrical, optical, and chemical functions before implant surgery to ensure all of the implanted devices are functional in the acute and long-term experiments.

Surgical Procedure All animal procedures were approved by Virginia Tech Institutional Animal Care and Use Committee and Institutional Biosafety Committee and were carried out in accordance with the National Institutes of Health Guide for the Care and Use of Laboratory Animals. Five to nine weeks old male wild type C57BL/6J mice (Jackson Laboratory) were received from the Jackson Laboratory (Bar Harbor, ME) and allowed to acclimate for at least 3 days before enrolling them in experiments. *Thy1-ChR2-YFP* mice were bred in our lab (Jackson Laboratory). Mice had access to food and water ad libitum and were kept in a facility maintained for 12 hours light/dark cycle starting at 7 AM. Male C57BL/6J mice were set up on a stereotaxic apparatus (David Kopf Instruments) and 1-3.5% isoflurane was induced to animals via nose cone during all procedures for anesthesia. To expose the scalp, a small incision was made on the skin along the midline then a small craniotomy was made with a dental drill. Then the assembled fiber probe was lowered using a micropositioner with respect to the Mouse Brain Atlas while the ground stainless steel wire was soldered to a miniaturized screw (J.I.Morris) on the skull. Finally, the whole exposed skull area was fully covered by a layer of Metabond (C&B METABOND; Parkell) and dental cement.

For surgeries with spatially expandable fiber probes used in spike and burst suppression recording, we first positioned the scaffolding fiber to the coordinates relative to bregma of -1.8 mm AP, 1.5 mm ML, -1 mm DV and affixed the scaffold using Metabond. Then the functional fiber probes were further inserted for 1 mm and the final coordinates of the five individual probes are (-1.8 mm AP, 1.3 mm AL, -2 mm DV), (-2 mm AP, 1.5 mm ML, -2 mm DV), (-1.8 mm AP, 1.5 mm ML, -2 mm DV), (-1.8 mm AP, 1.7 mm ML, -2 mm DV), and (-1.6 mm AP, 1.5 mm ML, -2 mm DV).

For surgeries with depth-dependent fiber probes in *Thy1-ChR2-YFP* mice, the coordinates relative to bregma used were -2 mm anteroposterior (AP); 1 mm mediolateral (ML); -3.3 mm dorsoventral (DV, four electrodes at -1 mm, -1.5 mm, -2.5 mm and -3.2 mm, respectively). For surgeries with drug intervention on *Thy1-ChR2-YFP* mice, the coordinates relative to bregma used were -2 mm AP, 1.5 mm ML, -3.2 mm DV.

For depth-dependent fiber probes used in seizure study with the straight implant, the coordinates relative to bregma used were -2 mm AP, 2 mm ML, -4.5mm DV with four electrodes at -1 mm, -1.5 mm, -2.5 mm and -4.4 mm, respectively. For depth-dependent fiber probes used in seizure study at a 30° angled implant, the coordinates relative to bregma used were -2 mm AP, 1.5 mm ML (at the brain surface) and the distance of each exposed electrode from the brain surface was 0.5 mm (CTX), 1.3 mm (CA1), 2.2 mm (CA3) and 4.8 mm (AMG). The location of the electrode in the brain was verified in the coronal brain slices (50 µm thickness) after completion of the recording. The brain slices were stained for cell nuclei using DAPI to visualize clearly the damage caused by electrode implants (**Figure 2.20**).

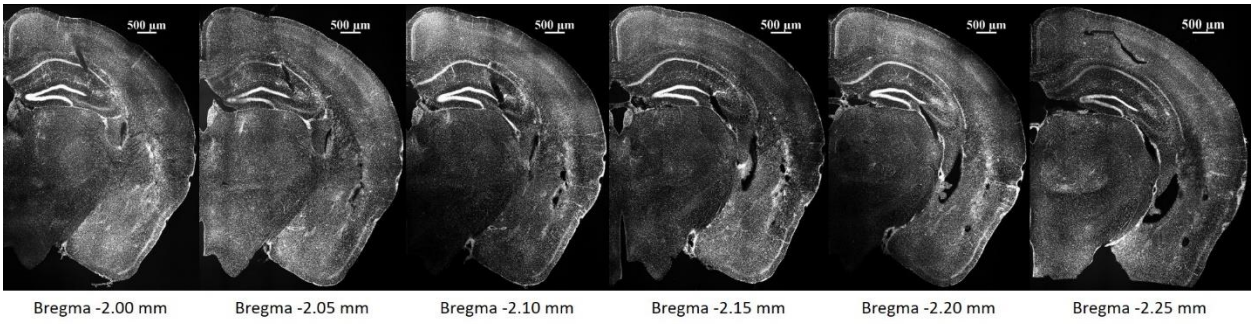

Figure 2.20 Location of depth-dependent fiber probe implanted angularly to the brain surface for electrophysiological recording. Mice brains collected at the end of electrographic recordings were sliced (50 µm thickness) and stained with DAPI to visualize cell nuclei. Serial coronal sections from 2.00 to 2.25 mm posterior to bregma are shown from left to right. Diagonal

cut mark seen in each slice indicates location of the electrode implanted to target cortex, CA1 and CA3 regions of hippocampus, and amygdala.

For surgeries with spatially expandable fiber probes used in *Thy1-ChR2-YFP* mice, we first lowered the scaffold to the coordinates of -1.5 mm AP, 0.5 mm ML and -2.5 mm DV relative to bregma. Then the scaffold was affixed to the scalp via Metabond while the fiber branches were further inserted into the brain for 1.5 mm after the Metabond was completely dry. Dental cement was used to affix the whole device above the skull. And the coordinates of the five electrodes are (-1.53 mm AP, 0.25 mm ML, -4 mm DV), (-1.75 mm AP, 0.53 mm ML, -4 mm DV), (-1.5 mm AP, 0.5 mm ML and -4 mm DV), (-1.47 mm AP, 0.75 mm ML, -4 mm DV), and (-1.25 mm AP, 0.47 mm ML, -4 mm DV).

For surgeries with spatially expandable fiber probes used in *Thy1-ChR2-YFP* mice to induce the seizure-like aftercharges, the coordinates of the scaffolding fiber is -2 mm AP, 1.5 mm ML, -0.6 mm DV and the functional fiber probes were further inserted for 0.5 mm (-2 mm AP, 1.4 mm ML, -1.1 DV) to target cortex region, 1 mm (-2.15 mm AP, 1.5 mm ML, -1.6 DV) to target CA1 region rostrally, 1 mm (-1.85 mm AP, 1.5 mm ML, -1.6 mm DV) to target CA1 region caudally, and 1.5 mm (-2 mm AP, 1.75 mm ML, -2.1 mm DV) to target CA3 region.

For surgeries with spatially expandable fiber probes used in seizure study, the coordinates for the scaffold relative to bregma used here are -2 mm AP, 1.5 mm ML, -1 mm DV. The lengths of inserted functional fibers beyond the bottom of the scaffolding fiber were 0.5 mm (CA1), 1 mm (CA3), 2 mm (thalamus) and 2 mm (thalamus). And the coordinates of the four electrodes are (-2.1 mm AP, 1.5 mm ML, -1.5 mm DV), (-2 mm AP, 1.7 mm ML, -2 mm DV), (-1.6 AP, 1.5 mm ML, -3 mm DV), and (-2 mm AP, 1.1 mm ML, -3 mm DV).

Viral Infection Theiler's murine encephalomyelitis virus (TMEV) was generously provided by Drs. Karen S. Wilcox and Robert S. Fujinami, University of Utah. Mice were infected with TMEV as previously reported[61]. Mice were anesthetized using 3% isoflurane and kept under anesthesia using 2-3% isoflurane during the entire infection procedure. The injection area in the right hemisphere was disinfected with 70% ethanol and the injection site is pinpointed slightly medial to the equidistant point on the imaginary line connecting the eye and the ear. A William's collar syringe which contains a plastic jacket on the needle to expose only 2 mm of the needle was used

for injection to restrict the injection within the somatosensory cortex. About 20-25 µl of Daniels strain of TMEV solution containing 300,000-375,000 plaque forming units (PFU) of the virus was injected intracortically by inserting the needle at a 90° angle to the skull. The needle was kept in place for at least 1 minute before retracting slowly to prevent leakage.

In Vivo Electrophysiology For studies involving single-unit LFP investigation in wild type mice and for the measurement of optically-induced electrical activities in *Thy1-ChR2-YFP* mice, a 32 Channel Neurophysiology System (Tucker-Davis Technologies, TDT) was connected to the headpins of the implanted device after animals recovered from surgeries. For optical stimulation, the fiber probe was connected to the DSPP laser as mentioned above. During optical stimulation, a laser pulse with 5 ms pulse was used and the frequencies used were 10, 20, and 100 Hz. Stimulation was delivered in 0.6 s stimulation epochs every 5 seconds. For the drug intervention experiments, the concentration of 0.1 mM CNQX (Tocris) solutions in PBS was prepared and 2.5 µl of which was injected into the brain through fiber probe's hollow channel using NanoFil Syringe and UMP-3 Syringe pump system at the speed of 80 nl/s.

Video-electroencephalography (vEEG) After 4-7 days of recovery from the surgical procedure, mice were infected with TMEV as described above and enrolled for continuous vEEG recordings between 2 and 8 days post-TMEV infection. The MP160 data acquisition system and AcqKnowledge 5.0 software from BIOPAC Systems, Inc. were used to record electroencephalograms. The corresponding behavior of each mouse was recorded using Media Recorder 4.0 software (Noldus Information Technology) and M1065-L network camera (Axis communications). Mice were connected to EEG100C differential amplifiers (BIOPAC) using custom-adapted six-channel cable connectors (363-000 and 363-441/6, Plastics1) and six-channel rotating commutators (SL6C/SB, Plastics1). All the cables and electrical components were sufficiently shielded to minimize electrical noise. Food and water were freely accessible to mice during the entire vEEG recording. Video and EEG recordings were automatically synchronized using the Observer XT 14.1 software from Noldus Information Technology. EEG signals were bandpass-filtered (high pass filter: 0.5 Hz, low pass filter: 100 Hz), amplified, and digitized at a sampling frequency of 500 Hz.

Data Analysis Data analysis was performed with Matlab (The Mathworks) and custom scripts were used to sort neural spikes and analyze the local field potentials (LFPs). The activities were digitally filtered from 0.5-300 Hz and 300-5000 Hz to present single spike resolutions and LFP resolution. The spike sorting algorithm was implemented by filtering out individual spikes using standard deviation dependent threshold, reducing the dimensionality of the data via principal component analysis (PCA) and using unsupervised learning algorithms to separate out the clusters, such as K-means clustering. A custom Matlab script was also written to create spectrograms to visually support the analysis of the LFPs in both the time domain and the frequency domain. The EEG and video recordings were reviewed manually for the detection of seizures. Electrographic seizures were defined as fast rhythmic spikes or sharp-wave discharges with amplitudes at least two times higher than baseline and lasting for at least 5 s. EEG signals during the ictal period typically start with low amplitude spikes that gradually increase in amplitude during seizure progression and then gradually decrease in amplitude and frequency at the end of the seizure. Suppression of EEG baseline also commonly occurs following convulsive seizures corresponding to behavioral arrest in mice. By verifying these gradual rhythmic changes in EEG signals and the suppression of basal EEG activity, seizures were identified and artifacts were excluded from the analysis.

Immunohistochemistry Animals were implanted with a stainless-steel probe or a Fiber F1/F2 for 4 weeks and then anesthetized with a ketamine (20 mg/mL)/xylazine (2 mg/mL) solution and transcardially perfused with phosphate-buffered saline (PBS) (Fisher BP661-10) followed by 4% paraformaldehyde (PFA) (Electron Microscopy Sciences Cat. #15714-S) in PBS. Upon extraction, the brain was kept in 4% PFA overnight at 4□ºC and then placed into PBS containing 0.02% sodium azide (Sigma S8032). The brain was serially sectioned into 50□µm transverse slices on a Campden Instruments 5100mz vibratome. All slices were blocked for 1hr at room temperature in blocking solution that contained 50% goat serum (Millipore S26-100ML) and 0.01% Triton X-100 (Sigma T9284) in PBS containing 0.02% sodium azide. Slices were then subsequently blocked in 8.3% Affinipure Fab Fragment goat anti-mouse IgG solution in 1X PBS. After blocking, slices were incubated with primary antibodies diluted in blocking solution without Triton X-100 overnight at room temperature. Primary antibodies used included chicken anti-GFAP (abcam Cat. #ab4674, 1:1000), mouse anti-NeuN (Millipore Cat. #MAB377, 1:100), and rabbit anti-Iba1 (Wako Cat. #019-19741, 1:500). Following primary incubation, slices were washed six times with

PBS for 10 minutes at room temperature with agitation. Secondary antibodies diluted in blocking solution without Triton X-100 were added at room temperature for 1 hr. Secondary antibodies used included goat anti-chicken Alexa Fluor 488 (Jackson ImmunoResearch Cat. #103-545-155, 1:500) goat anti-mouse Alexa Fluor 647 (Jackson ImmunoResearch Cat. #115-605-062, 1:500) and goat anti-rabbit Cy3 (Jackson ImmunoResearch Cat. #111-165-144, 1:500). Slices were then washed six times with PBS for 10 min at room temperature with agitation. Slices were mounted on glass slides with VECTASHIELD Antifade Mounting Medium with DAPI (Vector Laboratories Cat. #H-1200). Optical sections were acquired using a A1R Nikon laser scanning microscope using a Plan Apo 20X/N.A.0.75 air objective. Quantification of the data was performed using NIS-Elements (Nikon Instruments Inc.). To compensate for variance in lesion size, the puncture wound area was measured, and circular inner and outer regions of interest (ROI) were generated to form an annulus with an area normalized to all slices ($A = \pi(R^2 - r^2)$). Neuron density was then calculated within the normalized area by counting NeuN labeled cell bodies using spot detection (Nikon Elements). Area analysis of IBA1 and GFAP labeled cells was performed by creating binary layers of the optical sections using the threshold tool and quantified using the measurement tool (Nikon Elements). Projection images were created using ImageJ (NIH) software.

Statistics Parametric statistical tests were used if the data were sufficiently normal distributed and variance within groups was sufficiently similar. Experimental designs with two comparison groups were analyzed by a two-tailed unpaired t-test and designs with more than two comparison groups were analyzed using analysis of variance (ANOVA). The effects of CNQX on electrophysiological recordings were analyzed by repeated measure one-way ANOVA and Tukey's multiple comparisons test. The power of electrographic recording obtained from different brain regions was compared by two-way ANOVA and Tukey's multiple comparisons test. The difference between the two groups was considered statistically significant with a p-value of less than 0.05. Significance of tissue reaction to chronically implanted multimodal Fiber F2 and conventional stainless steel probes after four-week implantation was determined by the student's t-test. All tests were performed using GraphPad Prism 8.0.

2.4 Conclusion

Here we presented the development and application of spatially expandable multifunctional fiber-based probes for mapping and modulating brain activities across distant regions in the deep brain. The multisite multifunctional interfaces along a single fiber are created using a femtosecond laser micromachining technique. Furthermore, the integration of a helix scaffolding fiber with multifunctional fiber arrays fully extends the capabilities of fiber-based neural probes from a 1D single-site interface to 3D multi-site brain interfaces. These probes provide a powerful platform for recording localized spike activities and field potentials and performing optogenetic and chemical modulation of the activities in spaced deep brain regions. Our customizable fiber probe is also readily compatible with commercial EEG setup allowing us to detect multiple foci and different brain activities among brain regions of interest in the TMEV-infected seizure model. Recordings in epileptic mice illustrate the power of the spatially expandable fiber probes to simultaneously record from distant brain regions allowing circuit analysis of the epileptic brain. In the future, a higher density of electrodes and optical or chemical interfacing sites in these spatially expandable fiber-based probes can be explored to enable a larger recording or stimulation sample. Closed-loop systems that combine the detection of seizure foci with localized intervention can be developed which can significantly improve the effective treatment of seizure before clinical onset. Finally, these probes can enable a leap forward towards the understanding the brain circuitry in the hard-to-access deep subcortical regions, and facilitate the development of new therapeutic methods for treating various brain diseases, including epilepsy, Parkinson's disease, addiction, depression, autism, etc.

2.5 References

1 Alivisatos, A. P. et al. Neuroscience. The brain activity map. *Science* **339**, 1284-1285(2013).

2 Buzsaki, G. Large-scale recording of neuronal ensembles. *Nat Neurosci* **7**, 446-451(2004).

3 Carandini, M. From circuits to behavior: a bridge too far? *Nat Neurosci* **15**, 507-509(2012).

4 Marblestone, A. H. et al. Physical principles for scalable neural recording. *Front Comput Neurosci* **7**, 137(2013).

5 Nicolelis, M. A., Ghazanfar, A. A., Faggin, B. M., Votaw, S. & Oliveira, L. M. Reconstructing the engram: simultaneous, multisite, many single neuron recordings. *Neuron* **18**, 529-537(1997).

6 Quiroga, R. Q., Reddy, L., Kreiman, G., Koch, C. & Fried, I. Invariant visual representation by single neurons in the human brain. *Nature* **435**, 1102-1107(2005).

7 Ekstrom, A. D. et al. Cellular networks underlying human spatial navigation. *Nature* **425**, 184-188(2003).

8 Jacobs, J. et al. Direct recordings of grid-like neuronal activity in human spatial navigation. *Nat Neurosci* **16**, 1188-1190(2013).

9 Creutzfeldt, O., Ojemann, G. & Lettich, E. Neuronal activity in the human lateral temporal lobe. I. Responses to speech. *Exp Brain Res* **77**, 451-475(1989).

10 Viventi, J. et al. Flexible, foldable, actively multiplexed, high-density electrode array for mapping brain activity in vivo. *Nat Neurosci* **14**, 1599-1605(2011).

11 Zhao, Z. T. et al. Nanoelectronic Coating Enabled Versatile Multifunctional Neural Probes. *Nano Lett* **17**, 4588-4595(2017).

12 Kim, T. I. et al. Injectable, cellular-scale optoelectronics with applications for wireless optogenetics. *Science* **340**, 211-216(2013).

13 Seymour, J. P. & Kipke, D. R. Fabrication of polymer neural probes with sub-cellular features for reduced tissue encapsulation. *Conf Proc IEEE Eng Med Biol Soc* **1**, 4606-4609(2006).

14 Xie, C. et al. Three-dimensional macroporous nanoelectronic networks as minimally invasive brain probes. *Nat Mater* **14**, 1286-1292(2015).

15 Sohal, H. S. et al. The sinusoidal probe: a new approach to improve electrode longevity. *Front Neuroeng* **7**, 10(2014).

16 Kozai, T. D. et al. Ultrasmall implantable composite microelectrodes with bioactive surfaces for chronic neural interfaces. *Nat Mater* **11**, 1065-1073(2012).

17 Potter, K. A., Buck, A. C., Self, W. K. & Capadona, J. R. Stab injury and device implantation within the brain results in inversely multiphasic neuroinflammatory and neurodegenerative responses. *J Neural Eng* **9** (2012).

18 Khodagholy, D. et al. NeuroGrid: recording action potentials from the surface of the brain. *Nat Neurosci* **18**, 310-315(2015).

19 Jun, J. J. et al. Fully integrated silicon probes for high-density recording of neural activity. *Nature* **551**, 232-236(2017).

20 Angotzi, G. N. et al. A Synchronous Neural Recording Platform for Multiple High-Resolution CMOS Probes and Passive Electrode Arrays. *IEEE T Biomed Circ S* **12**, 532-542(2018).

21 Rios, G., Lubenov, E. V., Chi, D., Roukes, M. L. & Siapas, A. G. *Nanofabricated Neural Probes for Dense 3-D Recordings of Brain Activity*. *Nano Lett* **16**, 6857-6862(2016).

22 Khodagholy, D., Gelinas, J. N. & Buzsaki, G. Learning-enhanced coupling between ripple oscillations in association cortices and hippocampus. *Science* **358**, 369-372(2017).
23 Fu, T. M. et al. Stable long-term chronic brain mapping at the single-neuron level. *Nat Methods* **13**, 875-882(2016).
24 Bjornsson, C. S. et al. Effects of insertion conditions on tissue strain and vascular damage during neuroprosthetic device insertion. *J Neural Eng* **3**, 196-207(2006).
25 Sejnowski, T. J., Churchland, P. S. & Movshon, J. A. Putting big data to good use in neuroscience. *Nat Neurosci* **17**, 1440-1441(2014).
26 Ahrens, M. B., Orger, M. B., Robson, D. N., Li, J. M. & Keller, P. J. Whole-brain functional imaging at cellular resolution using light-sheet microscopy. *Nat Methods* **10**, 413-429(2013).
27 Deisseroth, K. & Schnitzer, M. J. Engineering Approaches to Illuminating Brain Structure and Dynamics. *Neuron* **80**, 568-577(2013).
28 Alivisatos, A. P. et al. The Brain Activity Map Project and the Challenge of Functional Connectomics. *Neuron* **74**, 970-974(2012).
29 Piatkevich, K. D. et al. Population imaging of neural activity in awake behaving mice. *Nature* **574**, 413-417(2019).
30 Khodagholy, D. et al. Highly conformable conducting polymer electrodes for in vivo recordings. *Adv Mater* **23**, H268-H272(2011).
31 Chang, E. F. Towards large-scale, human-based, mesoscopic neurotechnologies. *Neuron* **86**, 68-78(2015).
32 Patel, S. R. & Lieber, C. M. Precision electronic medicine in the brain. *Nat Biotechnol* **37**, 1007-1012(2019).
33 Liu, J. et al. Syringe-injectable electronics. Nat Nanotechnol **10**, 629-636(2015).
34 Zhou, T. et al. Syringe-injectable mesh electronics integrate seamlessly with minimal chronic immune response in the brain. *P Natl Acad Sci USA* **114**, 5894-5899(2017).
35 Bancaud, J. et al. Functional stereotaxic exploration (SEEG) of epilepsy. *Electroencephalogr Clin Neurophysiol* **28**, 85-86 (1970).
36 Shin, H. et al. Multifunctional multi-shank neural probe for investigating and modulating long-range neural circuits in vivo. *Nat Commun* **10**, 85-86(2019).
37 Wu, F. et al. Monolithically Integrated muLEDs on Silicon Neural Probes for High-Resolution Optogenetic Studies in Behaving Animals. *Neuron* **88**, 1136-1148(2015).
38 Son, Y. et al. In vivo optical modulation of neural signals using monolithically integrated two-dimensional neural probe arrays. *Sci Rep-Uk* **5** (2015).
39 Chen, J. K., Wise, K. D., Hetke, J. F. & Bledsoe, S. C. A multichannel neural probe for selective chemical delivery at the cellular level. *IEEE T Bio-Med Eng* **44**, 760-769(1997).
40 Cheung, K. C., Djupsund, K., Dan, Y. & Lee, L. P. Implantable multichannel electrode array based on SOI technology. *J Microelectromech* S **12**, 179-184(2003).
41 Li, Y., Baek, K., Gulari, M. & Wise, K. D. A drug-delivery probe with an, in-line flowmeter based on trench refill and chemical mechanical polishing techniques. *IEEE Sensor*, 1144-1147(2007).
42 Seidl, K. et al. In-plane silicon probes for simultaneous neural recording and drug delivery. *J Micromech Microeng* **20** (2010).
43 Seidl, K. et al. CMOS-Based High-Density Silicon Microprobe Arrays for Electronic Depth Control in Intracortical Neural Recording. *J Microelectromech S* **20**, 1439-1448(2011).

44 Cardin, J. A. et al. Targeted optogenetic stimulation and recording of neurons in vivo using cell-type-specific expression of Channelrhodopsin-2. *Nature Protocols* **5**, 247-254(2010).
45 Halassa, M. M. et al. Selective optical drive of thalamic reticular nucleus generates thalamic bursts and cortical spindles. *Nat Neurosci* **14**, 1118-1120(2011).
46 Han, X. et al. Millisecond-Timescale Optical Control of Neural Dynamics in the Nonhuman Primate Brain. *Neuron* **62**, 191-198(2009).
47 Kim, T. I. et al. Injectable, Cellular-Scale Optoelectronics with Applications for Wireless Optogenetics. *Science* **340**, 211-216(2013).
48 Kravitz, A. V. et al. Regulation of parkinsonian motor behaviours by optogenetic control of basal ganglia circuitry. *Nature* **466**, 622-U627(2010).
49 Lu, Y. et al. Poly(3,4-ethylenedioxythiophene)/poly(styrenesulfonate)-poly(vinyl alcohol)/poly(acrylic acid) interpenetrating polymer networks for improving optrode-neural tissue interface in optogenetics. *Biomaterials* **33**, 378-394(2012).
50 Rubehn, B., Wolff, S. B. E., Tovote, P., Luthi, A. & Stieglitz, T. A polymer-based neural microimplant for optogenetic applications: design and first in vivo study. *Lab Chip* **13**, 579-588(2013).
51 Voigts, J., Siegle, J. H., Pritchett, D. L. & Moore, C. L. The flexDrive: an ultra-light implant for optical control and highly parallel chronic recording of neuronal ensembles in freely moving mice. Front Syst Neurosci 7(2013).
52 Zhang, J. Y. et al. Integrated device for optical stimulation and spatiotemporal electrical recording of neural activity in light-sensitized brain tissue. *J Neural Eng* **6** (2009).
53 Kravitz, A. V., Tye, L. D. & Kreitzer, A. C. Distinct roles for direct and indirect pathway striatal neurons in reinforcement. *Nat Neurosci* **15**, 816-U823(2012).
54 Canales, A. et al. Multifunctional fibers for simultaneous optical, electrical and chemical interrogation of neural circuits in vivo. *Nat Biotechnol* **33**, 277-284(2015).
55 Park, S. et al. One-step optogenetics with multifunctional flexible polymer fibers. *Nat Neurosci* **20**, 612-619(2017).
56 Guo, Y. et al. Polymer Composite with Carbon Nanofibers Aligned during Thermal Drawing as a Microelectrode for Chronic Neural Interfaces. *Acs Nano*, **11**, 7, 6574–6585(2017).
57 Robbins, A. A., Fox, S. E., Holmes, G. L., Scott, R. C. & Barry, J. M. Short duration waveforms recorded extracellularly from freely moving rats are representative of axonal activity. *Front Neural Circuits* **7**, 181(2013).
58 Ching, S., Purdon, P. L., Vijayan, S., Kopell, N. J. & Brown, E. N. A neurophysiological-metabolic model for burst suppression. *Proc Natl Acad Sci USA* **109**, 3095-3100(2012).
59 Williams, A. J., Zhou, C. & Sun, Q. Q. Enhanced Burst-Suppression and Disruption of Local Field Potential Synchrony in a Mouse Model of Focal Cortical Dysplasia Exhibiting Spike-Wave Seizures. *Front Neural Circuits* **10**, 93(2016).
60 Osawa, S. et al. Optogenetically induced seizure and the longitudinal hippocampal network dynamics. *Plos One* **8**, e60928(2013).
61 Patel, D. C. et al. Hippocampal TNFalpha Signaling Contributes to Seizure Generation in an Infection-Induced Mouse Model of Limbic Epilepsy. *eNeuro* **4** (2017).
62 D.C. Patel, K.S. Wilcox. Models of Seizures and Epilepsies (2nd ed.) Ch. 46, (Elsevier Press, 2017).

63 Stewart, K. A., Wilcox, K. S., Fujinami, R. S. & White, H. S. Development of postinfection epilepsy after Theiler's virus infection of C57BL/6 mice. *J Neuropathol Exp Neurol* **69**, 1210-1219(2010).
64 Stewart, K. A., Wilcox, K. S., Fujinami, R. S. & White, H. S. Theiler's virus infection chronically alters seizure susceptibility. *Epilepsia* **51**, 1418-1428(2010).
65 Smeal, R. M. et al. The activity within the CA3 excitatory network during Theiler's virus encephalitis is distinct from that observed during chronic epilepsy. *J Neurovirol* **18**, 30-44(2012).
66 Aroniadou-Anderjaska, V., Fritsch, B., Qashu, F. & Braga, M. F. M. Pathology and pathophysiology of the amygdala in epileptogenesis and epilepsy. *Epilepsy Res* **78**, 102-116(2008).
67 Kwon, O. Y. & Park, S. P. Depression and anxiety in people with epilepsy. *J Clin Neurol* **10**, 175-188(2014).

Chapter 3

Nano-optoelectrodes integrated with flexible multifunctional fiber probes by high-throughput scalable fabrication

3.1 Introduction

By supporting surface plasmon modes to concentrate optical fields at the nanoscale, plasmonic metal nanostructures can serve as optical nanoantennas to achieve ultrasensitive spectroscopic bio-/chemical sensing. In particular, the refractive index (RI) plasmonic sensors can monitor surface binding events of biomarker molecules by resolving RI-dependent spectral shifting of surface plasmon resonances[1-3]; and surface-enhanced Raman spectroscopy (SERS) plasmonic sensors can provide vibrational finger-print spectra of analyte molecules by enhancing both excitation and inelastic scattering processes in hot spots[4-6]. In the attempts of creating plasmonic metal nanostructures onto the tips of optical fibers for *in-situ* remote optical biosensing[7], a new technology called "Lab on Fiber" has been developed[8-12]. Most of these previous works have used bottom-up or top-down nanofabrication methods such as self-assembly surface-functionalization, electron-beam lithography, and focused-ion-beam patterning to integrate the plasmonic metal nanostructures with optical fibers.[7, 13-17] These approaches, however, have challenges for simultaneous achievement of good accuracy, throughput, and scalability in manufacturing nanoantennas integrated fiber systems, which limits their potential in real-world applications. Furthermore, plasmonic nanoantennas consisting of high-conductivity noble metal nanostructures can also function as nanoelectrodes with a large electrochemical surface-to-volume ratio for high-performance electrical recording[18], and thus can essentially serve as nano-optoelectrodes for hybrid optical-electrical sensing in biochemical systems.

For *in vivo* electrical biosensing, silicon-based microelectrode arrays by top-down semiconductor fabrication process has become a robust and scalable technology to enable multichannel monitoring of neural activities in the brain[19-22], which, however, face difficulties in long-term *in vivo* operation due to the mismatch of the biomechanical properties between the soft brain tissue and rigid devices. Furthermore, most of the silicon-based devices are limited to single functionality. Recently, flexible multimaterial multifunctional fiber probes have proved their superiority not only in the outstanding biomechanical compatibility to allow chronic in vivo electrical recording at a single-cell level but also in bi-directional *in vivo* communication capability for both optical and electrical biosignals. Therefore, multimaterial multifunctional fiber probes can be used as a combined optical-electrical transmission line platform to integrate with nano-optoelectrodes at the fiber probe tip for hybrid optical-electrical bio-interfacing at a single-cell level *in vivo*.

In this work, we demonstrate the integration of dense nano-optoelectrode arrays onto the tips of multifunctional optoelectrical fibers by high-throughput scalable fabrication. The multifunctional fibers are fabricated using a convergence fiber drawing technique, which allows for polymer electrodes and silica waveguides to be co-drawn into a flexible micron-sized fiber device. The dense arrays of nano-optoelectrodes composed of Au/Ag nanolaminated nanodisks are created on the tips of flexible multifunctional probes by electron beam deposition of alternating metal layers through free-standing nanohole array masks. This unique surface modification enables us to detect chemicals through fiber tip via RI optical sensing and SERS molecular detection, which holds great potential to sense biomarkers *in-vivo.* Beyond optical sensing, we demonstrate that the nano-optoelectrodes can improve the electrical recording performance of the polymer composite electrodes by reducing the impedance of the electrodes. Moreover, we were

able to record neural activity from the hippocampus region of mouse brains 28 weeks post-implantation demonstrating good biocompatibility of these integrated probes for potential chronic implant applications.

3.2 Results and discussion

3.2.1 Fabrication of nano-optoelectrodes on multifunctional fibers

In previously reported studies[23-25], Canales *et al.* developed multifunctional fiber-based neural interfaces using a polymer waveguide and surrounding polymer electrodes. However, the large transmission loss in this kind of polymer waveguides makes it unsuitable for ultrasensitive optical sensing. To address this issue, we draw a multifunctional polymer fiber with a silica fiber in the center. Two conductive polymer electrodes (conductive polyethylene, CPE) were incorporated into a macroscopic preform via a machining process while the center of the preform remained hollow (**Figure 3.1a**). We then inserted the silica fiber with polyimide coating into the center orifice, which was then pulled down to converge with the surrounding polymer during the thermal drawing process shown in **Figure 3.1b**[26, 27]. The optical property of the silica fiber was not altered during the fiber drawing process based on the transmission spectrum measurement before and after drawing (**Figure 3.2**). The drawn fibers were cut, bundled, and inserted into an alumina tube and fixed using Phenyl salicylate (**Figure 3.1c(i)**). After the fixation, the bundle was polished on lapping films resulting in sub-micron roughness for deposition in the next step. Following the transfer of the nanohole array mask (nanohole diameter = 130 nm, periodicity = 400 nm) onto the tip surface of the polymer fiber bundle (**Figure 3.1c(ii)**), we used electron-beam evaporation to deposit a 1-nm thick Ti adhesion layer, and alternating Au and Ag layers (thickness = 25, 6, 25, 8, 25 nm from bottom to top) as shown in **Figure 3.1c(iii)**[28, 29]. Next, the scotch tape was used to remove the nanohole array mask (**Figure 3.1c(iv)**), leaving the periodic nano-

optoelectrodes on the tip of the fibers (**Figure 3.1c(v)**). The use of Au nanohole array mask can result in a high-yield and reproducible fabrication process of nano-optoelectrodes, compared to other nanofabrication techniques, such as e-beam lithography. As described in our previous work[28, 29], the Au nanohole array mask is fabricated on a 3-inch wafer and can be cut into pieces depending on the substrate size in use. After the nanohole array mask transfer process, only one e-beam evaporation and lift-off process is needed to integrate the plasmonic nano-optoelectrodes with the multifunctional fibers. And the structure of the nano-optoelectrodes has been optimized based on our previous work[30].

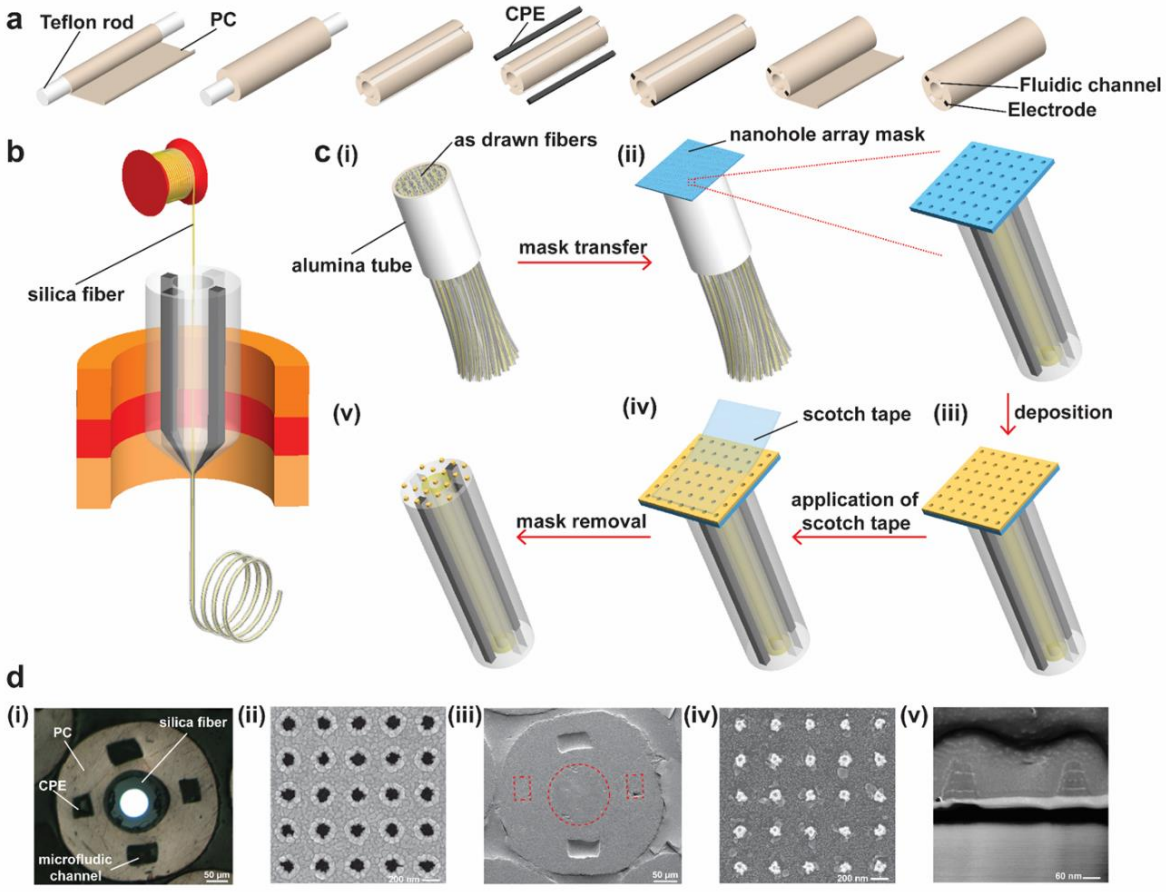

Figure 3.1 Fabrication of nano-optoelectrodes on multifunctional fiber tips. (a) A schematic showing the fabrication process of the preform with two electrodes, two fluidic channels, and a hollow core. (b) An illustration of the fiber drawing process. The silica fiber was inserted into the center hole and converged with the polymer material during the thermal drawing process. (c) Schematic illustration of the process of integrating the nano-optoelectrodes on the fiber tips: (i) As-drawn fibers were cut, bundled, and inserted into an alumina tube; (ii) After the fixation and

polishing process, a nanohole array mask was transferred to the top surface of the bundle; (iii) Following the mask transfer, layers of Ti, Au, and Ag were deposited onto the polymer fiber bundle tip via e-beam evaporation; (iv) The nanohole array mask was peeled off using scotch tape, leaving behind the periodic nanostructures as shown in (v). (d) Optical and SEM images of the multifunctional fiber, nanohole array mask, and the nano-optoelectrodes: (i) Optical image of the as-drawn multifunctional fiber in the bundle after polishing; (ii) SEM image of the nanohole array mask; (iii) SEM image of the fiber tip with periodic nano-optoelectrodes deposited; (iv) A zoomed-in SEM image showing the nano-optoelectrodes on the silica fiber; (v) A cross-sectional SEM image of the nano-optoelectrodes.

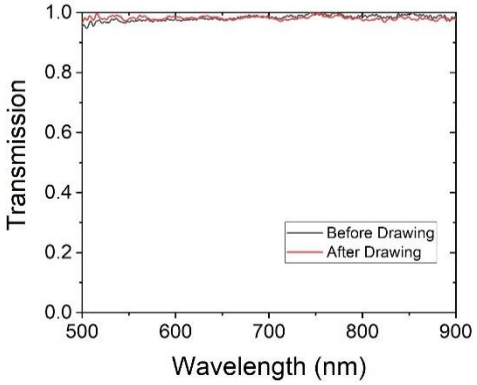

Figure 3.2 Transmission spectra of the silica fiber before drawing and in the drawn multifunctional fiber.

Figure 3.1d(i) shows a cross-sectional optical image of an as-drawn fiber in the bundle after polishing. To investigate the structure of the nanohole array mask and nano-optoelectrodes on the fiber tips, we used a Scanning Electron Microscope (SEM) to characterize the nanostructures of the mask as shown in **Figure 3.1d(ii)**. **Figure 3.1d(iii)** shows the SEM image of the as-drawn multifunctional fiber with nano-optoelectrodes deposited**,** and **Figure 3.1d(iv)** presents a zoomed-in SEM image of nano-optoelectrodes on the silica fiber tip surface. To further validate the layers of the nano-optoelectrode, the Focused Ion Beam (FIB) technique was utilized, and the corresponding cross-sectional SEM image of the nano-optoelectrodes is shown in **Figure 3.1d(v)**.

3.2.2 Refractive index sensing and SERS measurement

In order to examine the optical properties of nano-optoelectrode arrays on fiber, we conducted optical extinction measurements through the fiber tip surface at the normal-incident angle. As shown in **Figure 3.3a** (solid line), the extinction spectrum shows a major peak at ~ 705 nm for the localized surface plasmon resonance in nanolaminated Au-Ag-Au nano-optoelectrode arrays. The calculated extinction spectrum by 3D finite-difference time-domain (FDTD) methods also reveals a distinct resonant peak at 697 nm (dashed line in **Figure 3.3a**) in good agreement with the measurements. The FDTD-calculated $|E|^2$ distribution map (**Figure 3.3a** inset) reveals that the localized surface plasmon mode has the electric dipole nature with intense optical fields, mostly concentrated at the bottom edges of individual nano-optoelectrodes. Compared to the calculation, the resonant feature in the measurements shows a broader linewidth due to the inhomogeneous broadening effects from size variations between individual nanoantennas in the array.[30]

As the proof-of-concept demonstration for plasmonic RI sensing, we used nano-optoelectrodes integrated fiber probes to monitor the resonant shifts of plasmonic dipole mode in response to the RI changes in the background environment. The RI sensing measurements are conducted after acetone-IPA rinse cycles, demonstrating good stability of the nanostructures. Figure 2b depicts the measured extinction spectra for the optoelectrodes integrated fiber probes, respectively, in the air (n = 1), water (n = 1.33), ethanol (n = 1.36), isopropyl alcohol (IPA, n = 1.38), and butanol (n = 1.40). As the RI of surrounding medium increases, the plasmonic resonant peak redshifts from 667 nm (n = 1) to 703 nm (n = 1.33), 710 nm (n = 1.36), 711 nm (n = 1.38), and 714 nm (n = 1.4), respectively. By a linear regression fitting of the measured dependence between RIs and the relative spectral shifts of the resonant peaks, we can obtain a RI sensitivity of

~ 115.54 nm/RIU for the plasmonic nanodisk arrays (**Figure 3.3c**). The FDTD-simulated extinction spectra (**Figure 3.4**) in different background refractive index environments agree well with the measurements.

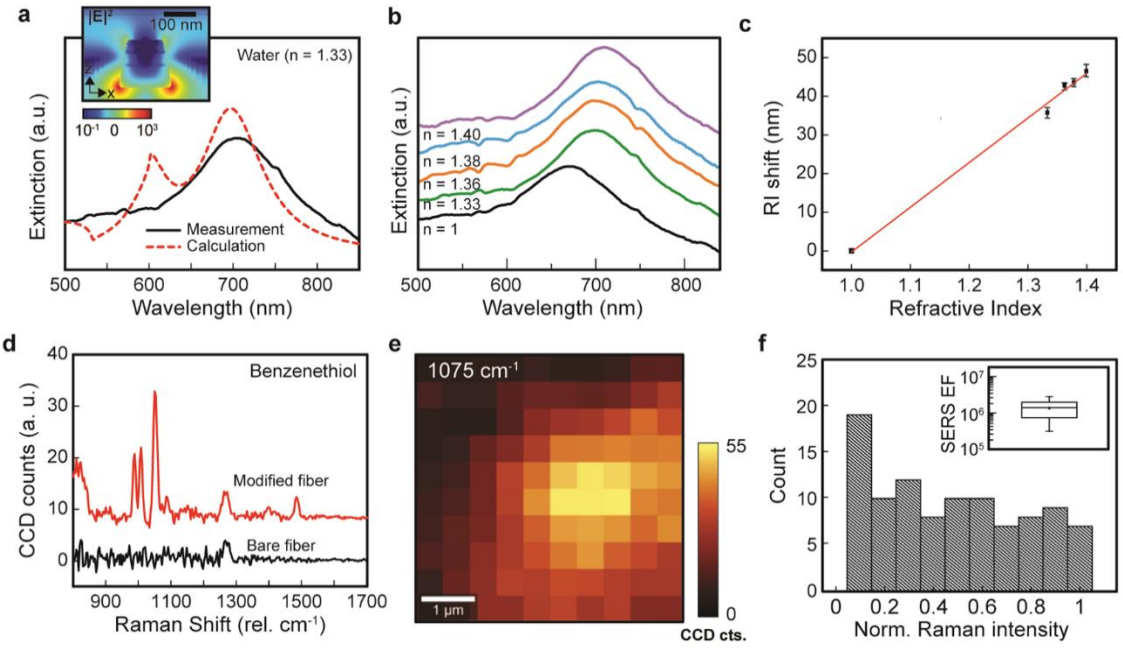

Figure 3.3 Refractive index sensing and SERS measurements from nano-optoelectrodes integrated fiber probes. (a) Measured and FDTD-calculated extinction spectra of nano-optoelectrode arrays on the fiber probes in the water show a distinct peak of localized surface plasmon mode. Inset: The FDTD-calculated x-z distribution map (697 nm). (b) Measured extinction spectra of nano-optoelectrodes integrated fiber probes with different background refractive index environments, including the air (n = 1), water (n = 1.33), ethanol (n = 1.36), IPA (n = 1.38), and butanol (n = 1.40). (c) The dependence of wavelength shifts of the resonant extinction peak on the refractive index changing from 1 to 1.40. (d) The measured average SERS spectra of BZT for fiber probes with and without the surface modification of nano-optoelectrode arrays. (e) 2D Raman image of a 5 μm × 5 μm area for the BZT Raman peak at 1075 cm-1. (f) Histograms of SERS intensities on the surface of nano-optoelectrodes integrated fiber probes. Inset: Calculated SERS EFs.

By measuring Raman spectra of benzenethiol (BZT) molecules functionalized on the surface of nano-optoelectrodes, we have examined the SERS performance of nano-optoelectrodes integrated fiber probes. As shown in **Figure 3.3d,** nano-optoelectrodes integrated fiber probes can induce intense BZT Raman signals featured by four notable BZT vibrational peaks at 1004 cm^{-1}

(the CCC ring in-plane bending mode), 1026 cm^{-1} (the CH in-plane bending mode), 1075 cm^{-1} (the CCC ring in-plane breathing mode with CS stretching mode), and 1578 cm^{-1} (the CC stretching mode). In contrast, the bare fiber probes without plasmonic nanostructures do not exhibit these characteristic BZT Raman peaks due to the lack of local optical field enhancement. **Figure 3.3e** shows the 2D confocal Raman images (at 1075 cm^{-1}) over a 5 μm × 5 μm area. For the analysis of SERS performance on nano-optoelectrodes at the fiber probe tip, we plotted the histograms of 1075 cm^{-1} Raman signal intensities from 10 × 10 pixels and found an average SERS enhancement factor (EF) of ~1.4 × 10^6 for the samples (Figure 2f). The SERS EFs were calculated by the formula:

$$EF = (I_{SERS}/I_{Raman}) \times (N_{Raman}/N_{SERS})^{31} \quad (1)$$

where I_{SERS}, I_{Raman}, N_{Raman}, and N_{SERS} are SERS BZT intensity, neat BZT Raman intensity, and the number of BZT molecules contributing to SERS and neat Raman intensities, respectively.

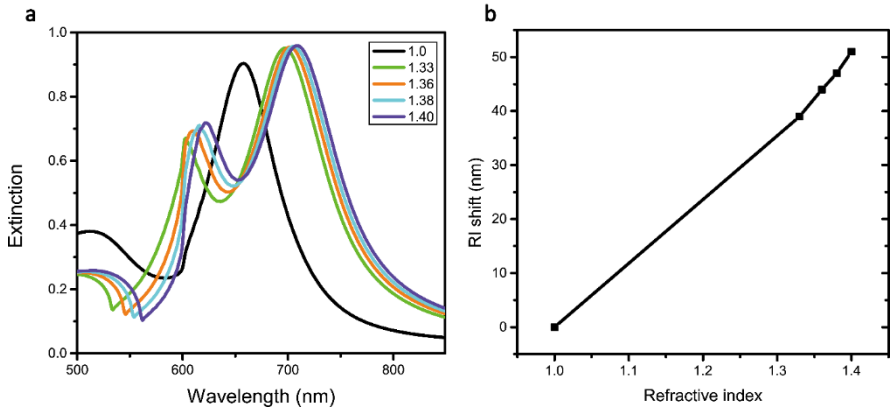

Figure 3.4 FDTD-simulated extinction spectra in different background refractive index environments. (a) FDTD-calculated extinction spectra of nano-optoelectrode arrays on the fiber probes with different background refractive index environments, including the air (n = 1), water (n = 1.33), ethanol (n = 1.36), IPA (n = 1.38), and butanol (n = 1.40). (b) The FDTD-calculated dependence of wavelength shifts of the resonant extinction peak on the refractive index changing from 1 to 1.40. By a linear regression fitting of the simulated dependence between RIs and the relative spectral shifts of the resonant peaks, a RI sensitivity of ~ 124.24 nm/RIU for the plasmonic nanodisk arrays is obtained.

3.2.3 Electrical characterization of the surface modified electrodes

To evaluate the effect of nano-optoelectrodes on the fiber electrodes, we compared the electrical performance of the fibers with surface modified and unmodified electrodes. In our previous study, we have proved that the impedance of the carbon nanofiber composite electrode (CNF-CPE) was significantly decreased compared with the conventional CPE electrode due to the alignment of the CNFs[24]. However, the impedance is still relatively high compared to other commonly used neural recording electrodes. Here, we deposited nano-optoelectrodes onto CNF-CPE electrodes using e-beam evaporation of Ti/Au/Ag/Au/Ag/Au with thicknesses of 1/25/6/25/8/25 nm by using the method shown in **Figure 3.1**, and measured the impedance spectra of the electrode. Figure 3a-b shows the bode plot of the impedance spectra acquired from a potentiostat using a three-electrode measurement method with the fiber electrode as the working electrode, a Pt wire as the counter electrode, and Ag/AgCl as the reference electrode. From the bode magnitude impedance plot (**Figure 3.5a**), we can observe an evident decrease in impedance for surface-modified electrodes at 1 kHz, a frequency where the action potential's firing frequency band was centered[32]. The bode phase plot (**Figure 3.5b**) also suggests that after surface modification, the electrode exhibits a less capacitive behavior while the unmodified electrode manifests a capacitor dominant behavior over the whole frequency range. For evaluating the performance of the surface-modified electrodes as a long-term neural implant device, the electrodes were soaked in 1X PBS solution for 30 days, and the impedance spectra were recorded daily. Figure 3c shows that the impedance of the surface-modified electrode at 1 kHz is relatively stable, with a slight decrease over time. This may result from the slightly porous structure of the electrode material as the unmodified electrode demonstrates the same decrease of impedance at 1 kHz.

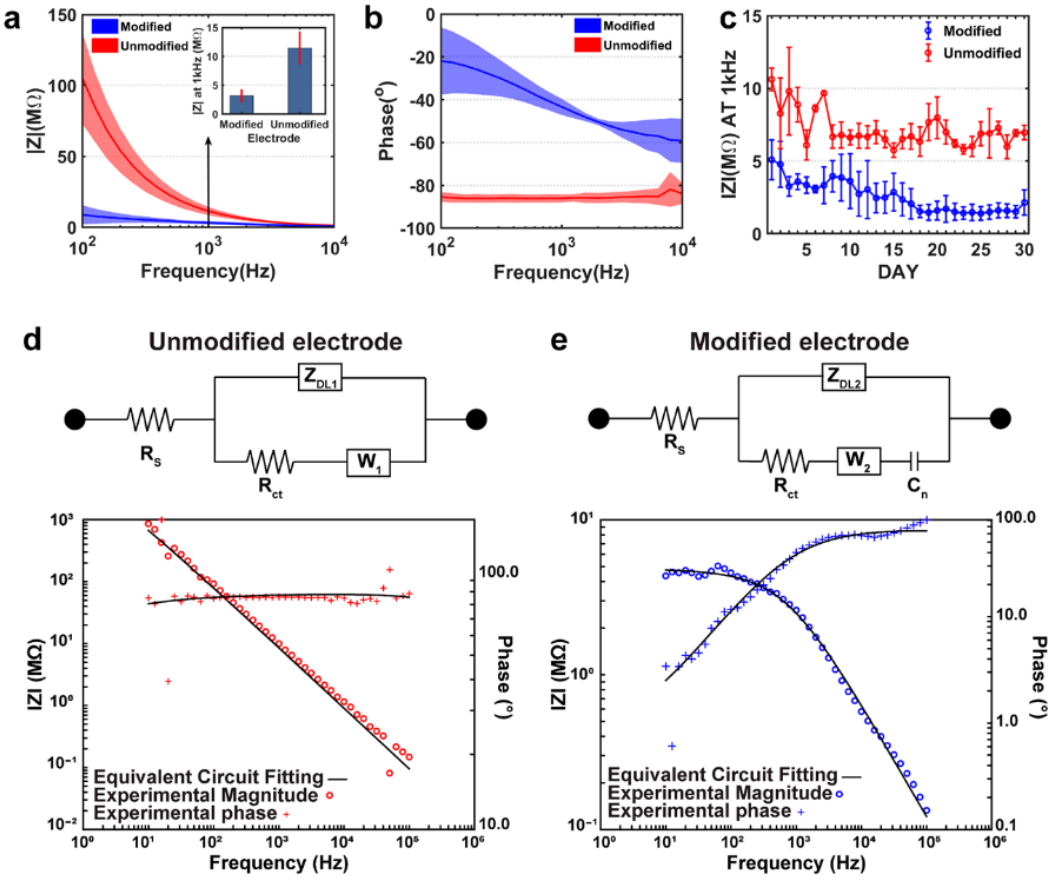

Figure 3.5 EIS measurements and the equivalent circuit model fitting of the electrode before and after surface modification. (a) The Bode magnitude impedance plot of the CNF-CPE electrode showing the lower impedance characteristics of the electrode after surface modification. (b) The Bode phase impedance plot of the CNF-CPE electrodes indicating the less capacitive behavior of the electrode with the interrogation of nano-optoelectrodes. (c) The CNF-CPE electrode with and without surface modification was soaked in 1x PBS for 30 days, and the impedance was recorded daily. Moreover, we can observe that the impedance of the surface-modified electrode is relatively stable, with a slight decrease in the magnitude of the impedance at 1 kHz, while the unmodified electrode exhibits similar behaviors. (d) The equivalent circuit model (modified Randles circuit) of the unmodified electrode and the representative EIS impedance spectra for experimental data (red) and equivalent circuit fitting (black) used for curve fitting. It is composed of electrolyte resistance (Rs) in series with a parallel combination of the double-layer capacitor (ZDL), Warburg impedance (W1), and charge transfer resistance (Rct1). (e) The equivalent circuit model of the modified electrode and the representative EIS impedance spectra for experimental data (blue) and equivalent circuit fitting (black) used for curve fitting. A pseudo-capacitor (Cn) was introduced to the circuit and in series of the Warburg impedance to represent the redox energy stored at the surfaces of nano-optoelectrodes.

To further understand how the deposited nano-optoelectrodes improve the electrical performance of the CNF-CPE electrodes, we first curve-fitted the experimental EIS data of unmodified electrodes to a modified Randles circuit[18, 33-35], as shown in **Figure 3.5d**. This model contains a solution resistance, R_s, in series with a parallel combination of a constant phase element representing double layer capacitor, Z_{DL1}, a charge transfer resistance, R_{ct1}, simulating Faradic reactions, and a Warburg impedance presenting the diffusion process. The constant phase element (a capacitor with non-ideal capacitor behavior) is defined as:

$$Z = 1/Y_0(jw)^n \quad (2)$$

where Y_0 is the capacitance of the constant phase element, and n is the phase factor (for an ideal capacitor, n = 1).[18, 36] The parameters for this equivalent circuit model are listed in Table 1 with mean values and standard deviations. For the surface-modified electrodes, we introduced a pseudo-capacitor to be in series with the Warburg element to represent the redox energy stored at the nanostructured surfaces of nano-optoelectrodes arrays[37, 38] while all the other elements remain unchanged, and the curve-fitted results are shown in **Figure 3.5e**. Then we applied the fitted solution resistance result from **Table 3.1** to the experimental EIS data of surface-modified electrodes, and the curve-fitted parameters are shown in **Table 3.2**.

unmodified					
	R_s (KΩ)	Y_{01} ($S*S^{A1}$)	A1	W1 ($S*S^{1/2}$)	R_{ct1} (MΩ)
mean	4.356	21.65×10^{-12}	0.956	34.71×10^{-12}	2.14
SD	0.051	1.34×10^{-12}	0.024	4.11×10^{-12}	0.34

Table 3.1 Means and standard deviations (SD) of parameters in the equivalent circuit model with the unmodified probe.

By comparing the parameters from these two tables, we can conclude that the deposited nano-optoelectrodes have increased the double-layer capacitance and promoted the charge transfer

reaction between the electrode surface and the electrolyte, resulting in the decrease of the impedance value. Also, the decrease in the phase factor further validates the increase of the surface roughness[39, 40], and the less capacitive behavior of the electrode after nano-optoelectrodes deposition.

modified					
	Y_{02} ($S*S^{A2}$)	A2	W_1 ($S*S^{1/2}$)	R_{ct1} (MΩ)	C_n (μF)
mean	383 x 10^{-12}	0.749	2.3 x 10^{-6}	4.91	1.47
SD	18.3 x 10^{-12}	0.04	0.58 x 10^{-6}	0.27	0.44

Table 3.2 Means and standard deviations (SD) of parameters in the equivalent circuit model with the surface-modified probe.

3.2.4 In vivo electrophysiology

To evaluate the recording capability of the surface-modified electrodes, we implanted the fibers into to hippocampus region of five wild-type mice for *in vivo* electrophysiology study. **Figure 3.6a** shows a photograph of a healthy mouse with a small probe implanted for 24 days. 24 days after the implantation, we started recording, and a representative trace of the raw recordings from the hippocampus region of the mice is shown in **Figure 3.6b**. The recorded signal was bandpass-filtered from 0.3 to 300 Hz and 300 to 5000 Hz to isolate the Local Field Potential (LFP) and single-unit activities, respectively. From the bandpass-filtered spiking activities, two representative spike clusters were distinctively isolated amongst many other spike clusters via principal component analysis (PCA) and K-means clustering. The two clusters can be observed in the recording data, in the action potentials, and in the PCA with the corresponding matching colors, which demonstrates our surface-modified electrodes' recording capability with a single-unit resolution (**Figure 3.6c**). We also calculated the two standard metrics, L-ratio and isolation distance, to evaluate the separations of spike clusters. From the minute-long recording, the L-ratio and the isolation distance (ID) of the two clusters were 0.024 and 18.28, respectively.

We repeated recordings of neural activities 28 weeks after implantation in five animals, as shown in **Figure 3.6d-e**. A representative 2.5 seconds electrophysiology recording is shown in **Figure 3.6d.** The top trace shows the unfiltered signal, the middle trace represents LFP recording, and the bottom one shows the spiking activities. Two isolated clusters were sorted from the recorded signal via the PCA analysis (Figure 4e). The L-ratio and the ID of two isolated clusters were 0.07 and 40.97, respectively. Clusters with L-ratio lower than 0.2 and ID larger than 20 are considered well-separated single neurons. Thus, the surface-modified electrodes presented reliable and stable recording performance over an extended period of chronic implantation.

To compare the recording performance of the CNF-CPE electrode before and after surface modification with nano-optoelectrodes, we implanted surface modified and unmodified polymer electrodes to the hippocampal formation of three wild-type mice and conducted power spectral analysis on the LFP recordings obtained from these electrodes. **Figure 3.6f** shows representative 2-second traces of LFP recording results from the CNF-CPE electrode with and without surface modification. One can observe that the peak-to-peak amplitude of the LFP trace acquired from the modified electrode was, on average, higher in magnitude than that acquired from the unmodified electrode. The frequency ranges content of the signal we investigated are, namely, Delta (0.5 - 3 Hz), Theta (4 - 7Hz), Alpha (8 - 13 Hz), and Beta (14 - 40 Hz) waves. As expected, in the spectrograms of a 140-second-long LFP trace from both electrodes, we observed relatively higher powers in each frequency bins with the surface-modified electrodes (**Figure 3.6g**). The resulting plot of the multitaper power spectral density estimate (**Figure 3.7**) also confirmed a systematically higher power density with nano-optoelectrodes modification.

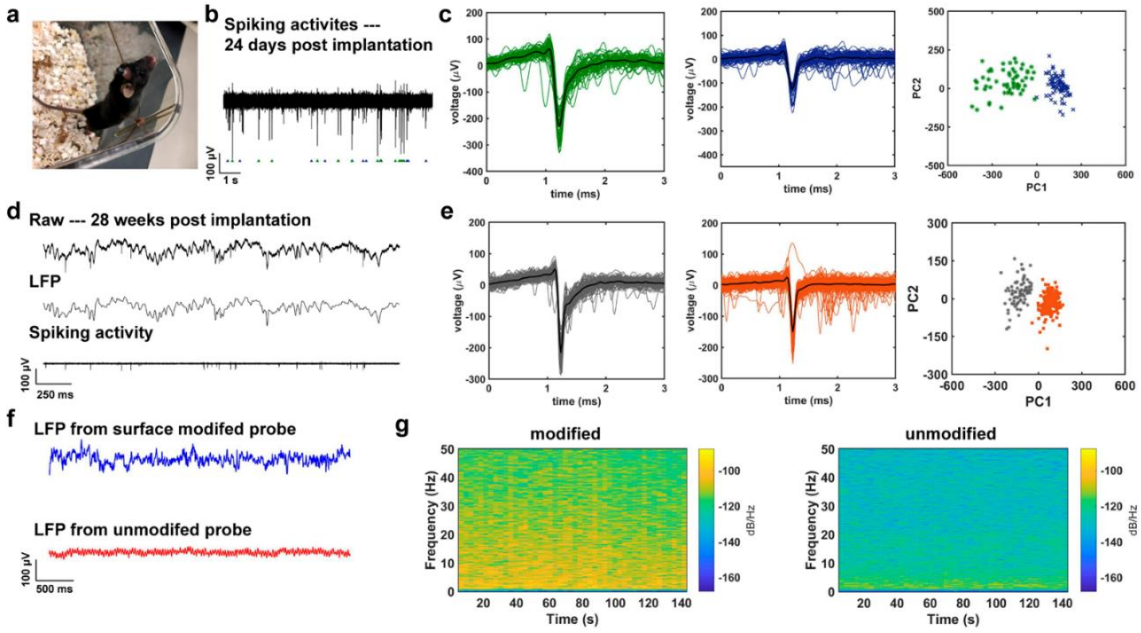

Figure 3.6 Electrophysiology recording from the surface-modified CNF-CPE electrodes, and its comparison with that from the unmodified electrodes. (a) A photograph of a mouse with the small CNF-CPE electrode implanted for 24 days. (b) A representative trace of spiking activities acquired from the surface-modified electrode 24 days post-implantation. (c) Two distinct clusters were isolated from the recorded signal via PCA. (d) Representative recorded electrophysiological signal following 28 weeks of implantation. The top trace shows the unfiltered signal, the middle trace shows bandpass-filtered (0.3 − 300 Hz) LFP, and the bottom trace represents the bandpass-filtered (0.5 − 5 kHz) spiking activity. (e) Two clustered units were sorted from the recording result and the corresponding PCA, indicating the quality of these two clusters. (f) A 2.5 s of LFPs was recorded from CNF-CPE electrodes with and without nano-optoelectrodes on day 0, showing a better recording performance with the surface-modified electrode. (g) The spectrograms of a 140-second-long LFP trace from both surface modified and unmodified electrodes, we observed relatively higher powers in each frequency bins from the CNF-CPE electrode with nano-optoelectrodes.

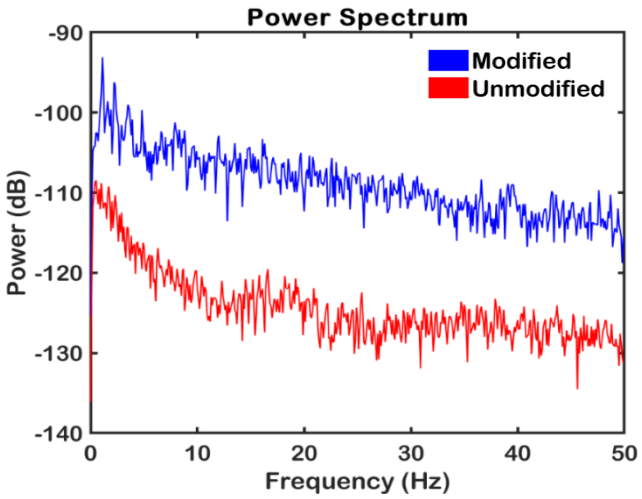

Figure 3.7 Power spectral density of the recording from surface modified and unmodified electrodes.

3.2.5 Biocompatibility of the surface modified electrode

The reactive tissue response to our surface-modified neural probe was assessed using immunohistochemical analysis of surrounding brain tissue from mice implanted for two-weeks with either a surface modified probe or a conventional stainless steel probe. The presence of glial fibrillary acidic protein (GFAP) was used to assess astrocyte reactivity to the probe, ionized calcium-binding adaptor molecule 1 (Iba1) was used as a marker of microglial response, and lastly, the neuron-specific protein NeuN was used to analyze neuronal density. Representative images from the contralateral side of an implanted brain (control), surface modified probe, and stainless steel probe are presented in **Figure 3.8**. Neuronal density, microglia density, and astrocyte reactivity were compared between all groups, and no significant difference was observed, **Figure 3.8e-g**.

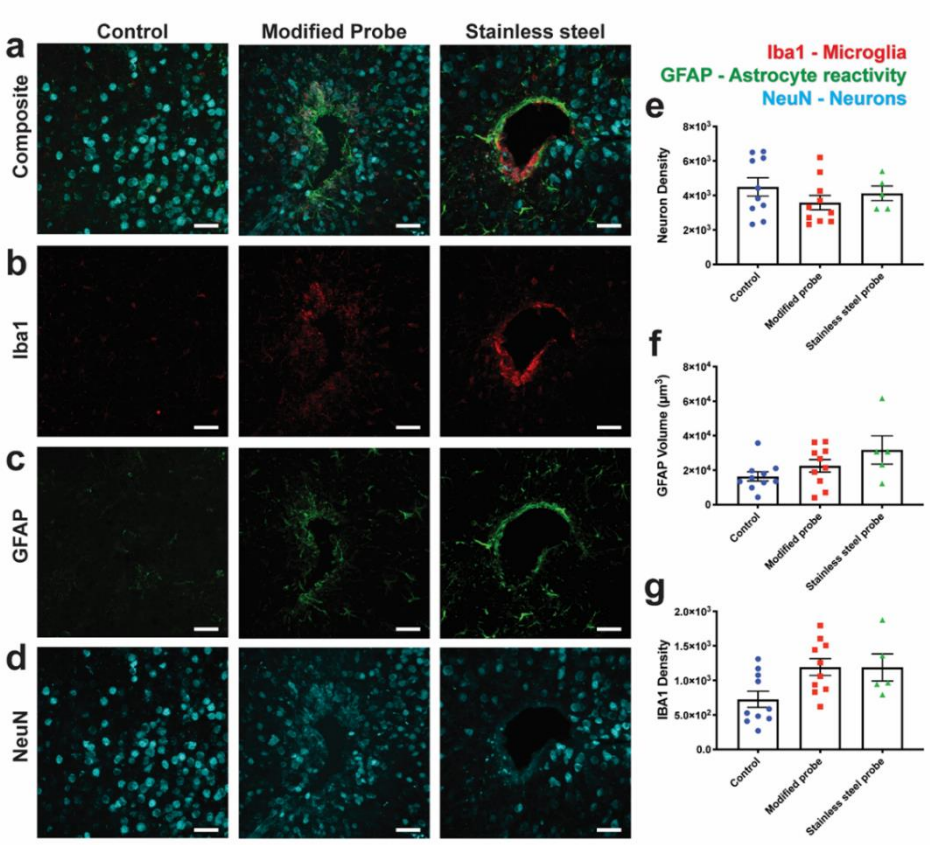

Figure 3.8 Immunohistological comparison of tissue reaction to chronically implanted surface modified probes (center) and conventional stainless steel probes (right) after two-week implantation. Control images (left) were acquired from contralateral side of implanted brain. (a−d) Z-projections created from confocal optical sections. Neurons labeled with NeuN (cyan), astrocytes labeled with GFAP (green), and microglia labeled with Iba1 (red). (d,e) Neuron density, calculated by counting NeuN labeled neurons, was not significantly different between the groups. (c,f) Astrocyte reactivity, measured as the volume of GFAP-positive cells, was not significantly different between groups. (b,g) The density of Iba1-positive cells was also not significantly different between groups. Significance was determined by one-way ANOVA with Tukey's multiple comparison test. Error bars on bar graphs reflect the standard error of the mean. (Scale bar: 40 μm)

3.3 Conclusion

We have developed a scalable method for fabricating nano-optoelectrode arrays on tips of multifunctional fibers by using free-standing nanohole array deposition masks. The integration of nanolaminated nanoantenna arrays allows us to conduct RI optical sensing and surface-enhanced Raman spectroscopy on the fiber tip. In the meantime, the conductive metal nanostructures can

enhance the electrical recording performance of the polymer-based microelectrodes demonstrating a larger power density of local field potential (LFP) compared with unmodified probes. These nano-optoelectrodes integrated probes were able to provide continuous electrophysiology measurements up to 28 weeks post-implantation, indicating good biocompatibility of these probes, consistent with our immunohistochemistry analysis. All these results indicate that we have developed a miniaturized multifunctional neural probe platform that can integrate optical nanoplasmonic biosensors and neural recording microelectrodes on the tip of a flexible and biocompatible polymer fiber. This work will pave the way toward new multimodal detection approaches for a deeper understanding of brain function in both the electrophysiological and biomolecular aspects.

3.4 Materials and methods

Thermal Fiber Drawing Process A preform was prepared to draw the multifunctional fiber with silica fiber inside. First, polycarbonate (PC) films (Laminated Plastics) were wrapped around a PTFE rod (U.S. Plastic Corp.) and consolidated to a PC tube with thick walls. Then four grooves were machined on the PC tube, and two of the grooves were inserted with commercially available conducting polyethylene (CPE, Hillas Packaging) as the electrodes while the other two remained hollow as the microfluidic channels. After the insertion of electrodes, additional PC films were wrapped around the structure and consolidated to a macroscopic template. Before the thermal drawing process, the silica fiber (AFH105/125/145T, Fiberguide) was inserted into the hole in the preform center and was fixed to the preform bottom, which enabled the flow of silica fiber as being pulled during the polymer thermal drawing process. Also, multifunctional fiber made of PVDF (polyvinylidene difluoride) was fabricated using the same method with an additional PC layer as a sacrificial layer to support a stable drawing.

Bundle Process In order to maximize the usage of the Au nanohole arrays mask, the outer sacrificial PC layer was etched away by immersion in dichloromethane for 2-4 min for each fiber with reasonable impedance data. Then fibers were inserted into a piece of nonporous alumina ceramic tube (Mcmaster-Carr) and fixed by Phenyl salicylate on both ends. After the fixation, a similar size hole was created in the center of a PC rod, and the ceramic tube was fixed inside this hole using the same method described above. In order to obtain a flat surface for the future deposition process, the fiber bundle was polished by optical polishing papers (30, 12, 5, 1, 0.5μm, Fiber Optic Center), resulting in sub-micrometer roughness.

Nanolaminated plasmonic nanoantenna deposition Before the deposition, the polished fiber bundle by oxygen plasma. The Au nanohole-array mask was pre-fabricated on a Si substrate with a 10-nm thick Cr sacrificial under the Au layer. Cr etchant (CHROMIUM ETCHANT 1020, Transene, USA) was used to lift-off this Au nanohole-array mask[21]. The thickness of the nanohole-array mask is about 150 nm, with the nanohole-array diameter of ~130 nm and the periodicity of 400 nm. After etching the Cr layer, we introduce deionized water between the Au nanohole array and the silicon substrate to float it up. Then scooping the mask onto oxygen plasma-treated glass substrate and transfer onto the fiber bundle surface with drying overnight at room temperature. Before depositing the alternating Au-Ag layers, a thin layer of Ti of 1 nm was deposited onto the bundle substrate through the nanohole array as an adhesion layer, then alternating layers of Au and Ag were deposited with layer thicknesses of 25, 6, 25, 8, 25 nm from bottom to top for the CNF fiber, while the thickness of 25, 6, 25, 8, 25, 10, 25 nm for the multifunctional fiber. Finally, the nanohole-array mask was peeled off by scotch tape, leaving the periodic nanoantenna arrays on the bundle surface. After the deposition, the ceramic tube was removed from the PC rod by apply heat through the hot gun, and the same process was repeated to separate fibers from the ceramic

tube. Followed by the separation, fiber was cleaned by dichloromethane to remove phenyl salicylate residue and rinsed by isopropyl alcohol (MilliporeSigma) for further cleaning.

Raman measurement BZT (Sigma-Aldrich, USA) was used as the probe molecules to evaluate the SERS performance of the modified fiber. The fiber tip was incubated in 1×10^{-3} M of BZT ethanolic solution for 24h to form a self-assembled monolayer. A confocal Raman microscope (Alpha 300 RSA+, WITec, Germany) equipped with a 785 nm diode laser (Toptica Photonics, Germany) was used for SERS measurement. BZT signals were collected via 20× objective (NA = 0.4) with 3 mW and 0.1 s integration time. Before the measurement, the instrumental calibration was verified using a silicon wafer by the silicon peak at 520 cm^{-1}. The backscattered photons were detected by a spectrometer (UHTS300, WITec, Germany) equipped with a CCD camera (DU401A, Oxford Instruments, UK). Cosmic ray removal and baseline correction were conducted by an instrument embedded software (Project v4.1, WITec, Germany) after the signal acquisition.

Refractive index measurement A halogen light source (DH 2000, Ocean Optics, USA) was utilized to illuminate the nano-optoelectrodes modified fiber tip via 20× objective (NA = 0.4) using the microscope configuration of an existing microscope (Alpha300 RSA+, WITec, Germany) schematically shown in **Figure 3.9**. The transmitted light under normal excitation was collected at the end of the fiber sensor with a fiber-coupled spectrometer (Flame, Ocean Optics, USA). For examining the sensitivity of the nano-optoelectrodes deposited onto the fiber tip to changes in refractive indices, optical transmission spectra were measured as the sensor tip was immersed in different liquid solutions such as water (n = 1.33), ethanol (n = 1.36), isopropyl alcohol (n = 1.38), butanol (n = 1.4). The transmission spectra are normalized by reference spectra measured using unmodified fiber and noise. The normalized transmission spectra were calculated by,

$$I_{normalized} = (I_{sample} - I_{noise})/(I_{reference} - I_{noise}) \quad (3)$$

where I_{sample}, I_{noise} and $I_{reference}$ are the transmission spectra of modified fiber, noise and transmission spectra of unmodified fiber, respectively.

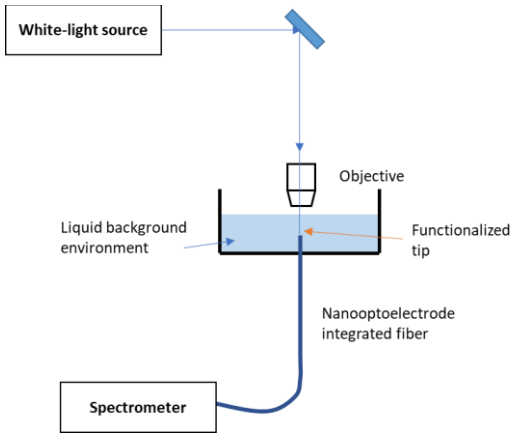

Figure 3.9 Schematic illustration of the extinction measurement.

Electrochemical Impedance Spectrum 2 cm long fiber sections of surface-modified and unmodified with similar cross-sectional size (25.7 μm × 16.6 μm) were prepared and connected with copper wire via silver paint. A potentiostat (Interface 1000E, Gamry Instruments) was utilized to obtain the impedance measurement results with 1x phosphate-buffered saline (PBS, Thermo Fisher) as the electrolyte. To evaluate the change in impedance results before and after surface modification of the polymer electrode, we performed a three-electrode experiment with polymer fiber, Ag/AgCl electrode (Cole-Pamer), and a Pt wire (Basi), which serve as working electrode, reference electrode, and counter electrode respectively. An AC voltage of 10 mV with frequency ranging from 10 Hz to 100 kHz was applied, and the impedance measurement results were recorded accordingly. In order to discover the impact of silver oxidation on electrode electrical characteristics, the polymer fiber tip was soaked in 1X PBS, and two-electrode EIS experiments were conducted daily for two weeks, which mimic the two-electrode recording environment in

mouse brain. The exciting AC voltage remained the same, while the frequency range changed to 100 Hz to 10 kHz.

Neural Probes Assembly Conductive silver paint was applied on the fiber tip to connect the copper wire, which was soldered to headpins (Sullins Connector Solutions) while the ground wire was a soldered stainless steel wire (GoodFellow). Then 5-minute epoxy (Devcon) was used to fix these wires as well as insulate the exposed electrical conducting parts.

Surgical Procedures All animal procedures were approved by the Virginia Tech Institutional Animal Care and Use Committee and Institutional Biosafety Committee and carried out in accordance with the National Institutes of Health Guide for the Care and Use of Laboratory Animals. Aged 7-9 weeks male C57BL/6J mice (Jackson Laboratory) were set up on a stereotaxic apparatus (David Kopf Instruments) and anesthetized by 1-3.5% isoflurane during the procedure via a nose cone. Pre-operatively, buprenorphine (0.05-0.1 mg/kg) with a dose of carprofen (5mg/kg) and Baytril (5mg/kg) was administrated subcutaneously to prevent post-surgical pain and infections. A small incision was made behind the eyes along the midline on the bare scalp to expose the skull, and the exposed skull was scraped with a sterile tool (Fine Science Tool) to facilitate future adhesion of Metabond (C & B METABOND). A small craniotomy was made with a dental drill through which the fiber electrode was lowered using a micropositioner and into the brain according to the brain atlas (coordinates relative to bregma: -2 mm anteroposterior, -1.5 mm mediolateral and -1.9 mm dorsoventral). Then the stainless steel ground wire was soldered to a miniature screw (J.I. MORRIS), which was affixed to the skull by Metabond along with the exposed skull area. To further stabilize the implantation, dental cement was applied, and the implant was fully supported by the skull. Animals were provided with a heating pad to maintain their body temperature during all procedures.

In Vivo Electrophysiology and Data Analysis After animals recovered from the surgery, headpins were connected to a 32 Channel Neurophysiology System (Tucker-Davis Technologies) to perform electrophysiology recordings. The electrophysiological activities in the hippocampus were sampled with the modified electrode at ~50 kHz. The sampled activities were bandpass-filtered from 0.3 to 300 Hz and 300 to 5000 Hz to access the LFP and single-unit activities. We wrote custom scripts in MATLAB (Mathworks) to detect action potentials in the single-unit traces and to analyze the power spectral density of the LFP traces. The candidates of action potentials were detected by setting a lower bound and an upper bound voltage threshold. These thresholds were set by visually investigating the waveforms of some action potentials and taking into account of different measurements of the overall signal, such as the standard deviation, noise level, etc. Due to the neurons' inherent refractory period, the deadtime was set to be 1 ms. For spike sorting, we first reduced the dimension of the candidates' voltage recordings via PCA. Then, in the principal component plane, we performed K-means clustering to cluster different numbers of candidates together. To evaluate these clusters, we computed L-ratio and isolation separation in the first 3 principal component space. The spectrograms of the LFP recordings were created with a moving hamming window with a length of 10 seconds and an overlap of 7 seconds. The parameters can be easily manipulated in the custom script to improve the resolution or the blurriness of the spectrograms. We adopted a multitaper power spectral estimate developed by Thomson, which reduces bias in estimation by introducing pairwise orthogonal Slepian tapers to the calculation. In our script, we used 7 independent Slepian tapers with a taper length of 10 seconds to create an estimation over a 50-second-long LFP recording. The interspike interval (ISI) histogram was computed by taking the time intervals in the same cluster and arranging the time

intervals into different bins. Due to the deadtime, the ISI histogram did not contain any counts <1ms.

Immunohistochemistry Animals were implanted with a stainless steel probe or a surface modified probe for 2 weeks and then anesthetized with a ketamine (20mg/mL)/xylazine (2mg/mL) solution and transcardially perfused with phosphate-buffered saline (PBS) (Fisher BP661-10) followed by 4% paraformaldehyde (PFA) (Electron Microscopy Sciences Cat. #15714-S) in PBS. Upon extraction, the brain was kept in 4% PFA overnight at 4º C and then placed into PBS containing 0.02% sodium azide (Sigma S8032). The brain was serially sectioned into 50 µm transverse slices on a Campden Instruments 5100mz vibratome. All slices were blocked for 1hr at room temperature in a blocking solution that contained 10% goat serum (Millipore S26-100ML) and 0.01% Triton X-100 (Sigma T9284) in PBS containing 0.02% sodium azide. After blocking, the slices were incubated with primary antibodies diluted in blocking solution without Triton X-100 overnight at room temperature. Primary antibodies used included chicken anti-GFAP (abcam Cat. #ab4674, 1:1000), mouse anti-NeuN (Millipore Cat. #MAB377, 1:1000), and rabbit anti-Iba1 (Wako Cat. #019-19741, 1:500). Following primary incubation, slices were washed six times with PBS for 10 minutes at room temperature with agitation. Secondary antibodies diluted in blocking solution without Triton X-100 were added at room temperature for 1 hr. Secondary antibodies used included goat anti-chicken Alexa Fluor 488 (Jackson ImmunoResearch Cat. #103-545-155, 1:500) goat anti-mouse Alexa Fluor 647 (Jackson ImmunoResearch Cat. #115-605-062, 1:500) and goat anti-rabbit Alexa Fluor 550 (Jackson ImmunoResearch Cat. #111-165-144, 1:500). Slices were then washed six times with PBS for 10 min at room temperature with agitation. Slices were mounted on glass slides with VECTASHIELD Antifade Mounting Medium with DAPI (Vector Laboratories Cat. #H-1200). Optical sections were acquired using a Nikon A1 laser scanning

microscope using a Plan Apo 20X/N.A.0.75 air objective. Quantification of the volumetric data was performed using NIS-Elements (Nikon Instruments Inc.). Neuron and Microglia density was calculated by counting NeuN, and IBA1 labeled cell bodies, respectively, using spot detection. Volumetric analysis of GFAP Labeled cells was performed by creating 3D reconstructions of the optical sections using the Threshold 3D tool and quantified using 3D volumetric measurement.

3.5 References

1 Shen, Y. *et al.* Plasmonic gold mushroom arrays with refractive index sensing figures of merit approaching the theoretical limit. *Nat Commun* **4**, 2381, doi:10.1038/ncomms3381 (2013).

2 B. Špačková, P. W., M. Bocková and J. Homola. Optical Biosensors Based on Plasmonic Nanostructures: A Review. *Proceedings of the IEEE* **104**, 2380-2408, doi:10.1109/JPROC.2016.2624340 (2016).

3 Brolo, A. G. Plasmonics for future biosensors. *Nat Photonics* **6**, 709–713, doi:10.1038/nphoton.2012.266 (2012).

4 Sun, F. *et al.* Hierarchical zwitterionic modification of a SERS substrate enables real-time drug monitoring in blood plasma. *Nat Commun* **7**, 13437, doi:10.1038/ncomms13437 (2016).

5 Zong, C. *et al.* Surface-Enhanced Raman Spectroscopy for Bioanalysis: Reliability and Challenges. *Chem Rev* **118**, 4946-4980, doi:10.1021/acs.chemrev.7b00668 (2018).

6 Hering, K. *et al.* SERS: a versatile tool in chemical and biochemical diagnostics. *Anal Bioanal Chem* **390**, 113-124, doi:10.1007/s00216-007-1667-3 (2008).

7 Smythe, E. J., Dickey, M. D., Whitesides, G. M. & Capasso, F. A technique to transfer metallic nanoscale patterns to small and non-planar surfaces. *Acs Nano* **3**, 59-65, doi:10.1021/nn800720r (2009).

8 Zhang, S. Y. *et al.* High-Q Polymer Microcavities Integrated on a Multicore Fiber Facet for Vapor Sensing. *Advanced Optical Materials* **7**, doi:10.1002/adom.201900602 (2019).

9 Wang, Q. & Wang, L. Lab-on-fiber: plasmonic nano-arrays for sensing. *Nanoscale* **12**, 7485-7499, doi:10.1039/d0nr00040j (2020).

10 Vaiano, P. *et al.* Lab on Fiber Technology for biological sensing applications. *Laser Photonics Rev* **10**, 922-961, doi:10.1002/lpor.201600111 (2016).

11 Kostovski, G., Stoddart, P. R. & Mitchell, A. The Optical Fiber Tip: An Inherently Light-Coupled Microscopic Platform for Micro- and Nanotechnologies. *Advanced Materials* **26**, 3798-3820, doi:10.1002/adma.201304605 (2014).

12 Ricciardi, A. *et al.* Lab-on-fiber technology: a new vision for chemical and biological sensing. *Analyst* **140**, 8068-8079, doi:10.1039/c5an01241d (2015).

13 Liu, Y. *et al.* Simple and Low-Cost Plasmonic Fiber-Optic Probe as SERS and Biosensing Platform. *Advanced Optical Materials* **7**, 1900337 (2019).

14 Lipomi, D. J. *et al.* Patterning the Tips of Optical Fibers with Metallic Nanostructures Using Nanoskiving. *Nano Lett* **11**, 632-636, doi:10.1021/nl103730g (2011).

15 Consales, M. *et al.* Lab-on-fiber technology: toward multifunctional optical nanoprobes. *Acs Nano* **6**, 3163-3170, doi:10.1021/nn204953e (2012).

16 Ricciardi, A. *et al.* Versatile Optical Fiber Nanoprobes: From Plasmonic Biosensors to Polarization-Sensitive Devices. *ACS Photonics* **1**, 69-78, doi:10.1021/ph400075r (2014).

17 Pisco, M. *et al.* Miniaturized Sensing Probes Based on Metallic Dielectric Crystals Self-Assembled on Optical Fiber Tips. *ACS Photonics* **1**, 917-927, doi:10.1021/ph500126v (2014).

18 Nimbalkar, S. *et al.* Ultra-Capacitive Carbon Neural Probe Allows Simultaneous Long-Term Electrical Stimulations and High-Resolution Neurotransmitter Detection. *Sci Rep* **8**, 6958, doi:10.1038/s41598-018-25198-x (2018).

19 Jun, J. J. *et al.* Fully integrated silicon probes for high-density recording of neural activity. *Nature* **551**, 232-236, doi:10.1038/nature24636 (2017).
20 Seidl, K. *et al.* CMOS-Based High-Density Silicon Microprobe Arrays for Electronic Depth Control in Intracortical Neural Recording. *J Microelectromech S* **20**, 1439-1448, doi:10.1109/Jmems.2011.2167661 (2011).
21 Seidl, K. *et al.* In-plane silicon probes for simultaneous neural recording and drug delivery. *J Micromech Microeng* **20**, doi:10.1088/0960-1317/20/10/105006 (2010).
22 Wu, F. *et al.* Monolithically Integrated muLEDs on Silicon Neural Probes for High-Resolution Optogenetic Studies in Behaving Animals. *Neuron* **88**, 1136-1148, doi:10.1016/j.neuron.2015.10.032 (2015).
23 Park, S. *et al.* One-step optogenetics with multifunctional flexible polymer fibers. *Nature Neuroscience* **20**, 612-+, doi:10.1038/nn.4510 (2017).
24 Guo, Y. Y. *et al.* Polymer Composite with Carbon Nanofibers Aligned during Thermal Drawing as a Microelectrode for Chronic Neural Interfaces. *Acs Nano* **11**, 6574-6585, doi:10.1021/acsnano.6b07550 (2017).
25 Canales, A. *et al.* Multifunctional fibers for simultaneous optical, electrical and chemical interrogation of neural circuits in vivo. *Nat Biotechnol* **33**, 277-+, doi:10.1038/nbt.3093 (2015).
26 Yu, L. *et al.* Flexible Multi-Material Fibers for Distributed Pressure and Temperature Sensing. *Advanced Functional Materials* **30**, 1908915, doi:https://doi.org/10.1002/adfm.201908915 (2020).
27 Haring, A. P. *et al.* 3D bioprinting using hollow multifunctional fiber impedimetric sensors. *Biofabrication* (2020).
28 Ali Safiabadi Tali, S. & Zhou, W. in *Frontiers in Optics / Laser Science.* JTu2A.58 (Optical Society of America).
29 Song, J. *et al.* Partial Leidenfrost Evaporation-Assisted Ultrasensitive Surface-Enhanced Raman Spectroscopy in a Janus Water Droplet on Hierarchical Plasmonic Micro-/Nanostructures. *Acs Nano* **14**, 9521-9531, doi:10.1021/acsnano.0c04239 (2020).
30 Song, J. & Zhou, W. Multiresonant Composite Optical Nanoantennas by Out-of-plane Plasmonic Engineering. *Nano Lett* **18**, 4409-4416, doi:10.1021/acs.nanolett.8b01467 (2018).
31 Junyeob Song, W. N., Wei Zhou. Scalable High-Performance Nanolaminated SERS Substrates Based on Multistack Vertically Oriented Plasmonic Nanogaps. *Advanced Materials Technologies* **4**, doi:10.1002/admt.201800689 (2019).
32 Ludwig, K. A., Uram, J. D., Yang, J. Y., Martin, D. C. & Kipke, D. R. Chronic neural recordings using silicon microelectrode arrays electrochemically deposited with a poly(3,4-ethylenedioxythiophene) (PEDOT) film. *J Neural Eng* **3**, 59-70, doi:10.1088/1741-2560/3/1/007 (2006).
33 Cutrone, A. & Micera, S. Implantable Neural Interfaces and Wearable Tactile Systems for Bidirectional Neuroprosthetics Systems. *Adv Healthc Mater*, doi:10.1002/adhm.201801345 (2019).
34 Shin, Y. M. *et al.* Microprobe electrode array with individual interconnects through substrate using silicon through-glass via. *Sensor Actuat B-Chem* **290**, 336-346, doi:10.1016/j.snb.2019.03.143 (2019).

35 Park, H., Takmakov, P. & Lee, H. Electrochemical Evaluations of Fractal Microelectrodes for Energy Efficient Neurostimulation. *Sci Rep-Uk* **8**, doi:10.1038/s41598-018-22545-w (2018).
36 Abouzari, M. R. S., Berkemeier, F., Schmitz, G. & Wilmer, D. On the physical interpretation of constant phase elements. *Solid State Ionics* **180**, 922-927, doi:10.1016/j.ssi.2009.04.002 (2009).
37 Merrill, D. R., Bikson, M. & Jefferys, J. G. R. Electrical stimulation of excitable tissue: design of efficacious and safe protocols. *J Neurosci Meth* **141**, 171-198, doi:10.1016/j.jneumeth.2004.10.020 (2005).
38 Lu, Y. C. *et al.* Ultralow Impedance Graphene Microelectrodes with High Optical Transparency for Simultaneous Deep Two-Photon Imaging in Transgenic Mice. *Advanced Functional Materials* **28**, doi:10.1002/adfm.201800002 (2018).
39 Alexander, C. L., Tribollet, B. & Orazem, M. E. Contribution of Surface Distributions to Constant-Phase-Element (CPE) Behavior: 1. Influence of Roughness. *Electrochim Acta* **173**, 416-424, doi:10.1016/j.electacta.2015.05.010 (2015).
40 Mulder, W. H., Sluyters, J. H., Pajkossy, T. & Nyikos, L. Tafel Current at Fractal Electrodes - Connection with Admittance Spectra. *J Electroanal Chem* **285**, 103-115, doi:Doi 10.1016/0022-0728(90)87113-X (1990).

Chapter 4
3D Bioprinting using hollow multifunctional fiber impedimetric sensors

4.1 Introduction

The increasing demands for products capable of repairing injuries and treating diseases have driven the growth of the regenerative medicine industry.[1-6] While various biofabrication processes have been examined for tissue engineering, demands for product prototyping and personalization have driven the creation of computer-aided biofabrication processes, such as 3D bioprinting processes. 3D bioprinting of cell-laden tissue constructs involves a number of pre-processing operations, including cell differentiation and expansion processes,[7,8] cell separation processes,[8,9] and bioink preparation steps. Thus, while there are various process parameters that are important toward the fabrication of repeatable bioprinted tissues, such as bioink rheological properties, there is a need for real-time in-line bioink compositional analysis, including concentration, cell type, and cell viability, for scalable and quality-controlled of 3D bioprinted constructs.

3D bioprinting processes have various process parameters, each of which exhibit a unique measurement strategy and challenge. One particularly challenging aspect from a process monitoring approach is the use of animal cells, often human cells, as a processed material, which have been referred to as "living materials" from a processing perspective. While sensors are emerging for compositional analysis in cell expansion bioreactors,[10] there remains a need for sensing platforms capable of continuous in-line monitoring of bioink composition and cell quality measures, such as viability and state of differentiation, during bioprinting. For example, in addition to potential variability in cell expansion, differentiation outcome, and bioink preparation

steps, processing defects such as nozzle clogging can also lead to inconsistency among 3D bioprinted tissue constructs.

Impedimetric-based sensing platforms has emerged as an attractive non-destructive testing approach for monitoring cell health, proliferation, and activity in both suspensions and adherent cultures.[11] For example, Nordberg *et al* demonstrated an impedance-based cell assay that monitored the impedance magnitude at 40 kHz in human adipose stem cell (hASC) cultures from young, middle aged, and elderly donors during proliferation and osteogenic differentiation.[12] In that study, sensor response enabled prediction of osteogenic potential in hASC populations, a result which has implications in quality-controlled biomanufacturing of stem cell-based therapies.[12] In another example, Sharma *et al* used impedance spectroscopy to investigate the viability of NS0 murine myeloma cells, an important cell line for production of therapeutic proteins, and found that impedance response enabled a more rapid detection of cell death than a Trypan blue as well as potential for continuous viability monitoring.[13] Narayanan *et al* used dielectric impedance spectroscopy for monitoring the quality of 3D bioprinted constructs.[14] This work showed that monitoring of permittivity change, Cole-Cole slope factor, and critical polarization frequency correlated with cell viability and proliferation and were significantly affected by printing parameters such as processing time and temperature.[14] Thus, an impedimetric sensing approach that could be integrated with the bioink deposition tool (e.g. nozzle) of the 3D bioprinting process may be particularly useful for in-line real-time bioink compositional and quality analysis throughout the material deposition process.

Multifunctional fibers with hollow channels have emerged as attractive platforms for chronic neural monitoring applications given their integrated sensing and microfluidic-based drug delivery capabilities.[15,16] Here, we present a fiber-based impedimetric sensor for monitoring of

bioink composition and quality during continuous microextrusion. Extrusion through electrode-functionalized hollow fibers enabled continuous monitoring of cell-laden solution or bioink impedance magnitude |Z| and phase angle (ϕ) of the extrudate. Studies using fibroblasts, neuronal cells, and stem cells showed that impedimetric sensing enabled detection of cell type, state of differentiation, and viability. This report provides an advance in sensor-based monitoring of 3D bioprinting processes based on bioink compositional and quality analysis using hollow multifunctional fiber technology. Overall, hollow multifunctional fibers provide an attractive platform for controlled delivery and fabrication of cell therapies.

4.2 Results and discussion

4.2.1 Principle of in-line bioink compositional analysis for 3D bioprinting processes

Impedimetric sensing is a useful characterization technique for enabling in-line monitoring of cell-laden bioink composition and quality, given it can be acquired non-invasively via boundary electrodes and can be performed with high-sampling rates. As shown in **Figure 4.1a**, the flow of alternating current through cell-laden materials, such as tissues, is dependent on the frequency of the applied electrical potential.[18] At low frequency, the current is dominated by charge transfer around cells through the extracellular matrix (ECM) or extracellular fluid (ECF), while current also arises from charge transfer through cells at high frequency.[18] To date, impedimetric characterization of cell-laden materials has enabled the characterization of cell shape, size, density, and integrity.[11,18] As shown in **Figure 4.1b**, hollow multifunctional fibers enable impedimetric characterization of extruded materials, such as a cell-laden bioink, using the two copper fiber electrodes. Thus, multifunctional fibers potentially enable real-time monitoring of the bioink impedance magnitude ($|Z|$) and phase angle (ϕ) frequency response during extrusion. As shown in **Figure 4.1c**, hollow multifunctional fibers facilitate in-line sensing of 3D bioprinting processes,

particularly real-time bioink compositional analysis. Multifunctional fibers potentially provide an attractive sensing platform for understanding the effect of bioink composition and process parameters, such as extrusion flow rate, on the properties and quality measures of 3D bioprinted tissue constructs.

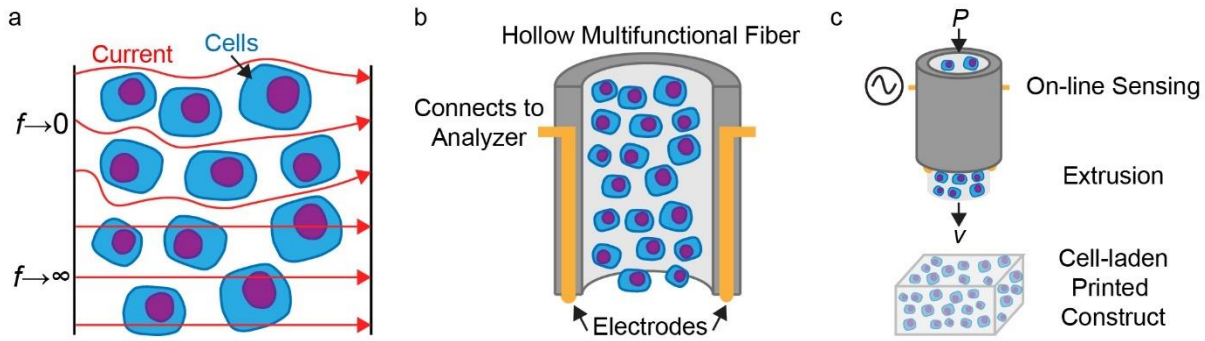

Figure 4.1 Sensing principle of the bioink during 3D printing process. a) Schematic representation of impedimetric monitoring of cell-laden materials using a two-electrode format showing the paths of current when driven by low- (f→0) and high-frequency (f→∞) applied potentials. b) Schematic showing the impedimetric sensing principle for bioink compositional analysis implemented in hollow multifunctional fibers. c) Schematic describing the concept of sensor-based in-line bioink compositional analysis of 3D bioprinting processes using multifunctional fibers.

4.2.2 Fabrication of hollow multifunctional fibers for extrusion of cell-laden bioinks

Given the majority of microextrusion 3D bioprinting is done using extrusion nozzles of diameter ranging from 100 – 500 μm,[19-21] we first examined the ability to tune the fiber channel diameter by variation of the fiber design or thermal drawing process parameters. As shown in **Figure 4.2a**, we produced the electrode-functionalized hollow fibers of conserved cross-sectional geometry and composition by the thermal drawing process. Before the thermal drawing process, we first created a macroscopic template, a preform, by wrapping PC films around a mandrel (Teflon rod), consolidating them, and machining the structure. The final preform consisted of one center hollow channel and two side hollow channels. Two copper wires were inserted into the

two side channels respectively and they were confined within their initial grooves and remained adjacent to the center hollow channel using a convergence fiber drawing method as previously reported. We varied the diameter of the center hollow channel by utilizing Teflon rods with different sizes. For example, the diameters of the Teflon rod used in this study were 6.35, 9.525, and 12.7 mm, which produced the corresponding hollow channel diameters in as-drawn fibers of 181, 272, and 362 μm, respectively as shown in **Figure 4.2b-d**. In addition to modifying the fiber channel diameter through the dimensions of the Teflon rod used in the preform fabrication process, we further tuned the channel diameter by adjusting the draw down ratio defined as the ratio of initial to final diameter. Fibers with a range of commonly used inner diameters of 100, 200, 300, 400, and 500 μm were fabricated by adjusting of the draw down ratio used for the three aforementioned preform geometries. Thus, the thermal drawing process enables the fabrication of hollow multifunctional fibers with a range of channel dimensions that are commonly employed for 3D bioprinting processes. As shown in **Figure 4.2e**, the volumetric flow rate (Q) increased nonlinearly with respect to increasing fiber channel diameter at a constant pressure, an expected result considering the Hagen-Poiseuille equation for shear-thinning power-law fluid (*e.g.*, alginate solutions[22]):[23]

$$Q = \frac{\pi R^3}{\frac{1}{n}+3}\left(\frac{\Delta P R}{2LK}\right)^{1/n} \quad (1)$$

where n is the flow behavior index, K is the flow consistency index, R is the nozzle radius, ΔP is the pressure drop, and L is the length of the nozzle.[24] The frictional head loss (h_f), an important parameter relating to shear stress-induced cell death and injury in 3D bioprinting processes, was calculated using Bernoulli's equation assuming negligible contributions of potential energy effects as:[23]

$$h_f = \frac{P_{appl} - P_{atm}}{\rho g} - \frac{v_{out}^2}{2g} \quad (2)$$

where P_{appl} is the applied pressure (here, 5 psi), P_{atm} is atmospheric pressure, v_{out} is the average velocity at the outlet, g is the acceleration due to gravity, and ρ is the density of the fluid. We note that Equ. (2) ignores the effect of head loss due to contraction effects, which is a valid assumption in laminar flow regimes.[23] The head loss per unit length ($S = h_f/L$) can be related to the Darcy friction factor (f_D) through the Darcy-Weisbach equation as:[25]

$$f_D = \frac{\pi^2 g D^5 S}{8Q^2} \quad (3)$$

The mean wall shear stress (τ) that cells are exposed to during the 3D bioprinting process can subsequently be estimated in terms of the Darcy-Weisbach friction factor as:[26]

$$\tau = \frac{1}{8} f_D \rho v_{out}^2 \quad (4)$$

As shown in **Figure 4.2e**, the head loss per length ranged from 98.9 ± 3.4 to 53.7 ± 2.0 over the diameter range 100 to 500 μm. While this study provides insight into the roughness of the fiber channel walls and illustrates the ability to understand 3D bioprinting quality in terms of quantitative estimates of the shear stress experienced by cells, it should be noted that the shear stress generated in practice can be reduced by decreasing the average outlet velocity of the printed bioink (i.e., the speed of the 3D bioprinting process) as shown in Equ. 4. As shown in **Figure 4.2f**, hollow multifunctional fibers enabled continuous extrusion of alginate bioinks with minimal die swell at the average outlet velocities (*i.e.,* extruder feed rates) for the 3D bioprinting studies discussed in the following sections.

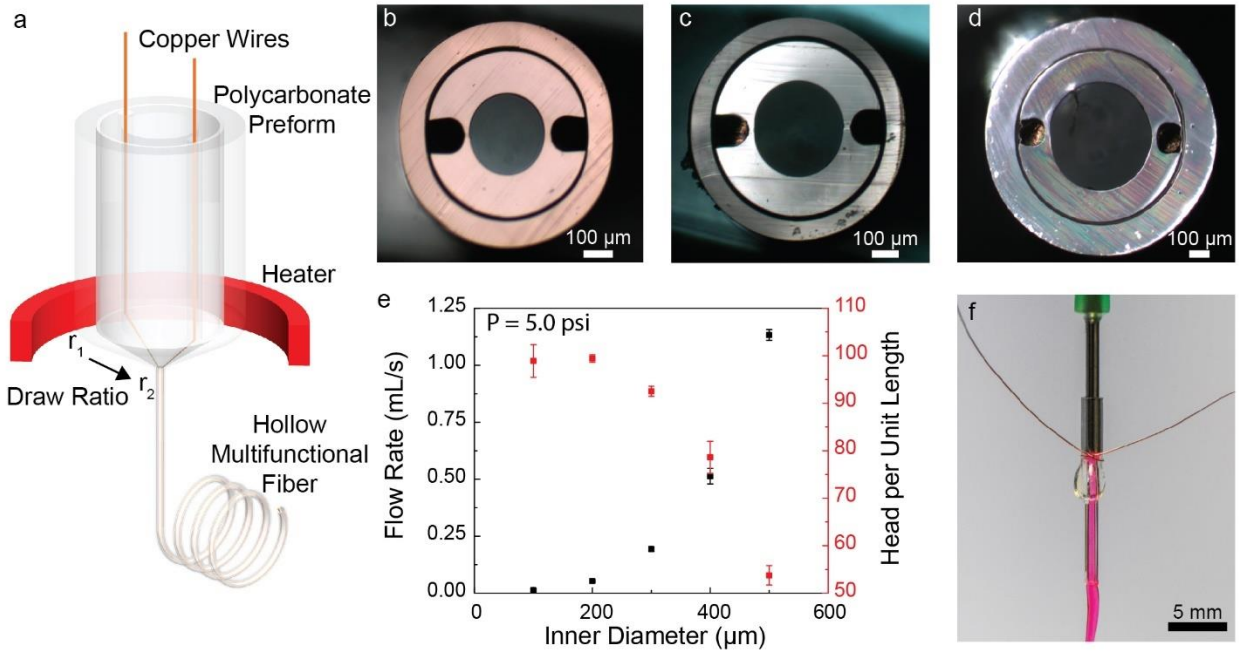

Figure 4.2 Fabrication of hollow multifunctional fibers. a) Schematic of the manufacturing process to produce electrode functionalized hollow multifunctional fibers. A preform tube with imbedded copper wires was drawn, and the draw down ratio controlled the fiber diameter. Cross sections of drawn fibers with inner diameters of 300 (b), 400 (c), 500 µm (d). e) Volumetric flow rate of water in mL/s and head per unit length through 34.0 mm long fibers from an applied pressure of 5.0 psi. f) Image of gel extrusion through a 500 µm diameter fiber, red dye added for visibility.

4.2.3 Detection of cell viability differences

Understanding the effects of material (i.e., bioink) properties and process parameters, such as bioink rheological properties and average velocity of extruded bioink, respectively, on resultant tissue quality remains an active area of research within the biofabrication field. For example, material innovations, such as those based on novel shear-thinning bioinks, are continuing to emerge that reduce the shear stress-induced cell damage and death during 3D bioprinting. Given, the viability of deposited cells is among the most important characteristics to quantify and monitor from a process and quality control perspective, we next examined if the hollow multifunctional fibers could detect the viability of cells within extruded cell-laden bioinks. As shown in **Figure 4.3a** and **4.3b**, alginate-NFC bioinks containing PC-12 cells with either high or low viability at the

same concentration of 5 x 10^5 cells/mL exhibited different impedance responses over the frequency range of 0.1 to 100 kHz and different phase angle responses over the range of 0.1 to 2 kHz. Live/dead stained images taken following bioprinting can be seen in **Figure 4.3c**. As shown in **Figure 4.3d**, the bioinks containing populations of cells with either high or low viability exhibited 89.8 ± 2.8% and 0% viability. As shown in **Figure 4.3a**, bioinks that contained a high population of viable cells exhibited a higher impedance than those that contained a high population of dead cells across the 0.1 to 100 kHz frequency range. The maximum relative difference in impedance between the two bioinks of 118% was observed at 12 kHz. This result agrees with previous impedimetric results, and is attributed to the integrity of the cell membranes.[27,28] As shown in Figure 3b, bioinks that contained a high population of viable cells exhibited a higher phase angle at relatively low frequencies ranging from 0.1 to 2 kHz. Differences in phase angle between the two bioinks was not distinguishable above 2 kHz. The maximum difference in phase angle between the two bioinks of 13.6 degrees was observed at 0.16 kHz. Thus, fixed-frequency impedimetric monitoring of extruded cell-laden bioinks at 160 Hz or 12 kHz could potentially enable real-time monitoring of cell viability in cell-laden 3D-bioprinted materials at high sampling rates. Bioprinted constructs fabricated using the viable bioink were cultured for seven days. We found that the cell viability in the bioprinted tissue constructs was 76.5 ± 8.1% after the curing process (day 1) and did not significantly differ from the cell viability on day 7 (81 ± 2.8%).

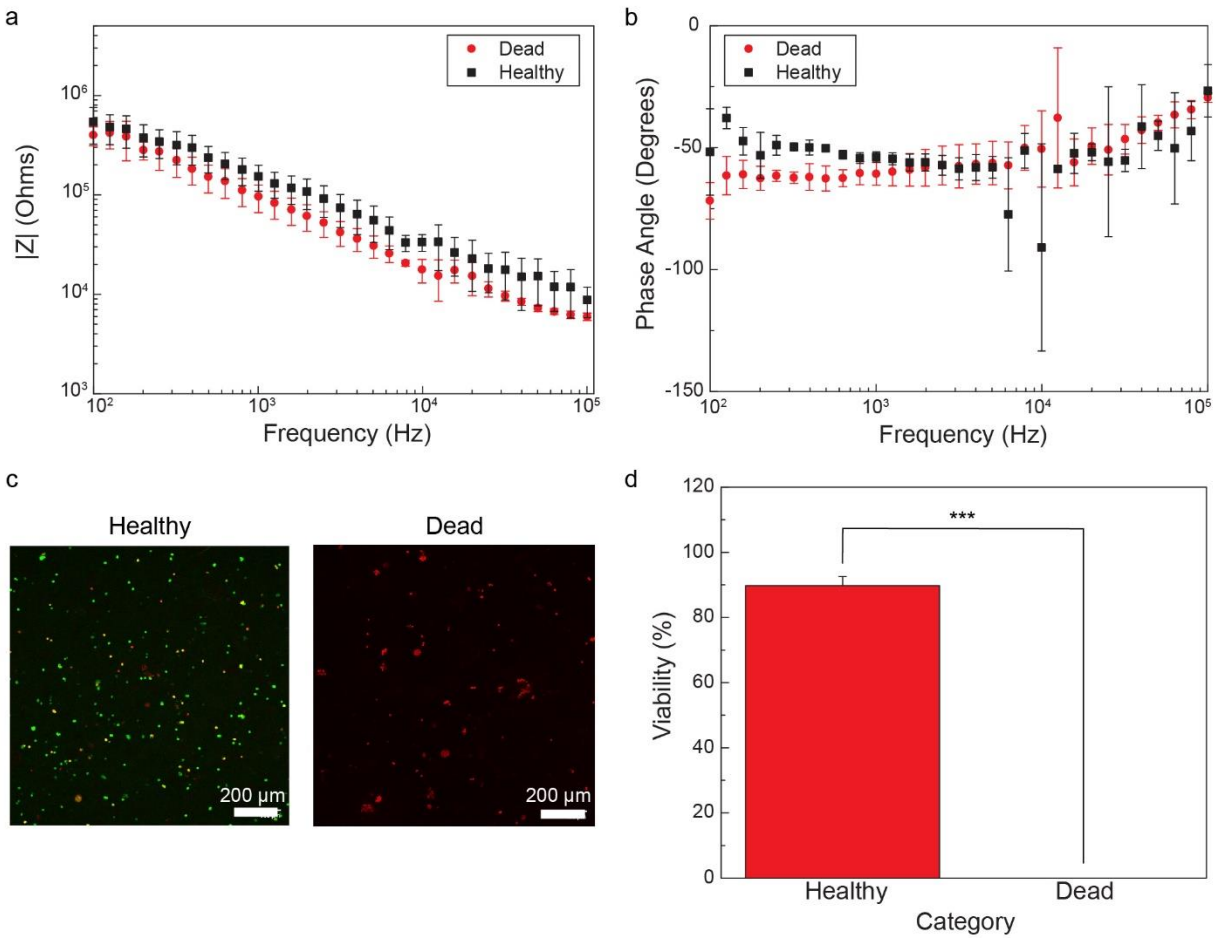

Figure 4.3 EIS recording of bioinks with different cell viabilities. Electrical impedance spectra of hollow multifunctional fibers during 3D bioprinting of cell-laden alginate-NFC bioinks containing 5 x 105 cells/mL shown in terms of the impedance magnitude (a) and phase angle (b) responses (error bars correspond to the standard deviation of measurements obtained from bioprinting of n = 3 constructs). c) Fluorescence micrographs associated with a live/dead stain of bioinks containing populations of PC-12 cells with either high or low viability. d) Viability study of bioinks containing populations of PC-12 cells with either high or low viability (n = 3 biological replicates, *** indicates $p < 0.001$).

4.2.4 Examination of bioinks with different cell type

Having shown that 3D bioprinting using hollow multifunctional fibers enables detection of cell viability differences among cell-laden bioinks, we next examined whether they could also characterize differences in cell type. While many bioprinted constructs are composed of a single cell type, applications of 3D bioprinting to fabrication of organ-on-a-chip system requires bioprinting of multiple cell types on a single substrate.[29-31] In addition to fabrication of organ-chip

platforms, applications of 3D bioprinting for fundamental study of cell migration[32] and cell-laden scaffolds for repair of complex injuries requires[31] bioprinting of multiple cell types in a single construct. As shown in **Figure 4.4a** and **4.4b**, alginate-NFC bioinks containing either PC-12 cells or fibroblasts at the same concentration of 1 x 10^6 cells/mL exhibited different impedance responses over the frequency range of 0.1 to 100 kHz. Live/dead stained images taken following bioprinting can be seen in **Figure 4.4c**. As shown in **Figure 4.3d**, the PC-12 cell- and 3T3 cell-laden bioinks exhibited cell viabilities of 70.5 ± 5.8 and 92.5 ± 4.2%, respectively. As shown in Figure 4a, bioinks that contained PC-12 cells exhibited a higher impedance than those that 3T3 cells across the 0.1 to 100 kHz frequency range. The maximum relative difference in impedance between the two bioinks of 153%occurred at 0.1 kHz, which was different than the location of the maximum impedance difference associated with sensing of bioink cell viability (12 kHz) (see Figure 3a). As shown in **Figure 4.4b**, bioinks that contained PC-12 cells exhibited a higher phase angle than those that contained 3T3 cells across the 0.1 to 100 kHz frequency range. The maximum difference in phase angle between the two bioinks of 10.8 – 11.7 degrees was observed across the 1 – 5 kHz frequency range. Thus, fixed-frequency impedimetric monitoring of extruded cell-laden bioinks at 0.1 kHz or a fixed frequency within the 1 - 5 kHz could range potentially enable real-time monitoring of cell type in cell-laden 3D-bioprinted materials (e.g., bioinks) at high sampling rates. Bioprinted constructs fabricated using the viable bioink were cultured for seven days. The 3D bioprinted PC-12 cell- and 3T3 cell-laden bioprinted tissue constructs exhibited day-7 cell viabilities of 74.6 ± 7.4 and 87.0 ± 2.1%, respectively (see Supplementary Figure S5 for associated live/dead stains).

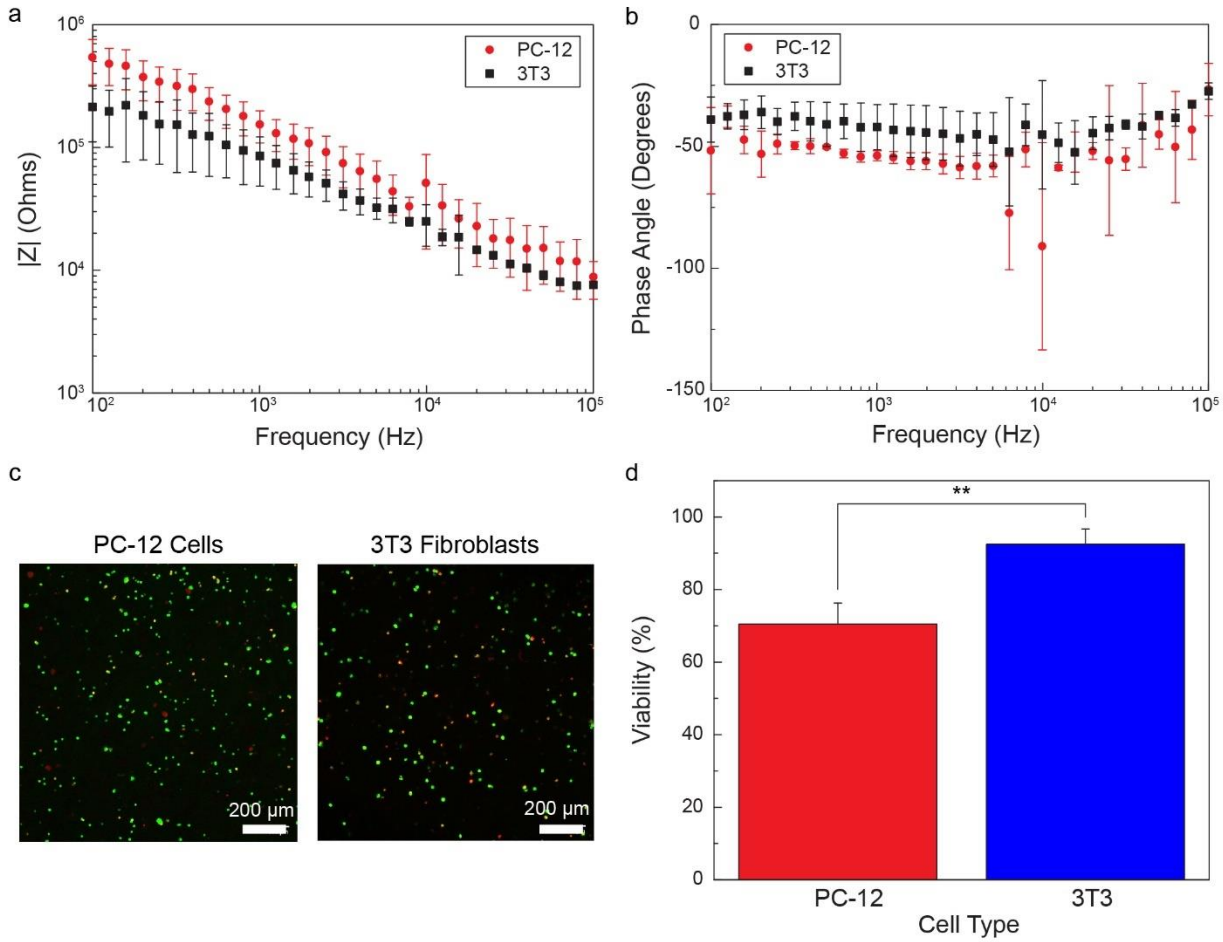

Figure 4.4 Bioimpedance reading of bioinks with diverse cell types. Electrical impedance spectra of hollow multifunctional fibers during 3D bioprinting of PC-12 cell- and 3T3 cell-laden alginate-NFC bioinks containing 1 x 106 cells/mL shown in terms of the impedance magnitude (a) and phase angle (b) responses (error bars correspond to the standard deviation of measurements obtained from bioprinting of n = 3 constructs). c) Fluorescence micrographs associated with a live/dead stain of bioinks containing viable PC-12 or 3T3 cells. d) Viability study of PC-12 or 3T3 cell-laden bioinks (n = 3 biological replicates, ** indicates $p < 0.01$).

4.2.5 Signal response to stem cells and differentiated cells

In addition to the ability to detect changes in cell viability and types, the ability to classify the state of 3D bioprinted cells remains an important process monitoring challenge, particularly for biofabrication of quality 3D bioprinted stem cell therapies. Given stem cell pluripotency and stability are required for effective function of associated 3D bioprinted stem cell therapies, it remains a present biomanufacturing challenge to preserve pluripotency and maintain stem cell

stability during processing based on the tendency of stem cells to spontaneously differentiate into terminal cell types.[33] Having shown that 3D bioprinting using hollow multifunctional fibers enables detection of cell viability and cell type differences among cell-laden bioinks, we next examined if they could also characterize differences in the extent of differentiation among stem cells comprising a stem cell-laden bioink. Embryonic stem cells can be stabilized in a self-renewing state through the application of leukemia inhibitory factor (LIF).[34,35] As shown in **Figure 4.5a** and **b**, alginate bioinks containing mESCs at 1 x 10^6 cells/mL cultured in the presence or absence of LIF exhibited distinguishable impedance responses across the 0.1 – 100 kHz frequency range. As shown in **Figure 4.5a** and **b**, bioinks that contained a high population of stem cells (94.1% stem cells; + LIF) exhibited a lower impedance and phase angle than those in which a significant fraction of stem cells (56.8% differentiated cells; – LIF) had undergone differentiation across the 0.1 to 100 kHz frequency range. As shown in **Figure 4.5a**, the difference in impedance between the two bioinks of ranged from 69% at 100 kHz to 136% at 1 kHz, but the differentiated group (- LIF) exhibited higher impedance across the 0.1 to 100 kHz frequency range. The highest signal to noise level was achieved above 30 kHz. As shown **Figure 4.5b**, the largest difference in phase angle between the bioinks occurred in the 0.1 – 5 kHz frequency range, with the maximum difference of 17.1 degrees occurring at 0.1 kHz.

As shown in **Figure 4.5c** and **d**, mouse embryonic stem cells (mESCs) exhibited significant differences in expression of stage specific embryonic antigen-1 (SSEA-1), an established stemness marker, after culture in the presence or absence of LIF for 14 days (+ LIF and – LIF, respectively). As summarized in Figure 5e, stem cells cultured in the presence and absence of LIF (i.e., + LIF and – LIF, respectively) tested 94.1 ± 2.1 and 43.2 ± 7.6% positive for SSEA-1, respectively.

To investigate the impact of extrusion through the hollow multifunctional fiber on stem cell viability, the viability of stem cells in 3D bioprinted constructs was compared with that in molded constructs, which served as the control group. Micrographs associated with the live/dead assay in the 3D bioprinted and molded stem cell-laden tissue constructs are shown in **Figure 4.5f-i**. As shown in **Figure 4.5j**, the extruded + LIF and – LIF stem cell-laden 3D bioprinted constructs exhibited similar viability (86.8 ± 3.7% and 88.6 ± 2.7%, respectively) and extrusion of stem cell-laden bioinks through the hollow multifunctional fiber had a minimal effect on cell viability relative to the molding process (86.8 ± 3.7% vs. 89.7 ± 2.9 for the + LIF group, respectively, and 88.6 ± 2.7% vs. 92.6 ± 1.2% for the – LIF groups, respectively).

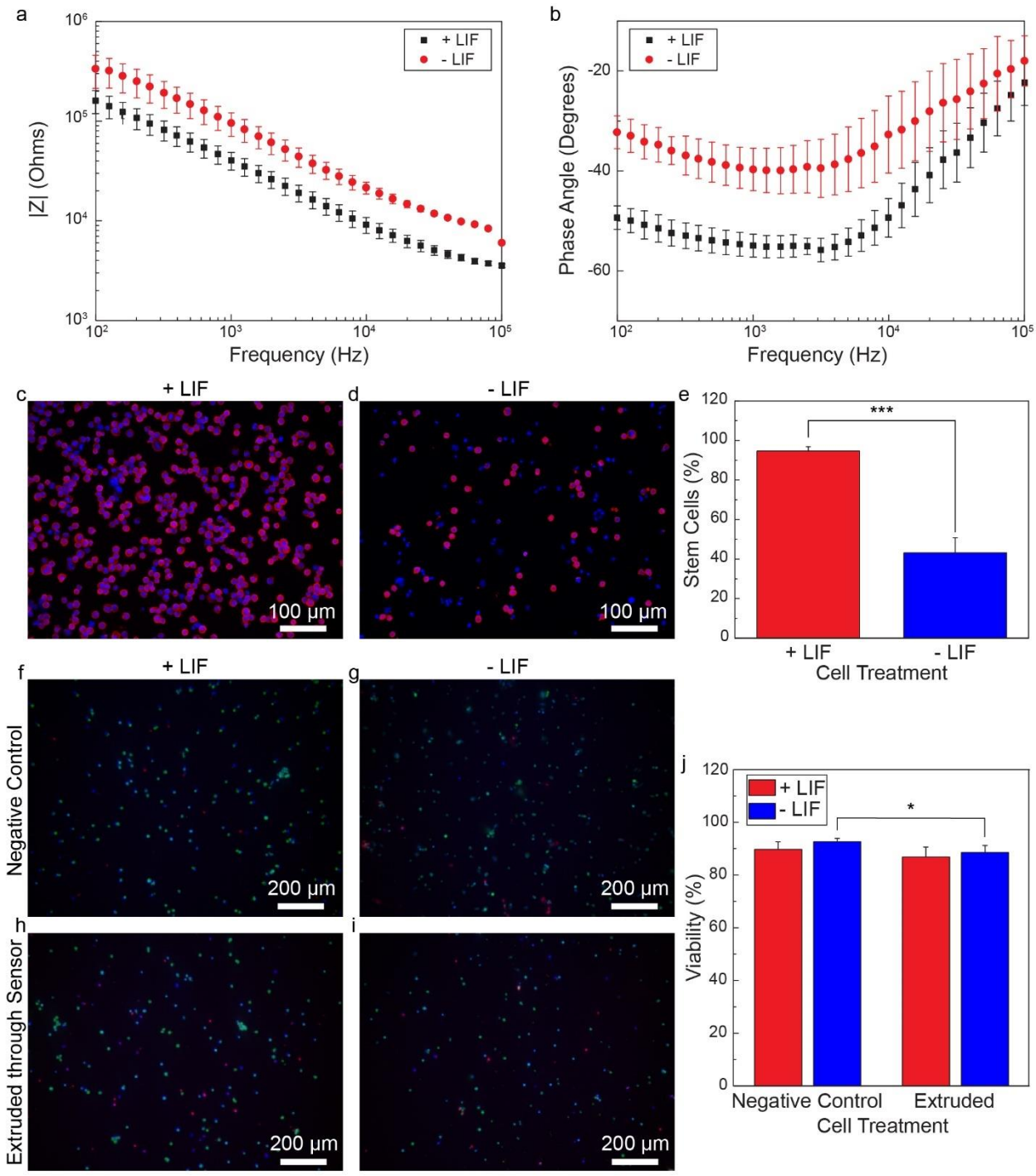

Figure 4.5 Measurements of bioinks to the extent of diffrenciation. Impedance magnitude (a) and phase angle (b) of stem cells (+ LIF) and spontaneously differentiated cells (– LIF), averages of n = 3 samples shown. Merged fluorescent micrographs (200x) associated with expression of SSEA-1, a mESC specific marker, in mESC cultures stabilized in a stem cell state (+ LIF) (c) and allowed to spontaneously differentiate (– LIF) (d), which served the basis of the stem cell-laden bioinks. e) Percentage of stem cells present in a stem cell state based on SSEA-1 expression data following 14 days of culture in +LIF and – LIF media (i.e., panels c and d) (*** indicates $p < 0.001$, n = 3). Fluorescent micrographs (100x) associated with live/dead assays of stem cells in a

stem cell state (+ LIF) (f and g) and in a spontaneously differentiated state (– LIF) (h and i) in both bioprinted and molded constructs using calcein AM, EthD-1, and Hoechst 33342 (nuclei). j) Summary of stem cell viability after following processing (* indicates $p < 0.05$, $n = 3$).

4.3 Conclusions

Here, we demonstrate the capability of in-line monitoring of cell-laden bioink composition and quality during 3D bioprinting processes via impedimetric sensing. 3D bioprinting using hollow electrode functionalized fibers with controlled inner diameter enabled impedance spectroscopy of cell-laden bioinks during extrusion across the 10^2 to 10^6 Hz frequency range. Monitoring of fiber electrical impedance was shown to enable sensing of bioink compositional characteristics, such as cell viability, type, and extent of stem cell differentiation. This work shows that microextrusion 3D bioprinting using hollow multifunctional fiber sensors provides a potential path to improving process monitoring capability of 3D bioprinting processes, particularly regarding in-line monitoring of deposited cell viability, type, stemness, and extent of differentiation. This work also suggests that fiber-based sensors may provide useful platforms for controlled delivery of cell therapies, such as injectable stem cell therapies.

4.4 Materials and methods

Hydrogel Preparation Alginate solutions were prepared by dissolving alginate in DPBS at room temperature under constant stirring for 24 hours. An alginate concentration of 1 wt% was prepared for fibroblast and neuronal cell experiments, and a concentration of 0.25 wt% was prepared for embryonic stem cell (mESC) experiments. Following preparation, 2 wt% NFC was added to the 1 wt% alginate solution used for fibroblast and neuronal cell 3D printing and homogenized under sonication for 90 seconds (FB705 with microtip accessory, Fisher Scientific). All solutions were autoclaved at 121 °C for 30 minutes prior to use.

Cell Culture and Differentiation Neuronal cells from the rat adrenal gland (PC-12, ATCC) were cultured in RPMI-1640 supplemented with 10% v/v horse serum, 5% v/v FBS, and 100 U mL−1 penicillin-100 μg mL−1 streptomycin at 37 °C and 5% CO_2. The PC-12 cells grew as a suspension. The cell medium was changed twice weekly. PC-12 cells for low-viability bioinks were prepared via nutrient deprivation for one week, which was initiated when the culture reached confluence.

Mouse embryonic fibroblasts (NIH/3T3, ATCC) were cultured in DMEM/F12 supplemented with 100 U mL−1 penicillin-100 μg mL−1 streptomycin and 10% v/v FBS at 37°C and 5% CO_2. The 3T3 cells grew as adherent cultures. Passaging was performed using treatment with Typsin-EDTA solution at 90% confluency.

The mouse embryonic stem cells (mESCs) (C57BL/6; Cat. SCRC-1002; ATCC) was cultured in 0.1% gelatin-coated plates at 37^{o}C, 21%O_2 and 5%CO_2 with high-glucose DMEM supplemented with 15% ES-cell qualified FBS, 1000 U/ml leukemia inhibitory factor, 0.1 mM nonessential amino acids, 0.1 mM 2-mercaptoethanol, 2 mM L-glutamine, and 1X penicillin streptomycin with daily medium change. To induce spontaneous differentiation, mESCs were washed twice with phosphate-buffered saline (PBS) and then cultured in the same medium, except in the absence of LIF. Medium was changed every 2 days.

Fabrication of Hollow Multifunctional Fibers Similar to previous functional fibers,[17] PC films were first wrapped round a Teflon rod (diameter = 6.35 – 12.7 mm) and placed in a heated oven (T = 200 ˚C). After the consolidation of the materials by heating, the Teflon rod was removed resulting a uniform PC tube. Single grooves (diameter = 3.175 – 4.37 mm) were then machined on opposite sides of the tube surface. A thin layer of PVDF (thickness = 0.12 mm) and thick layer of PC (thickness = 3 mm) were then rolled on the machined PC tube. The assembly was then placed in the vacuum oven to facilitate material forming and consolidation. A copper wire (16

gauge) was passed through each of the two channels that remained from the machining process to complete the fabrication of the preform. Hollow multifunctional fibers were subsequently drawn from the perform using a thermal drawing process, which was performed under controlled temperature and stress using a custom furnace (temperatures in the pre-heating section, heating section, and cooling section were 150, 285, and 110 °C, respectively). Fiber drawing was done at constant velocity (85 cm/min).

Upon initial production of the fiber, the copper electrodes were exposed on both ends of the fiber. To prevent contact between the electrodes and the extrudate at both the entrance and exit to the fiber, the exposed electrodes at the entrance were blocked with medical epoxy. This ensured the two electrodes would only contact the material at one location, at the exit of the fiber. To provide an opening for connecting leads to the copper wires embedded in the fiber, a scalpel was used to remove material along a section of the outer walls of the fiber exposing the embedded copper wire. Silver paint was used to connect the exposed copper wire in the fiber to copper leads. To build the fluidic connection, the fiber was inserted into the ethylene vinyl acetate tubing (0.5 mm inner diameter) and the whole device was affixed with 5-min epoxy. The tubing was slid onto 18-gauge syringe tips to form a tight seal (see Supplementary Figure S1 for a schematic illustrating the assembly process).

3D Bioprinting of Cell-laden Bioinks Following cell resuspension in fresh pre-warmed growth medium, cell-laden bioinks were then created by combining cell suspensions and 2 wt% alginate solutions at a 1:1 ratio by volume. 2 mL of 1 wt% cell-laden alginate bioinks with 2 wt% NFC were loaded into sterile 5 cc syringe barrels with 500 μm diameter tips that contained the hollow fibers. Tips and fibers were sterilized with 70% ethanol prior to use. The PC-12 and 3T3 cells were collected as a single-cell suspension in phosphate-buffered saline (PBS, Fisher) following

dissociation with Typsin-EDTA (3T3) or Accutase (PC-12, Sigma). The cell concentration and percent of viable cells was determined using Trypan Blue (VWR) following manufacturer's instructions. Based on the Trypan blue counts, bioinks containing 5 x 10^5 and 1 x 10^6 PC-12 cells/mL, 1 x 10^6 3T3 fibroblasts/mL, and 5 x 10^5 dead PC-12 cells/mL were prepared. All tissue constructs were printed into 6-well plates using a commercial 3D bioprinter (Inkredible+, CELLINK) using extrusion pressures ranging from 2 to 10 psi at a print speed of 1 mm/s print speed. Following printing, 500 µm of sterile 100 mM $CaCl_2$ was applied to each sample and allowed to cure for 120 s before triple rinsing with 2 mL sterile DPBS. All bioprinting was done in a biosafety cabinet. All studies were done using single-layer square tissue constructs (10 x 10 mm^2). Each experimental group contained (n = 6) replicates.

Syringe Extrusion of Cell-laden Bioinks 2 mL of 0.25 wt% cell-laden alginate bioinks containing 10^6 cells/mL were prepared and loaded into 5 mL syringes. Suspensions containing stable stem cells (+ LIF) and spontaneously differentiated cells (– LIF) were prepared at the same concentration. Sterile tips that contained the hollow fibers (diameter = 500 µm) were then attached to the syringe. Cell-laden bioinks were hand printed based on a previously reported technique into petri dishes and subsequently cured with 500 µL of sterile 50 mM $CaCl_2$ by exposure for 120 s followed by triple rinsing with 2 mL sterile DI water.

Sensing Principle and Data Acquisition The configuration of the hollow multifunctional fiber sensor is based on impedance analysis of the circuit composed of the two fiber copper electrodes and the extruded material, which is in the middle of the copper electrodes. The electrical impedance response of the system was done using a potentiostat (Interface 1010E, Gamry Instruments) using a two-electrode format in which one copper electrode served as the working electrode, the other copper electrode served as the counter electrode using an AC voltage of 10

mV and zero DC offset over a range of 0.100 – 100 kHz in a logarithmic sweep with 10 points per decade.

Immunocytochemistry The mESC and differentiated mESC cells were fixed with 4% paraformaldehyde (PFA) at room temperature (RT) for 30 minutes and then cytospun onto glass tissue slides at 1100 revolutions per minute (RPM) for 4 minutes. The resulting cells were then washed twice with PBS, followed by blocking in 1.5% BSA and 0.2% Tween20 buffer for 1 hour at room temperature. The cells were then incubated overnight with 1:250 anti-stage specific embryonic antigen-1 (SSEA-1, Santa Cruz Biotech, Dallas, TX), washed thrice, and stained with a secondary antibody, goat anti-mouse 594, at a concentration of 1:1000 in blocking buffer. Hoechst 33342 was counterstained to label cell nuclei in all groups. An additional set of coverslips were stained with only secondary antibody as a negative control. Fluorescent micrographs were acquired using an Olympus IX73 microscope equipped with a DP70 CCD camera (Olympus, Center Valley, PA). The images were then analyzed using ImageJ software (NIH). At least 1,100 Hoechst cells were analyzed in each group to calculate percent of SSEA-1-positive cells over total number of cells.

Live/Dead Assay of PC-12 and 3T3 Cells At days 1 and 7 following printing, cell viability was assessed with a LIVE/DEAD Assay (ThermoFisher) following manufacturer's instructions. In brief, the bio-printed parts were incubated in a 2μ M calcein AM and 4 μM EthD-1 solution for 30 minutes at 37°C with 5% CO_2. The bio-printed parts were then moved into fresh cell medium for imaging using a laser-scanning microscope (A1R; Nikon) equipped with a Plan Apo 10×/N.A 0.45 air objective. Two independent fields of view were imaged per sample for each condition. Quantification of the percentage of cells that were viable was performed with ImageJ Fiji software. In short, the total volume of cells (green signal from calcein AM plus and red signal from EthD-

1) was calculated by creating a binary representation of the fluorescent signals. Subsequently, the percentage of viable cells was obtained by dividing the calcein AM (green signal) volume from the calculated total volume.

Live/Dead Assay of mESCs and Spontaneously Differentiated Cells Cured alginate hydrogels were dissolved with the addition of 0.1M EDTA. Bioprinted mESC and differentiated mESC cells were centrifuged at 1100 RPM for 4 minutes and then suspended in 1 ml culture medium to remove alginate. Cells were then plated in a 0.1% gelatin-coated 48-well plate (1×10^5 cells per well) and allowed 2 hours to attach to the bottom of the culture dish. Afterward, cells were washed with PBS and incubated with 2 µM calcein AM, 1.25 µM EthD-1, and 1 µM Hoechst 33342 for 20 minutes. Only live cells with intracellular esterase activity could digest non-fluorescent calcein AM into fluorescent calcein. Dead or dying cells containing damaged membranes allowed the entrance of EthD-1 to stain the nuclei. Cells were imaged with Olympus IX73 microscope described above and analyzed using ImageJ software. At least 800 Hoechst cells were analyzed in each group to calculate percentage of dead cells over total number of cells.

The calcein AM/EthD-1 staining was also performed for cells 72 hours following 3D bioprinting, except the cells were cultured and imaged in the hydrogel. The percentage of dead cells was calculated by dividing total red (representing dead cells) fluorescent intensity over total blue (representing total number of cells) fluorescent intensity for each image.

Statistics Statistical analysis was completed in Origin Pro 2016. Student's t-test were used for live/dead and SSEA-1 assays. Chi-squared tests were used for Trypan blue counts. *, **, and *** indicate a p-value (p) less than 0.05, 0.01, and 0.001, respectively. Error bars and ± indicate standard deviation. Number of replicates (n) is specified for each experiment and was greater than three in all cases.

4.5 References

1 Bártolo, P., Chua, C., Almeida, H., Chou, S. & Lim, A. Biomanufacturing for tissue engineering: present and future trends. *Virtual and Physical Prototyping* **4**, 203-216 (2009).

2 Bajaj, P., Schweller, R. M., Khademhosseini, A., West, J. L. & Bashir, R. 3D biofabrication strategies for tissue engineering and regenerative medicine. *Annu. Rev. Biomed. Eng.* **16**, 247-276 (2014).

3 Murphy, S. V. & Atala, A. 3D bioprinting of tissues and organs. *Nat. Biotechnol.* **32**, 773-785, doi:10.1038/nbt.2958 (2014).

4 Mironov, V., Kasyanov, V. & Markwald, R. R. Organ printing: from bioprinter to organ biofabrication line. *Curr. Opin. Biotechnol.* **22**, 667-673 (2011).

5 Mironov, V. *et al.* Organ printing: tissue spheroids as building blocks. *Biomaterials* **30**, 2164-2174 (2009).

6 Pigeau, G. M., Csaszar, E. & Dulgar-Tulloch, A. Commercial scale manufacturing of allogeneic cell therapy. *Frontiers in medicine* **5** (2018).

7 Kumar, A. & Starly, B. Large scale industrialized cell expansion: producing the critical raw material for biofabrication processes. *Biofabrication* **7**, 044103 (2015).

8 Aijaz, A. *et al.* Biomanufacturing for clinically advanced cell therapies. *Nature biomedical engineering* **2**, 362-376 (2018).

9 Clomburg, J. M., Crumbley, A. M. & Gonzalez, R. Industrial biomanufacturing: the future of chemical production. *Science* **355**, aag0804 (2017).

10 Holzberg, T. R. *et al.* Sensors for biomanufacturing process development: facilitating the shift from batch to continuous manufacturing. *Current opinion in chemical engineering* **22**, 115-127 (2018).

11 Gamal, W. *et al.* Impedance-based cellular assays for regenerative medicine. *Philosophical Transactions of the Royal Society B: Biological Sciences* **373**, 20170226 (2018).

12 Nordberg, R. C. *et al.* Electrical cell-substrate impedance spectroscopy can monitor age-grouped human adipose stem cell variability during osteogenic differentiation. *Stem cells translational medicine* **6**, 502-511 (2017).

13 Sharma, R., Blackburn, T., Hu, W., Wiltberger, K. & Velev, O. D. On-chip microelectrode impedance analysis of mammalian cell viability during biomanufacturing. *Biomicrofluidics* **8**, 054108 (2014).

14 Narayanan, L. K., Thompson, T. L., Shirwaiker, R. A. & Starly, B. Label free process monitoring of 3D bioprinted engineered constructs via dielectric impedance spectroscopy. *Biofabrication* **10**, 035012 (2018).

15 Chen, R., Canales, A. & Anikeeva, P. Neural recording and modulation technologies. *Nature Reviews Materials* **2**, 1-16 (2017).

16 Frank, J. A., Antonini, M.-J. & Anikeeva, P. Next-generation interfaces for studying neural function. *Nat. Biotechnol.* **37**, 1013-1023, doi:10.1038/s41587-019-0198-8 (2019).

17 Canales, A. *et al.* Multifunctional fibers for simultaneous optical, electrical and chemical interrogation of neural circuits in vivo. *Nat. Biotechnol.* **33**, 277-284, doi:10.1038/nbt.3093 (2015).

18 Amini, M., Hisdal, J. & Kalvøy, H. Applications of bioimpedance measurement techniques in tissue engineering. *Journal of Electrical Bioimpedance* **9**, 142-158 (2018).

19 Blaeser, A. *et al.* Controlling shear stress in 3D bioprinting is a key factor to balance printing resolution and stem cell integrity. *Advanced healthcare materials* **5**, 326-333 (2016).
20 Haring, A. P., Sontheimer, H. & Johnson, B. N. Microphysiological Human Brain and Neural Systems-on-a-Chip: Potential Alternatives to Small Animal Models and Emerging Platforms for Drug Discovery and Personalized Medicine. *Stem Cell Reviews and Reports* **13**, 381-406, doi:10.1007/s12015-017-9738-0 (2017).
21 Kang, H.-W. *et al.* A 3D bioprinting system to produce human-scale tissue constructs with structural integrity. *Nat. Biotechnol.* **34**, 312, doi:10.1038/nbt.3413 (2016).
22 Rezende, R. A., Bártolo, P. J., Mendes, A. & Filho, R. M. Rheological behavior of alginate solutions for biomanufacturing. *J. Appl. Polym. Sci.* **113**, 3866-3871, doi:10.1002/app.30170 (2009).
23 McCabe, W. L., Smith, J. C. & Harriott, P. *Unit operations of chemical engineering*. Vol. 7 (McGraw-hill New York, 2017).
24 Bird, R. B. Transport phenomena. *Applied Mechanics Reviews* **55**, R1-R4 (2002).
25 Elger, D. F., Roberson, J. A., Williams, B. C. & Crowe, C. T. *Engineering fluid mechanics*. (Wiley Hoboken, NJ, 2016).
26 Chaudhry, M. H. *Applied hydraulic transients*. 3rd edn, (Springer, 2005).
27 Palego, C. *et al.* in *2013 IEEE MTT-S International Microwave Symposium Digest (MTT)*. 1-3.
28 Shafiee, H., Sano, M. B., Henslee, E. A., Caldwell, J. L. & Davalos, R. V. Selective isolation of live/dead cells using contactless dielectrophoresis (cDEP). *Lab on a Chip* **10**, 438-445 (2010).
29 Johnson, B. N. *et al.* 3D printed nervous system on a chip. *Lab on a Chip* **16**, 1393-1400 (2016).
30 Xu, T. *et al.* Complex heterogeneous tissue constructs containing multiple cell types prepared by inkjet printing technology. *Biomaterials* **34**, 130-139, doi:http://dx.doi.org/10.1016/j.biomaterials.2012.09.035 (2013).
31 Merceron, T. K. *et al.* A 3D bioprinted complex structure for engineering the muscle–tendon unit. *Biofabrication* **7**, 035003 (2015).
32 Haring, A. P. *et al.* 3D Printed Multiplexed Competitive Migration Assays with Spatially Programmable Release Sources. *Advanced Biosystems* **4**, 1900225, doi:10.1002/adbi.201900225 (2020).
33 Amit, M. & Itskovitz-Eldor, J. Derivation and spontaneous differentiation of human embryonic stem cells. *J. Anat.* **200**, 225-232 (2002).
34 Hall, J. *et al.* Oct4 and LIF/Stat3 additively induce Krüppel factors to sustain embryonic stem cell self-renewal. *Cell stem cell* **5**, 597-609 (2009).
35 Murray, P. & Edgar, D. The regulation of embryonic stem cell differentiation by leukaemia inhibitory factor (LIF). *Differentiation* **68**, 227-234 (2001).

Chapter 5

Implantable miniature optical fibers for on-demand delivery of checkpoint immunotherapies and tumor impedance measurement

5.1 Introduction

Immune checkpoint blockade (ICB) antibodies against cytotoxic T–lymphocyte–associated protein 4 (CTLA-4) or programmed cell death 1 (PD-1) have demonstrated that reactivating anti-tumor immune responses can regress tumors,[1,2] and these ICB antibodies have been approved by the United States Food and Drug Administration (FDA) for the treatment of a broad range of tumors.[3-7] Simultaneous blockade of both CTLA-4 and PD-1 reverses T cell dysfunction and generates more durable anti-tumor activity than either therapy alone.[5,8-11] However, the response rate of ICB therapeutics tends to be low.[3,5,12,13] Additionally, immune-related adverse events can occur (especially when combined ICB antibodies are used) and can sometimes be life threatening.[3,5,14,15] For example, in one study, 36% of patients with melanoma discontinued treatment with combined ICB antibodies owing to treatment-related adverse events;[5] and 59% of patients had grade 3 or 4 treatment-related adverse events, some of which remained unresolved 5 years after treatment.[11]

In light of the disadvantages of these and other systemic immunotherapeutics, intra- or peritumoral treatments have been evaluated as alternatives.[16] This strategy not only generates a local anti-tumor immune response but also drives inhibition of systemic and distal tumors via the induction of immune memory,[17] and this inhibition enables immunological targeting of disseminated malignancies. Clinically, local immunotherapy has been proposed primarily for the treatment of unresectable tumors or for post-surgical adjuvant therapy to prevent local recurrence.[18] Many locally administered immunotherapeutics, such as various cytokines and anti-

CTLA-4, have been shown to inhibit untreated distal tumors in preclinical studies[19-28] and have also been tested in clinical trials.[29-31]

However, intratumoral injection of immunotherapeutics does not prevent them from entering the systemic circulation and dispersing to distal organs. In mice, intratumorally administered cytokines[32,33] were rapidly cleared from the local injection site and were detected in peripheral organs within minutes of injection. Similarly, in patients being treated for skin cancer, high levels of circulating IL-2[34] or IL-12[35] were observed within 1–3 hours of intratumoral injection. This phenomenon limits the maximum tolerated dose of these agents because of the undesired widespread exposure and off-target inflammatory symptoms. To address this problem, various investigators have linked immunotherapeutic agents, including ICB antibodies and cytokines, to collagen-binding peptide domains for systemic administration, in light of the substantial amounts of collagen present in solid tumors.[36-38] These modified ICB antibodies retain the anti-tumor effects of the unmodified antibodies but have fewer adverse effects. However, the modified antibodies can also bind to normal collagen-containing tissues (e.g., connective tissues, artery walls), which may limit their efficacy and dose.

Another local administration strategy involves implanting degradable scaffolds or hydrogels loaded with immunotherapeutics, such as cytokines or ICB antibodies, to control the localization and activation of dendritic cells[39,40] or T cells.[41-43] This strategy shows superior efficacy to bolus injections, but a mechanism for dosage adjustment, either to lower systemic toxicities or to augment therapeutic responses, is largely lacking. Additionally, some hydrogels and scaffolds require tumor resection prior to implantation, owing in part to their relatively large volume.

Recent progress in on-demand drug delivery[44-48] inspired us to explore a strategy for local drug delivery via a system that would integrate a feedback loop with convenient means for timely presentation of the results of treatment and would allow us to adjust drug loading to potentiate immunotherapy without exacerbating toxicity. Specifically, we envisioned that localized delivery could be realized with an implantable miniaturized device with both delivery and measurement capabilities, preferably lasting for weeks at a time, because durable anti-tumor immunity requires prolonged drug retention.[49] To this end, we have engineered an implantable miniature optical fiber device (IMOD) that can be used for local delivery of ICB antibodies and for monitoring of clinical outcomes by tumor impedance measurement over the course of a few weeks. We chose impedance measurement because unlike other methods such as electron or fluorescence microscopy, this reliable and convenient technique is non-destructive, non-invasive, and not limited by penetration depth.[50] Importantly, we demonstrated that tumor impedance is well-correlated with tumor size in several studies in mice and is responsive to the therapeutic treatments.[51-54] We also included the option of photodynamic therapy (PDT) owing to its capacity to enhance anti-tumor immunity and to prolong intratumoral drug retention.[55] We found that in multiple tumor models, combination therapy involving PDT and localized delivery of ICB antibodies via IMOD cured or delayed tumor growth and elicited durable anti-tumor immune responses.

5.2 Results and discussion

5.2.1 Design and fabrication of IMOD and its use for in vitro drug release

The IMOD comprises of a tubular polycarbonate optical fiber (outer diameter, 1.23 mm; inner diameter, 0.57 mm; light transmission rate, >89%) with a thin chemical-resistant layer of polyvinylidene difluoride bearing two embedded copper microelectrodes (diameter, 125 μm) for impedance measurement (**Figure 5.1a**). [41,42] To load a hydrophobic drug onto the outer surface of

the fiber, we applied multiple alternating layers of a drug-containing poly(lactic-co-glycolic acid) solution in tetrahydrofuran and a highly concentrated poly(lactic acid) (PLA) solution (50 mg/mL in tetrahydrofuran), the purpose of which was to prolong drug release (**Figure 5.1b**).[43] Note that length of the optical fiber and the dosage of the loaded drug could be adjusted to suit its application. Additionally, the inner channel of the resulting coated fiber could be loaded with hydrophilic molecules (e.g., ICB antibodies) via capillary action (**Figure 5.1b**).[44]

Prior to in vivo implantation, the microelectrodes embedded in the fiber were connected to an integrated-circuit chip that was used for impedance measurement (**Figure 5.1c**). In addition, tubing was inserted into the chip to connect to the inner channel of the fiber, which allows for on-demand reloading of a drug (e.g., ICB antibodies) into the optical fiber. Specifically, the tubing could be connected to a syringe containing ICB antibodies solution (**Figure 5.1c, d**); after each injection of the solution, the end of the tubing would be sealed with epoxy glue, which could be removed with scissors for refilling of the tubing.

To test the drug-loading and drug-releasing capabilities of the fibers, we encapsulated rhodamine B, which mimics hydrophobic drugs, into the surface coating of the optical fiber (five cycles, **Figure 5.1e**); and we filled the inner channel of the optical fiber with a solution of fluorescein isothiocynate-bovine serum albumin (FITC-BSA) in phosphate buffered saline. The compounds on the outer surface of the fiber and in the inner channel were visualized by fluorescence imaging (**Figure 5.1e**). When the fiber was immersed in phosphate buffered saline at 37 °C, 90% of the rhodamine was released within 12 hours (**Figure 5.2a**). To avoid direct contact and prevent mechanical effect, transwell assays were set up to test the ability of tumor cells to uptake rhodamine B released from the coated fibers; we found that rhodamine B was effectively absorbed and retained by 4T1 murine mammary carcinoma cells (**Figure 5.2b**).

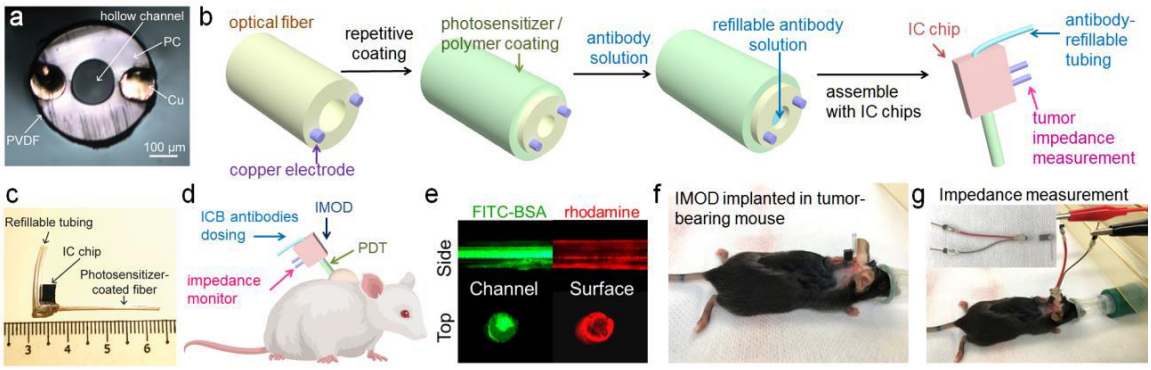

Figure 5.1 Design and fabrication of an implantable miniaturize optical fiber device (IMOD) for on-demand drug delivery and tumor impedance measurement. (a) The cross-section image of uncoated optical fiber with embedded electrodes for measuring tumor impedance. PC, polycarbonate; PVDF, polyvinylidene difluoride. (b) Procedure for coating the optical fiber surface with hydrophobic molecules (e.g., verteporfin or rhodamine) and filling the inner channel of the fiber with hydrophilic drugs (e.g., immune checkpoint blockade (ICB) antibodies or fluorescein isothiocyanate–bovine serum albumin (FITC-BSA)). The obtained fiber was assembled with an integrated-circuit (IC) chip to the IMOD device. (c) The image of IMOD with a refilling tubing and IC chip. (d) IMOD combines photodynamic therapy, immune checkpoint therapy, and impedance measurement, allowing for monitoring of treatment efficacy and adjustment of the antibody dose to generate a sustained anti-tumor immune response while minimizing systemic toxicities. (e) Fluorescence imaging of an optical fiber coated with rhodamine B (red) and loaded with FITC-BSA (green). (f) Implantation of IMOD into a subcutaneous E0771 tumor in a C57BL/6 mouse. g, Connection of IMOD in f via an electrical connector to a Gamry potentiostat for impedance measurement.

The layer-by-layer coating approach was also used with verteporfin, an FDA-approved photosensitizer for PDT; specifically, more than 40 μg of verteporfin per centimeter of fiber could be loaded. An optical fiber coated with alternating layers of verteporfin and PLA released 83% of verteporfin after 12 hours. For slower verteporfin release, we coated the fiber with three more layers of PLA and found that the release rate was substantially lower than that of the fiber without the extra PLA layers, as determined by high-performance liquid chromatography 5 (**Figure 5.2c**). 4T1 breast cancer cell death was observed 20 hours after cells were incubated with a verteporfin-loaded fiber in a transwell and subjected to 20 s of NIR light, while cells that were shielded for NIR light remained healthy, proving that verteporfin released from the fiber could be activated by NIR light (**Figure 5.2d**). Ex vivo intratumoral diffusion experiments were performed by inserting

rhodamine-coated fibers into murine 4T1 mammary tumors excised from BALB/c mice and incubating the fiber-bearing tumors in cell culture medium at 37 °C. The concentration of rhodamine in the excised tumors was retained for up to 10 days (**Figure 5.3a**, **b**). Fibers were also inserted into excised 4T1 tumors and then filled with aqueous Cy5 dye conjugated to BSA (Cy5-BSA) to mimic intratumoral delivery of a hydrophilic agent. Fluorescence imaging showed that Cy5-BSA solution injected via the fibers quickly spread throughout the tumor mass, and the Cy5 fluorescence signals persisted even after 48 hours (**Figure 5.3c**). Taken together, these results showed that both hydrophobic small molecules and proteins could be sustainably delivered via the fiber.

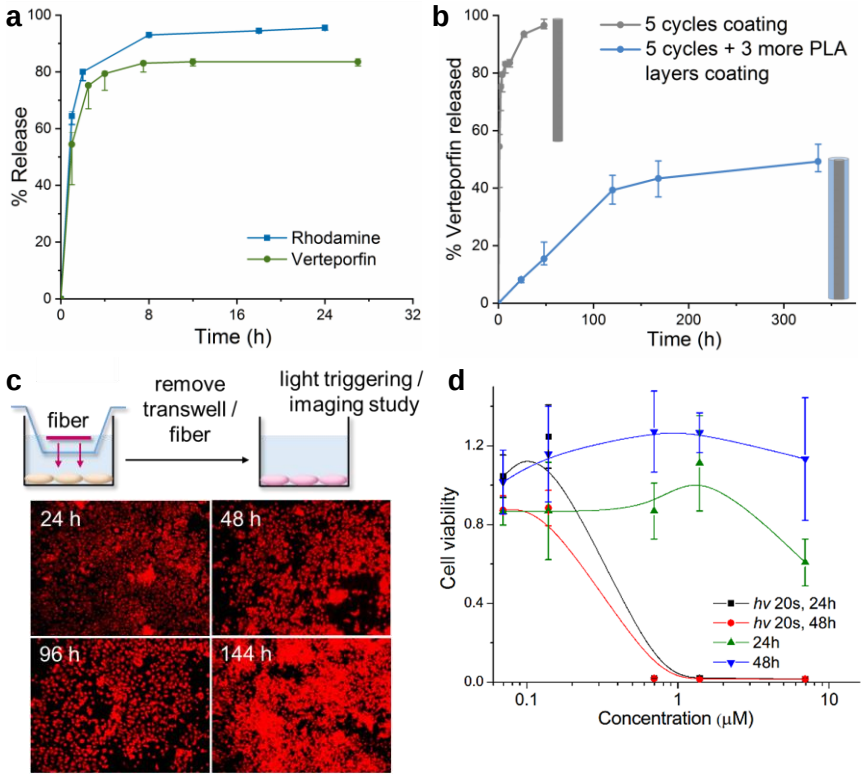

Figure 5.2 In vitro sustained release of drugs loaded onto the fiber in IMOD. (a) Cumulative release of verteporfin or rhodamine over time. (b) Cumulative release of verteporfin from fiber for short-term and long-term purposes. (c) Schematic of transwell assays for *in vitro* imaging and toxicity studies. Fluorescent images were taken of 4T1 cells incubated with rhodamine loaded fibers in transwell between 24 to 144 h. (d) Viability of 4T1 cancer cells (MTT assay) when treated

with verteporfin for 4 h, washed and with or w/o 20 s NIR light irradiation, and further incubated for 24 or 48 h.

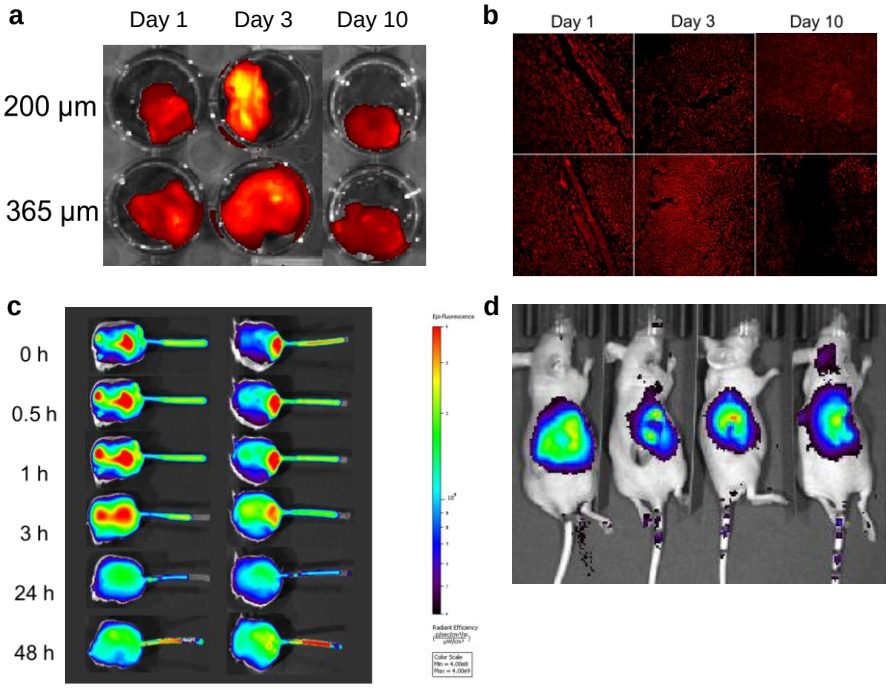

Figure 5.3 Ex vivo intratumoral release of fibers loaded with different drugs. (a) Rhodamine loaded fiber was inserted into excised 4T1 s.c. tumor tissue and allowed to diffuse for 1 to 10 days in Opti-MEM culture medium at 37 °C. (b) Resulting fluorescent images corresponding to experimental conditions in a showing diffused rhodamine within tumor tissue. (c) Cy5-BSA loaded fiber was inserted into excised 4T1 s.c. tumor tissue and left to diffuse for 48 h in Opti-MEM culture medium at 37 °C. The tip of the fiber outside the tumor was sealed. (d) IVIS image shows in vivo diffusion of verteporfin within tumor tissue at 4h post-implantation.

5.2.2 In vivo tumor impedance measurement

Once we fabricated IMOD, we first examined the feasibility of monitoring *in vivo* tumor growth by measuring tumor impedance with IMOD. Since we suspected that tumor heterogeneity may lead to fluctuation of impedance values with tumor depth (**Figure 5.4a**), we carried out ex vivo impedance measurements of isolated 4T1 tumors with different sizes by implanting IMOD at different depths within the tumors. These experiments showed no significant differences between tumor impedance values at various depths, from the center to the periphery of tumors ranging in volumes from 100 to 1200 mm^3 (**Figure 5.4a**).

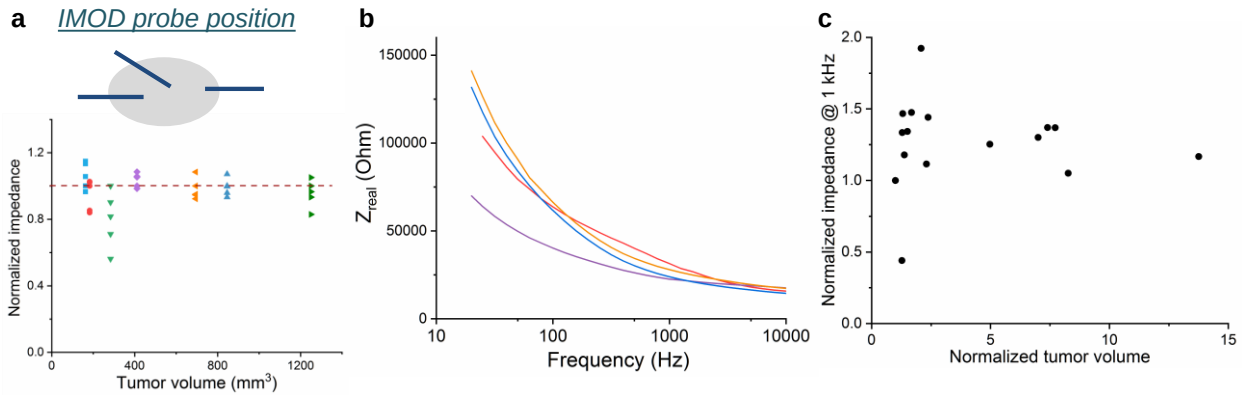

Figure 5.4 The use of IMOD for tumor impedance measurement. (a) Relationship between position of fiber-optic probe with respect to tumor core and corresponding impedance measurement. Ex vivo tumor impedance measured on excised s.c. 4T1 tumor with various tumor volume. Every data point within the same tumor volume was taken at different positions on the tumor. (b) Bode phase impedance plot of s.c. 4T1 tumor over 0.1-10 kHz frequency. (c) No linear relationship between normalized impedance at 1 kHz and normalized tumor volume.

To measure impedance *in vivo*, we implanted IMOD into a subcutaneous (s.c.) 4T1 tumor (50–100 mm^3, ~5 mm diameter, **Figure 5.1c**). Before implantation, the IMOD electrodes were tested in phosphate buffered saline to verify that they were functioning properly. During the measurement, the mouse was under anesthesia, and the implanted IMOD was connected to a Gamry electrochemical potentiostat (**Figure 5.1d**). The whole measurement process lasted about 10 min. Tumor impedance varied with current frequency as shown in the Bode phase impedance plot in **Figure 5.4b**. At a low frequency (1 kHz), impedance did not vary significantly with tumor size (**Figure 5.4c**). In contrast, at a frequency of 10 kHz , which is consistent with the frequency recommended in the literature,[60] normalized impedance increased linearly with increasing normalized tumor size (R^2 = 0.81, n = 6, **Figure 5.5a**). Importantly, we were able to use IMOD to monitor tumor impedance signals over the course of 3–4 weeks of tumor growth. The ability of IMOD to record tumor impedance signals in other types of tumors was also evaluated, and similar linear relationships between impedance and tumor size were observed in s.c. E0771 breast tumors (C57BL/6 mice, R^2 = 0.80, n = 8, **Figure 5.5b**), s.c. CT26 colon tumors (BALB/c mice, R^2 = 0.83,

n = 7, **Figure 5.5c**), and s.c. B16F10 melanoma tumors (C57BL/6 mice, R^2 = 0.91, *n* = 5, **Figure 5.5d**).

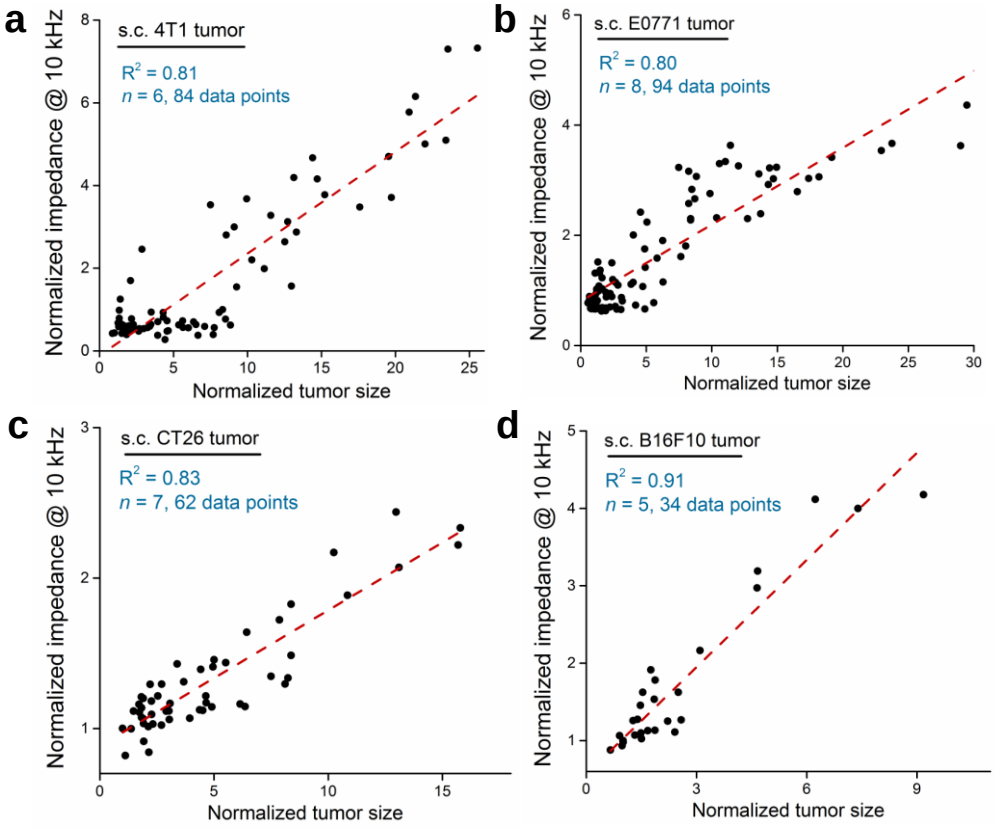

Figure 5.5 In vivo tumor impedance measurements using IMOD. The linear regression relationships (red dashed lines) between normalized tumor size and normalized impedance at 10 kHz were observed for subcutaneous (a) 4T1, (b) E0771, (c) CT26, and (d) B16F10 tumors.

5.2.3 Circuit model analysis

As shown by many researchers, the current predominantly flows through the paracellular space between cells at low frequency and the majority of the current takes the transcellular pathway across the cells when the frequency is over 10 kHz[61-64]. To simulate this current flow, a simplified equivalent circuit model is proposed to gain insights into the obtained impedance spectrum (**Figure 5.6a**). This circuit model consists of a resistance of the Tumor Interstitial Fluid (TIF, R_{TIF}) in series with a constant phase element (CPE) representing double layer capacitor (Z_{DL}) and a parallel

combination of the paracellular resistance (R_{para}) and another CPE simulating the transcellular behavior of the cell (Z_{trans}).

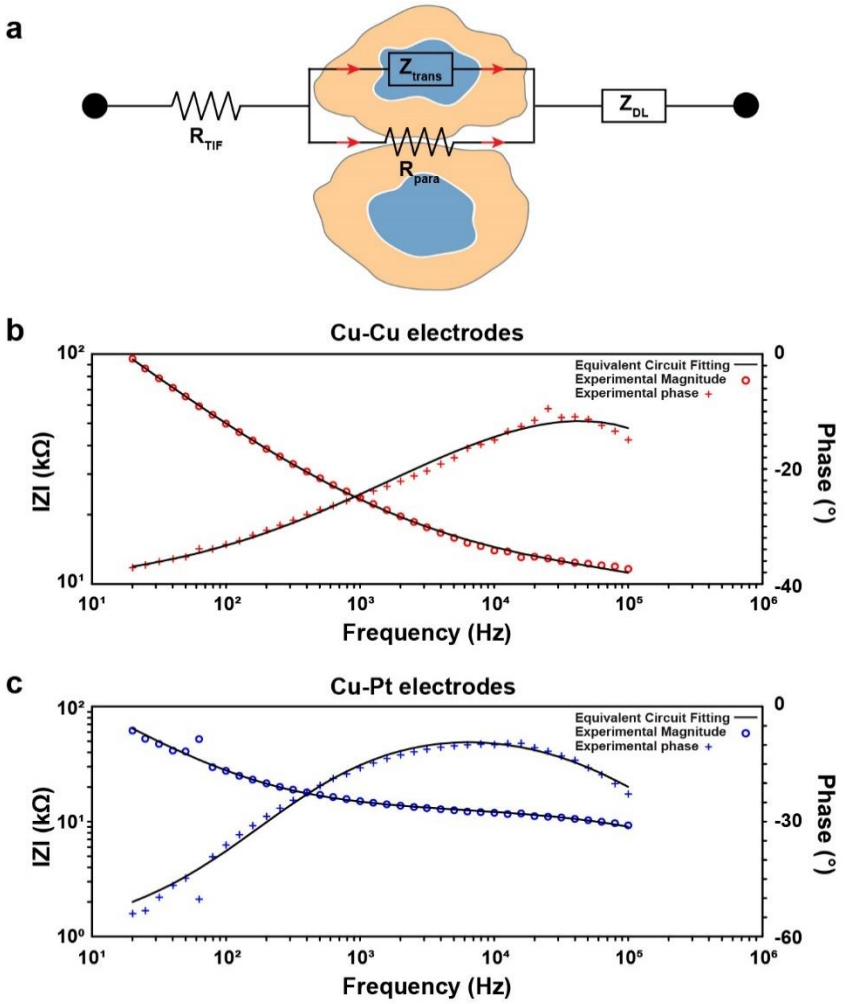

Figure 5.6 Modeling of tumor impedance measurement in E0771 tumors and comparison between experiments and simulation curves. (a) Proposed equivalent circuit model for electrode–tumor tissue interface; (b) Representative EIS impedance spectra for experimental data of copper/copper electrodes in E0771 tumors (red) and equivalent circuit fitting (black) used for curve fitting; (c) Representative EIS impedance spectra for experimental data of copper/platinum electrodes in E0771 tumors (blue) and equivalent circuit fitting (black) used for curve fitting.

The impedance of the constant phase element is $Z = \frac{1}{A(j\omega)^n}$, where $i = \sqrt{-1}$, $0 < n <$ 1. The angular frequency $\omega = 2\pi f$ with f as frequency in Hz, and A is the CPE admittance at $\omega =$ 1 rad/s. The parameter n is such that if $n = 1$, the impedance of a CPE is that of an ideal capacitor;

and when n = 0, the CPE is a pure resistor. Applying this principle to the constant phase elements in the circuit gives their impedance equals to $\frac{1}{A_{DL}(j\omega)^{n_{DL}}}$ (Z_{DL}) and $\frac{1}{A_{trans}(j\omega)^{n_{trans}}}$ (Z_{trans}), respectively. Further assignment is also given by assuming that the resistive elements TIF and paracellular pathway both possess simple resistance, R_{TIF} and R_{para} correspondingly. Combining the above definitions give the total impedance of the proposed circuit, Z_{Total} as

$$Z_{Total} = R_{TIF} + Z_{DL} + \left(\frac{1}{R_{para}} + \frac{1}{Z_{trans}}\right)^{-1} \quad (1)$$

$$= R_{TIF} + Z_{DL} + \left[\frac{Z_{trans}R_{para}}{Z_{trans}+R_{para}}\right] \quad (2)$$

Replacing Z_{SL} and Z_{DL} with their corresponding definitions give the overall circuit impedance as

$$Z_{Total} = R_{TIF} + \frac{1}{A_{DL}(j\omega)^{n_{DL}}} + \frac{\frac{1}{A_{trans}(j\omega)^{n_{trans}}}R_{para}}{\frac{1}{A_{trans}(j\omega)^{n_{trans}}}+R_{para}} \quad (3)$$

The proposed equivalent circuit model was used to fit the obtained impedance spectra measured using IMOD equipped with copper – copper electrodes within subcutaneous E0771 tumor (**Figure 5.6b).** A representative impedance spectrum was also given for impedance recorded using implanted IMOD with platinum – copper electrodes under similar experimental settings (**Figure 5.6c**). Fitting results were calculated and plotted using Echem Analyst™ software by Gamry Instruments. The parameters for this equivalent circuit model are listed in **Table 5.1** with mean values and standard deviations.

Due to the fact that the IMOD was immersed in solid tumor when performing the electrochemical impedance spectroscopy, the effective thickness or the distance of the TIF that contributes to the R_{TIF} is relatively small. Moreover, since the ionic composition of TIF is very close to that of plasma, which has the electrical conductivity of 14.3 mS cm^{-1} at body

temperature[65,66], we hypothesize that R_{TIF} is negligible in the circuit which is further validated by the equivalent circuit fitting results shown in the table.

	Cu-Cu electrodes		Cu-Pt electrodes	
	mean	SD	mean	SD
R_{TIF} (Ω)	558.33	71.28	554.33	59.57
A_{DL} ($S^*S^{n_{DL}}$)	1.27×10^{-6}	0.04×10^{-6}	7.75×10^{-7}	0.76×10^{-7}
n_{DL}	0.45	0.05	0.66	0.01
R_{para} (kΩ)	9.68	0.18	11.67	0.33
A_{trans} ($S^*S^{n_{trans}}$)	5.18×10^{-10}	0.44×10^{-10}	1.05×10^{-8}	0.09×10^{-8}
n_{trans}	0.77	0.01	0.64	0.01

Table 5.1 Means and standard deviations (SD) of parameters in the equivalent circuit model from different impedance measurement experiments.

From the averaged fitted results of the E0771 tumors, we can observe that the paracellular resistance and transcellular impedance are the critical components in the impedance composition. We next investigate the relations between the normalized tumor size and paracellular resistance (R_{para}) or transcellular impedance ($1/A_{trans}$, as the impedance of a capacitor is inversely proportional to its capacitance). As shown in **Figure 5.7**, we discover that the normalized paracellular resistance and transcellular impedance increased linearly with the normalized tumor size which correlates to our findings of the relationship between the normalized impedance value at a frequency of 10 kHz and the tumor size. This phenomenon can be further explained by the increase of the tumor cell number as tumor gets larger, leading to the proportional increase of the R_{para} and $1/A_{trans}$, which results in the proportional increase of the total impedance Z_{TOTAL}. This linear relationship between the normalized tumor size and normalized impedance may potentially indicate the regular growth patent of the tumor associated with the increase of the impedance at a constant rate.

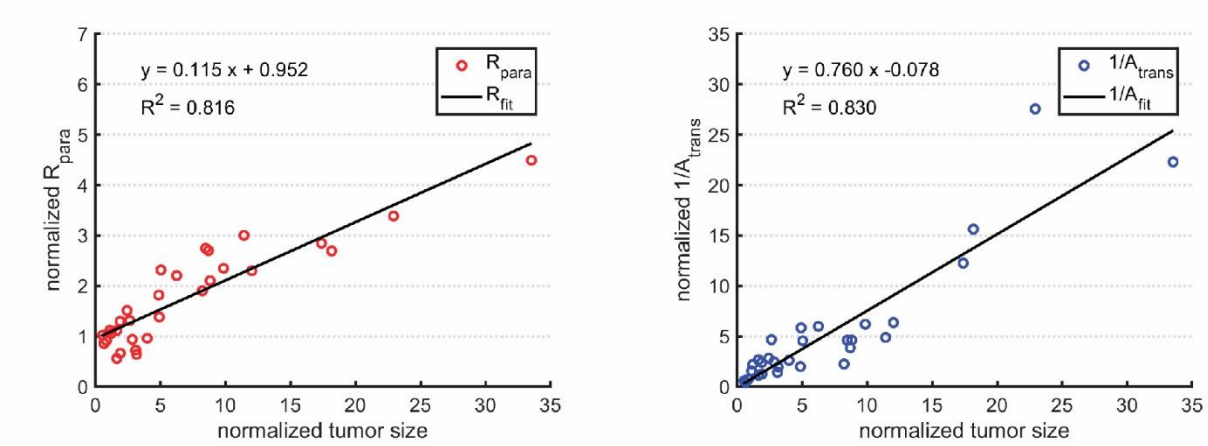

Figure 5.7 Combined fitting results of tumor G4M2 and G4M3. Normalized Rpara and 1/Atrans increased linearly with the normalized tumor size.

5.2.4 Effect of PDT on intratumoral drug retention

The ability of the optical fiber in IMOD to transmit light enabled us to use PDT, which is an FDA-approved, minimally invasive therapeutic modality[67] in which an inactive light-sensitive molecule, called a photosensitizer, reacts with oxygen upon light irradiation to form reactive oxygen species that are cytotoxic to tumor cells.[68] Treatment of murine tumors by means of localized PDT reportedly increases anti-tumor immunity by releasing antigens and inflammatory cytokines from dying tumor cells.[68,69] Several studies using the combination of ICB and PDT, in which various photosensitizers or nanoparticles were administered, suggested that this combination shows enhanced anti-tumor efficacy relative to individual treatments.[70-73] Notably, enhanced tumor vessel permeation of therapeutics has been observed in PDT-treated mice and has been utilized to improve intratumoral accumulation of nanoparticles and drugs.[74-76]

We then assessed whether PDT could improve intratumoral retention of ICB antibodies. We selected Cy7-BSA to mimic ICB antibodies because fluorescently labeled BSA is easy to prepare on a milligram scale for imaging studies. In addition, the molecular weight of BSA (55 kDa) is close to the molecular weights of anti-PD-1 (~40 kDa) and anti-CTLA-4 (~35 kDa).We

administered Cy7-BSA via IMOD 4 hours after PDT (i.e., verteporfin administration and light irradiation), and we then monitored the distribution of Cy7-BSA fluorescence by means of a whole-body imaging system. The fluorescence signal for Cy7-BSA was observable in the tumor for approximately 1 week (half-life, 31.0 hours; **Figure 5.8a, c**). Conversely, Cy7-BSA administered through IMOD without prior PDT was quickly cleared from the tumors (half-life, 4.2 hours; **Figure 5.8b, c**). Note that prior to PDT (4 hours after implantation of IMOD), verteporfin stayed mainly around the tumor site (**Figure 5.3d**).

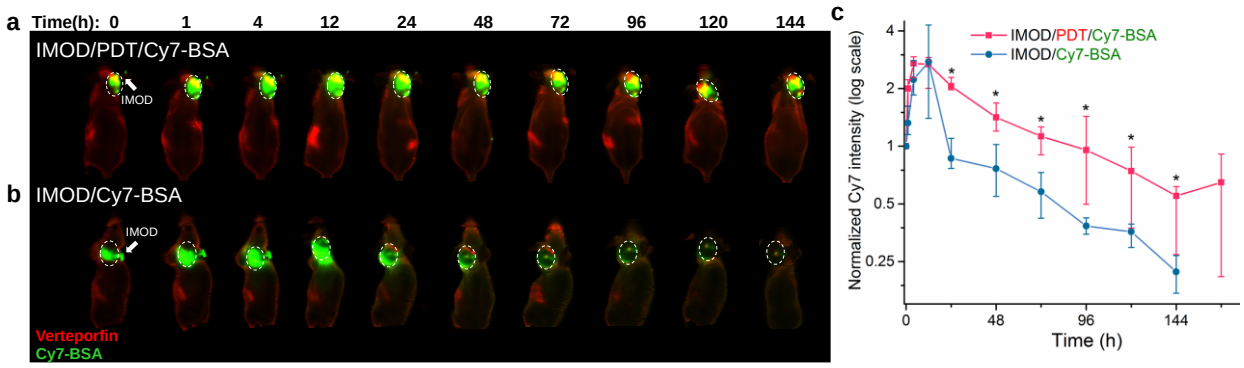

Figure 5.8 Effect of photodynamic therapy (PDT) on intratumoral retention of proteins. Representative whole-body fluorescence images of (a) 4T1 tumor–bearing nude mice with an implanted IMOD (white arrow) that received PDT (red, −4 h) and Cy7–bovine serum albumin (BSA) via IMOD (0 h); (b) 4T1 tumor–bearing nude mice that received Cy7-BSA via IMOD (0 h). In both panels, the tumors are indicated with white dashed circles. (c) Time course of normalized intratumoral Cy7 intensity over 1 week ($n = 5$) for the mice shown in a and b. Data are medians ± quartiles. Asterisks indicate $P < 0.01$, determined by Mann–Whitney *U*-tests.

5.2.5 Tumor impedance measurement responds to the ICB antibody treatment via IMOD

Next, we determined whether tumor impedance measured via IMOD would respond to the administered treatment—in other words, whether the tumor impedance readings would synchronously respond to the reduction in tumor size. First, we confirmed that tumor impedances measured by IMOD responded to treatment with intraperitoneally injected ICB antibodies (q3d × 3) in mice with s.c. CT26 tumors into which IMOD was implanted. Importantly, we found that the

impedance readings obtained with IMOD correlated with the change in tumor size (n = 5, **Fig. 5a**). Encouraged by these results, we then determined whether IMOD could be used for both impedance measurement and ICB antibody delivery in E0771 s.c. tumor model. The ICB antibodies were administered every 2 days, and impedance values were recorded before injection of the antibodies. We found that in all the treated mice, the decrease in E0771 tumor sizes elicited by the antibodies could be detected from the impedance measurements (n = 6, **Fig. 5b**). These results demonstrate that we could achieve sustained delivery of ICB antibodies while simultaneously measuring impedance to monitor tumor growth.

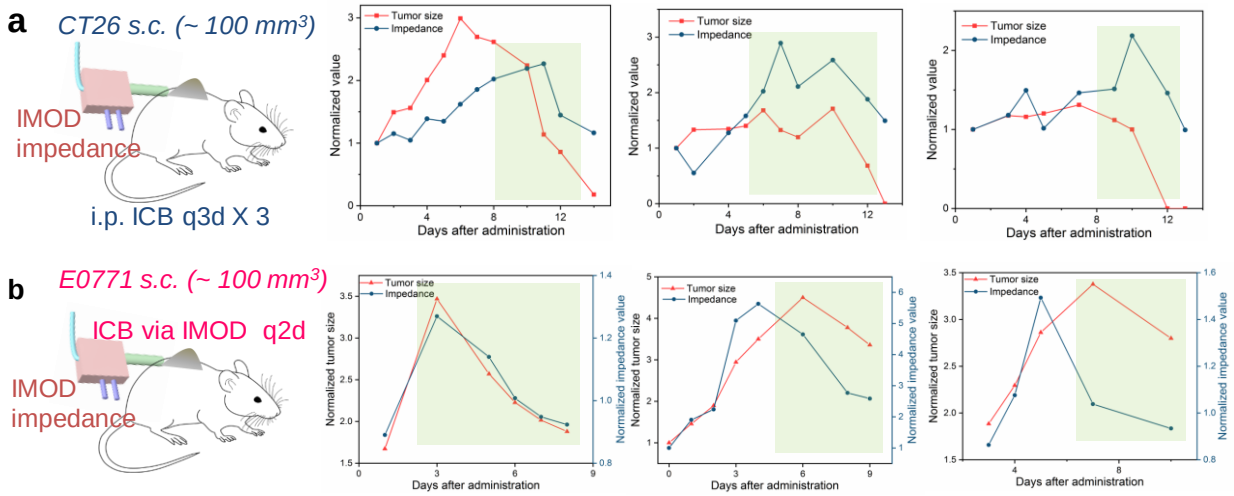

Figure 5.9 Correlation between tumor shrinkage and impedance (highlighted in light green). (a) Representative results for treatment of s.c. CT26 tumor by intraperitoneally (i.p.) injections of ICB antibodies, with tumor impedance measured by an implanted IMOD. (b) Representative results for treatment of s.c. E0771 tumor by injection of ICB antibodies every 2 days via an implanted IMOD. Tumor impedance values were measured by IMOD before administration of treatment.

5.3 Conclusions

In this study, we demonstrated that IMOD allowed us to simultaneously measure tumor impedance and deliver ICB antibodies. Quickly and conveniently determining the efficacy of on-demand drug delivery has long been a challenge, and our miniature device exhibits the potential

to be useful for on-demand local drug delivery, with the versatility to allow changes in the delivered drugs and their concentrations; and use of the device may also decrease systemic toxicities. Combining PDT with delivery of ICB antibodies via IMOD resulted in a durable anti-tumor response, whereas administration of either treatment separately or in combination via different administration routes was often less effective. Importantly, we found that treatment-induced shrinking of tumor volume could be detected by monitoring tumor impedance via IMOD. To improve our understanding of the effects of tumor tissue growth on tumor impedance, we propose a modified Randles equivalent circuit model to fit our experimental results.[77] Data simulated with this model fitted well with our experimental impedance data. Notably, impedance measurements via IMOD were simple to carry out, and we envision that other sensors could be adapted to facilitate rapid *in situ* monitoring of physiological changes in tumors.

5.4 Materials and methods

Fabrication of electrode-embedded fibers and IMOD The fabrication of electrode-embedded fiber was based on reported procedures.[57] In brief, a layer of polycarbonate (PC) film with moderate thickness was rolled onto a teflon rod and consolidated in a vacuum oven to prepare a macroscopic preform that resembles the final fiber geometry. Two slots were machined 180 degree apart for electrode embedding, followed by another layer of PC film till the proper diameter was reached. The preform was consolidated to enable a stable fiber drawing process. After the second consolidation, the teflon rod was removed from the preform and two copper wires were inserted into two machined slots separately prior to the thermal drawing process. During the fiber thermal drawing process, copper wire was pulled from the coil which was mounted on a customized stage above the drawing furnace. As a result of the convergence fiber drawing, the outcome fiber has the structure of one hollow channel in the center and two copper wires opposite to each other

outside the hollow channel (see **Figure 6.1a**). To assemble the fiber device with the integrated circuit chip (IC chip) for impedance measurement, the copper wires in the fiber were manually exposed by a scalpel and electrically connected to external copper wires with conductive silver paint (SPI Supplies, West Chester, PA). These external copper wires were soldered to the headpins of the integrated circuit chip (Sullins Connector Solutions, San Marcos, CA), and epoxy was applied to protect the connection and avoid short circuits.

Optical fiber coating and drug loading To prepare a polymer solution of hydrophobic molecules (e.g., rhodamine B) for fiber coating, a mixture of poloxamer (1000 mg, pluronic F127, Sigma-Aldrich), PLGA (330 mg, poly(D,L-lactide-co-glycolide), molecular weight: 30k-60k, Sigma-Aldrich) in tetrahydrofuran (THF, 5 mL) was agitated vigorously in a 8 mL reaction vial until PLGA solution was homogenous and clear. Saturated rhodamine B / acetone solution was added into the PLGA / THF solution until solution was homogeneous and pink. Similarly, verteporfin (Cayman Chemical, Ann Arbor, MI) / PLGA solution was prepared by adding 2.5 mg/mL of verteporfin / THF solution and 5 mL PLGA solution into an 8 mL reaction vial.

To coat the fiber layer-by-layer with the polymer solution, a polycarbonate optical fiber was dipped into PLA / THF (100 mg/mL) solution and removed slowly so as to create a smooth coating. Next, it was placed into an air-tight chamber connected to vacuum. The coated fiber was dried under vacuum for 30 minutes before it was dipped into the rhodamine B / PLGA solution. The fiber was dried under vacuum again for 60 minutes. This was repeated until there were 11 layers of alternating polymer coatings (additional 1 PLA layer outside of rhodamine B/ PLGA). Verteporfin coated fiber was prepared in a similar way. To extend the release of verteporfin, three additional layers of PLA coatings was coated onto the verteporfin fibers.

Mice and cell lines Balb/c and C57BL/6 mice (ages 4 to 6 weeks female, from Jackson Laboratories or Envigo), and nu/nu mice (ages 4 to 6 week female, from Charles River) were used according to protocols approved by the Institutional Animal Care and Use Committee (IACUC) of Virginia Tech and maintained in pathogen-free conditions in a barrier facilities. The breast cancer E0771 cell line was purchased from CH3 Biosystem (Amherst, NY); the breast cancer 4T1, the colon cancer CT26 and melanoma B16F10 cell lines were originally purchased from the American Type Culture Collection (ATCC, Manassas, VA). All cells were maintained at 37 °C with 5 % CO_2 in culture medium according to the instructions, supplemented with 10% heat-inactivated FBS and penicillin/streptomycin (all from Life Technology, Grand Island, NY).

Subcutaneous tumor inoculation For subcutaneous (s.c.) inoculation of single B16F10, 4T1, E0771, CT26 tumors, 5×10^5 cells in 50 μL of sterile PBS (1×) were subcutaneously injected into the back of neck of C57BL/6 or BALB/c female mice after hair was removed. Treatments were started when tumors reached ~50 mm^3. The body weight and tumor size were measured every 1-2 days after the treatment started. Tumor length and width were measured with a digital caliper, and the tumor volume was calculated using the following equation: tumor volume = length × width × width / 2.[96] Mice were euthanized when their tumor volumes reached a predetermined end point (1000 mm^3) or when their body weights dropped over 10 %. For tumor rechallenge studies, mice that rejected tumors were inoculated with same amount of tumor cells (5×10^5 cells) in the right flank, and monitored for another 2 weeks.

IMOD implantation and treatments Mice receiving treatments through IMOD were placed under anesthesia, with s.c. injection of carprofen (5 mg/kg) as analgesia prior to implantation. Implantation of IMOD started by making a small slit on the edge of tumor using sterile surgical scissors. The optical fiber end of IMOD was gently inserted into tumor and the device was placed

under skin with refillable tubing remaining above skin level (see **Figure 6.1c**). Skin was pulled taut and adhered around device using 3M Vetbond Tissue Adhesive. An ethanol solution (70 %) was applied appropriately to maintain cleanliness of surgical wound. Intratumoral treatments of ICB antibodies via IMOD were administered in 100 µL sterile PBS through refillable channel on IMOD. 100 µg of α-CTLA-4 (clone 9H10, BioXCell, Lebanon, NH) and α-PD-1 (clone RMP1-14, BioXCell) were administered each per dose.

For photodynamic therapy, verteporfin loaded fiber was trimmed to 1 cm per dosage and implanted into tumor. At 4 hours post-implantation, the mouse was anesthetized with isoflurane. The tumor area was irradiated by near infrared light (Kessil H150-red LED light source of 34W, 20 s, 600-700 nm) while the rest of the mouse body was covered by aluminum foil.

***In vivo* tumor impedance measurement** For tumor impedance measurements, tumors were inoculated and allowed to form tumor mass of approximately 50 mm^3, as described above. IMOD was implanted and impedance reading was recorded by connecting Gamry Interface 1000™ Potentiostat to IC chip on IMOD. Mice were placed under anesthesia while all impedance readings were taken. Treatments were given after impedance readings were measured for better consistency. For both measuring and dosing of drugs via IMOD, Pt / Cu were used to replace Cu / Cu electrodes due to its stability for impedance measuring over weeks.

Whole-body fluorescence imaging of mice Whole body fluorescence imaging of mice was performed with LI-COR Biosciences Odyssey Infrared Imaging System with emission wavelength at 700 nm (for verteporfin) and 800 nm (for Cy7-BSA). The nu/nu mice were first subcutaneously inoculated with 5×10^4 4T1 cells in 50 µL PBS (1×) on the back of neck. Similar to the descriptions above, IMOD with verteporfin loaded optical fiber was implanted once tumor length was determined to be approximately 8 mm. The nu/nu mice were fed with alfalfa-free food for at

least one week prior to the study in order to minimize the gastrointestinal background autofluorescence.[97] For imaging studies, a 100 μg/mL Cy7-BSA in 30 μL sterile PBS solution (1×) was injected through refillable tubing on IMOD into the 4T1 tumor after PDT irradiation. Fluorescence images of nu/nu mice were taken at designated time points.

5.5 References

1 Sharma, P. & Allison, J. P. The future of immune checkpoint therapy. *Science* **348**, 56-61, doi:10.1126/science.aaa8172 (2015).

2 Pardoll, D. M. The blockade of immune checkpoints in cancer immunotherapy. *Nat. Rev. Cancer* **12**, 252-264, doi:10.1038/nrc3239 (2012).

3 Hodi, F. S. *et al.* Improved Survival with Ipilimumab in Patients with Metastatic Melanoma. *N. Engl. J. Med.* **363**, 711-723, doi:doi:10.1056/NEJMoa1003466 (2010).

4 Topalian, S. L. *et al.* Safety, Activity, and Immune Correlates of Anti-PD-1 Antibody in Cancer. *N. Engl. J. Med.* **366**, 2443-2454, doi:10.1056/NEJMoa1200690 (2012).

5 Larkin, J. *et al.* Combined Nivolumab and Ipilimumab or Monotherapy in Previously Untreated Melanoma. *N. Engl. J. Med.* **373**, 23-34, doi:10.1056/NEJMoa1504030 (2015).

6 Hamid, O. *et al.* Safety and Tumor Responses with Lambrolizumab (Anti-PD-1) in Melanoma. *N. Engl. J. Med.* **369**, 134-144, doi:10.1056/NEJMoa1305133 (2013).

7 Tang, J., Shalabi, A. & Hubbard-Lucey, V. M. Comprehensive analysis of the clinical immuno-oncology landscape. *Annals of Oncology* **29**, 84-91, doi:10.1093/annonc/mdx755 (2018).

8 Curran, M. A., Montalvo, W., Yagita, H. & Allison, J. P. PD-1 and CTLA-4 combination blockade expands infiltrating T cells and reduces regulatory T and myeloid cells within B16 melanoma tumors. *PNAS* **107**, 4275-4280, doi:10.1073/pnas.0915174107 (2010).

9 Motzer, R. J. *et al.* Nivolumab plus Ipilimumab versus Sunitinib in Advanced Renal-Cell Carcinoma. *N. Engl. J. Med.* **378**, 1277-1290, doi:10.1056/NEJMoa1712126 (2018).

10 Overman, M. J. *et al.* Durable Clinical Benefit With Nivolumab Plus Ipilimumab in DNA Mismatch Repair–Deficient/Microsatellite Instability–High Metastatic Colorectal Cancer. *J. Clin. Oncol.* **36**, 773-779, doi:10.1200/jco.2017.76.9901 (2018).

11 Larkin, J. *et al.* Five-Year Survival with Combined Nivolumab and Ipilimumab in Advanced Melanoma. *N. Engl. J. Med.* **381**, 1535-1546, doi:10.1056/NEJMoa1910836 (2019).

12 Schadendorf, D. *et al.* Pooled Analysis of Long-Term Survival Data From Phase II and Phase III Trials of Ipilimumab in Unresectable or Metastatic Melanoma. *J. Clin. Oncol.* **33**, 1889-1894, doi:10.1200/jco.2014.56.2736 (2015).

13 Antonia, S. J. *et al.* Nivolumab alone and nivolumab plus ipilimumab in recurrent small-cell lung cancer (CheckMate 032): a multicentre, open-label, phase 1/2 trial. *The Lancet Oncology* **17**, 883-895, doi:10.1016/S1470-2045(16)30098-5 (2016).

14 Johnson, D. B. *et al.* Severe cutaneous and neurologic toxicity in melanoma patients during vemurafenib administration following anti-PD-1 therapy. *Cancer Immunol. Res.* **1**, 373, doi:10.1158/2326-6066.CIR-13-0092 (2013).

15 Bowyer, S. *et al.* Efficacy and toxicity of treatment with the anti-CTLA-4 antibody ipilimumab in patients with metastatic melanoma after prior anti-PD-1 therapy. *Br J Cancer* **114**, 1084-1089, doi:10.1038/bjc.2016.107 (2016).

16 Marabelle, A., Kohrt, H., Caux, C. & Levy, R. Intratumoral Immunization: A New Paradigm for Cancer Therapy. *Clin. Cancer Res.* **20**, 1747-1756, doi:10.1158/1078-0432.Ccr-13-2116 (2014).

17 Johnson, E. E. *et al.* Intratumoral immunocytokine treatment results in enhanced antitumor effects. *Cancer immunology, immunotherapy : CII* **57**, 1891-1902, doi:10.1007/s00262-008-0519-0 (2008).

18 Gimbel, M. I., Delman, K. A. & Zager, J. S. Therapy for Unresectable Recurrent and In-Transit Extremity Melanoma. *Cancer Control* **15**, 225-232, doi:10.1177/107327480801500305 (2008).
19 van Mierlo, G. J. D. *et al.* CD40 stimulation leads to effective therapy of CD40(-) tumors through induction of strong systemic cytotoxic T lymphocyte immunity. *PNAS* **99**, 5561-5566, doi:10.1073/pnas.082107699 (2002).
20 Galili, U., Wigglesworth, K. & Abdel-Motal, U. M. Intratumoral Injection of α-gal Glycolipids Induces Xenograft-Like Destruction and Conversion of Lesions into Endogenous Vaccines. *The Journal of Immunology* **178**, 4676-4687, doi:10.4049/jimmunol.178.7.4676 (2007).
21 Stone, G. W. *et al.* Nanoparticle-delivered multimeric soluble CD40L DNA combined with Toll-Like Receptor agonists as a treatment for melanoma. *PloS one* **4**, e7334-e7334, doi:10.1371/journal.pone.0007334 (2009).
22 Simmons, A. D. *et al.* Local secretion of anti-CTLA-4 enhances the therapeutic efficacy of a cancer immunotherapy with reduced evidence of systemic autoimmunity. *Cancer Immunol Immunother* **57**, 1263, doi:10.1007/s00262-008-0451-3 (2008).
23 Broomfield, S. A. *et al.* Locally Administered TLR7 Agonists Drive Systemic Antitumor Immune Responses That Are Enhanced by Anti-CD40 Immunotherapy. *The Journal of Immunology* **182**, 5217-5224, doi:10.4049/jimmunol.0803826 (2009).
24 Fransen, M. F., Sluijter, M., Morreau, H., Arens, R. & Melief, C. J. M. Local Activation of CD8 T Cells and Systemic Tumor Eradication without Toxicity via Slow Release and Local Delivery of Agonistic CD40 Antibody. *Clin. Cancer Res.* **17**, 2270-2280, doi:10.1158/1078-0432.Ccr-10-2888 (2011).
25 Fransen, M. F., van der Sluis, T. C., Ossendorp, F., Arens, R. & Melief, C. J. M. Controlled Local Delivery of CTLA-4 Blocking Antibody Induces CD8⁺ T-Cell–Dependent Tumor Eradication and Decreases Risk of Toxic Side Effects. *Clin. Cancer Res.* **19**, 5381-5389, doi:10.1158/1078-0432.Ccr-12-0781 (2013).
26 Sagiv-Barfi, I. *et al.* Eradication of spontaneous malignancy by local immunotherapy. *Sci. Transl. Med.* **10**, eaan4488, doi:10.1126/scitranslmed.aan4488 (2018).
27 Wang, S. *et al.* Intratumoral injection of a CpG oligonucleotide reverts resistance to PD-1 blockade by expanding multifunctional CD8⁺ T cells. *PNAS* **113**, E7240-E7249, doi:10.1073/pnas.1608555113 (2016).
28 Marabelle, A. *et al.* Depleting tumor-specific Tregs at a single site eradicates disseminated tumors. *The Journal of Clinical Investigation* **123**, 2447-2463, doi:10.1172/JCI64859 (2013).
29 Brody, J. D. *et al.* In Situ Vaccination With a TLR9 Agonist Induces Systemic Lymphoma Regression: A Phase I/II Study. *J. Clin. Oncol.* **28**, 4324-4332, doi:10.1200/jco.2010.28.9793 (2010).
30 Frank, M. J. *et al.* In Situ Vaccination with a TLR9 Agonist and Local Low-Dose Radiation Induces Systemic Responses in Untreated Indolent Lymphoma. *Cancer Discovery* **8**, 1258-1269, doi:10.1158/2159-8290.Cd-18-0743 (2018).
31 Ribas, A. *et al.* SD-101 in Combination with Pembrolizumab in Advanced Melanoma: Results of a Phase Ib, Multicenter Study. *Cancer Discovery* **8**, 1250-1257, doi:10.1158/2159-8290.Cd-18-0280 (2018).

32 Hanes, J. *et al.* Controlled Local Delivery of Interleukin-2 by Biodegradable Polymers Protects Animals from Experimental Brain Tumors and Liver Tumors. *Pharmaceutical Research* **18**, 899-906, doi:10.1023/A:1010963307097 (2001).
33 Hill, H. C. *et al.* Cancer Immunotherapy with Interleukin 12 and Granulocyte-Macrophage Colony-stimulating Factor-encapsulated Microspheres. *Coinduction of Innate and Adaptive Antitumor Immunity and Cure of Disseminated Disease* **62**, 7254-7263 (2002).
34 Eton, O. *et al.* Phase I trial of subcutaneous recombinant human interleukin-2 in patients with metastatic melanoma. *Cancer* **95**, 127-134, doi:10.1002/cncr.10631 (2002).
35 van Herpen, C. M. *et al.* Pharmacokinetics and Immunological Aspects of a Phase Ib Study with Intratumoral Administration of Recombinant Human Interleukin-12 in Patients with Head and Neck Squamous Cell Carcinoma. *A Decrease of T-bet in Peripheral Blood Mononuclear Cells* **9**, 2950-2956 (2003).
36 Ishihara, J. *et al.* Matrix-binding checkpoint immunotherapies enhance antitumor efficacy and reduce adverse events. *Sci. Transl. Med.* **9**, eaan0401, doi:10.1126/scitranslmed.aan0401 (2017).
37 Ishihara, J. *et al.* Targeted antibody and cytokine cancer immunotherapies through collagen affinity. *Sci. Transl. Med.* **11**, eaau3259, doi:10.1126/scitranslmed.aau3259 (2019).
38 Momin, N. *et al.* Anchoring of intratumorally administered cytokines to collagen safely potentiates systemic cancer immunotherapy. *Sci. Transl. Med.* **11**, eaaw2614, doi:10.1126/scitranslmed.aaw2614 (2019).
39 Ali, O. A., Emerich, D., Dranoff, G. & Mooney, D. J. In Situ Regulation of DC Subsets and T Cells Mediates Tumor Regression in Mice. *Sci. Transl. Med.* **1**, 8ra19-18ra19, doi:10.1126/scitranslmed.3000359 (2009).
40 Kim, J. *et al.* Injectable, spontaneously assembling, inorganic scaffolds modulate immune cells in vivo and increase vaccine efficacy. *Nature biotechnology* **33**, 64-72, doi:10.1038/nbt.3071 (2015).
41 Stephan, S. B. *et al.* Biopolymer implants enhance the efficacy of adoptive T-cell therapy. *Nature Biotechnology* **33**, 97-101, doi:10.1038/nbt.3104 (2015).
42 Park, C. G. *et al.* Extended release of perioperative immunotherapy prevents tumor recurrence and eliminates metastases. *Sci. Transl. Med.* **10**, eaar1916, doi:10.1126/scitranslmed.aar1916 (2018).
43 Wang, C. *et al.* In situ formed reactive oxygen species–responsive scaffold with gemcitabine and checkpoint inhibitor for combination therapy. *Sci. Transl. Med.* **10**, eaan3682, doi:10.1126/scitranslmed.aan3682 (2018).
44 Timko, B. P., Dvir, T. & Kohane, D. S. Remotely Triggerable Drug Delivery Systems. *Adv. Mater.* **22**, 4925-4943, doi:10.1002/adma.201002072 (2010).
45 Tong, R., Chiang, H. H. & Kohane, D. S. Photoswitchable nanoparticles for in vivo cancer chemotherapy. *PNAS* **110**, 19048-19053, doi:10.1073/pnas.1315336110 (2013).
46 Rwei, A. Y. *et al.* Ultrasound-triggered local anaesthesia. *Nature biomedical engineering* **1**, 644-653, doi:10.1038/s41551-017-0117-6 (2017).
47 Lu, Y., Aimetti, A. A., Langer, R. & Gu, Z. Bioresponsive materials. *Nature Reviews Materials* **2**, 16075, doi:10.1038/natrevmats.2016.75 (2016).
48 Farra, R. *et al.* First-in-Human Testing of a Wirelessly Controlled Drug Delivery Microchip. *Sci. Transl. Med.* **4**, 122ra121-122ra121, doi:10.1126/scitranslmed.3003276 (2012).

49 Milling, L., Zhang, Y. & Irvine, D. J. Delivering safer immunotherapies for cancer. *Advanced drug delivery reviews* **114**, 79-101, doi:10.1016/j.addr.2017.05.011 (2017).

50 Rahman, A. R. A., Register, J., Vuppala, G. & Bhansali, S. Cell culture monitoring by impedance mapping using a multielectrode scanning impedance spectroscopy system (CellMap). *Physiological Measurement* **29**, S227 (2008).

51 Morimoto, T. *et al.* A study of the electrical bio-impedance of tumors. *Journal of investigative surgery : the official journal of the Academy of Surgical Research* **6**, 25-32 (1993).

52 Hope, T. A. & Iles, S. E. Technology review: the use of electrical impedance scanning in the detection of breast cancer. *Breast Cancer Res* **6**, 69-74, doi:10.1186/bcr744 (2004).

53 Jahnke, H.-G. *et al.* Direct Chemosensitivity Monitoring Ex Vivo on Undissociated Melanoma Tumor Tissue by Impedance Spectroscopy. *Cancer Research* **74**, 6408-6418, doi:10.1158/0008-5472.can-14-0813 (2014).

54 Du, Z., Wan, H., Chen, Y., Pu, Y. & Wang, X. Bioimpedance spectroscopy can precisely discriminate human breast carcinoma from benign tumors. *Medicine* **96**, e5970, doi:10.1097/MD.0000000000005970 (2017).

55 Zhen, Z. *et al.* Tumor Vasculature Targeted Photodynamic Therapy for Enhanced Delivery of Nanoparticles. *ACS Nano* **8**, 6004-6013, doi:10.1021/nn501134q (2014).

56 Canales, A. *et al.* Multifunctional fibers for simultaneous optical, electrical and chemical interrogation of neural circuits in vivo. *Nat. Biotech.* **33**, 277, doi:10.1038/nbt.3093 (2015).

57 Yu, L. *et al.* Flexible Multi-Material Fibers for Distributed Pressure and Temperature Sensing. *Advanced Functional Materials* **30**, 1908915, doi:10.1002/adfm.201908915 (2020).

58 Tian, B., Shankarappa, S. A., Chang, H. H., Tong, R. & Kohane, D. S. Biodegradable Mesostructured Polymer Membranes. *Nano Lett.* **13**, 4410-4415, doi:10.1021/nl402251x (2013).

59 Yu, L. *et al.* Porous polymer optical fiber fabrication and potential biomedical application. *Opt. Mater. Express* **7**, 1813-1819 (2017).

60 Wu, H., Yang, Y., Bagnaninchi, P. O. & Jia, J. Electrical impedance tomography for real-time and label-free cellular viability assays of 3D tumour spheroids. *Analyst* **143**, 4189-4198, doi:10.1039/C8AN00729B (2018).

61 Venkatanarayanan, A., Keyes, T. E. & Forster, R. J. Label-free impedance detection of cancer cells. *Anal Chem* **85**, 2216-2222, doi:10.1021/ac302943q (2013).

62 Stanica, L. *et al.* Electric Cell-Substrate Impedance Sensing of Cellular Effects under Hypoxic Conditions and Carbonic Anhydrase Inhibition. *Journal of Sensors* **2017**, 9290478, doi:10.1155/2017/9290478 (2017).

63 Benson, K., Cramer, S. & Galla, H. J. Impedance-based cell monitoring: barrier properties and beyond. *Fluids Barriers CNS* **10**, 5, doi:10.1186/2045-8118-10-5 (2013).

64 Amini, M., Hisdal, J. & Kalvøy, H. Applications of bioimpedance measurement techniques in tissue engineering. *Journal of Electrical Bioimpedance* **9**, 142-158 (2018).

65 Duck, F. A. in *Physical Properties of Tissues* (ed Francis A. Duck) 167-223 (Academic Press, 1990).

66 Wagner, M. & Wiig, H. Tumor Interstitial Fluid Formation, Characterization, and Clinical Implications. *Front Oncol* **5**, 115, doi:10.3389/fonc.2015.00115 (2015).

67 Patrizia, A. *et al.* Photodynamic therapy of cancer: An update. *CA: Cancer J. Clin.* **61**, 250-281, doi:doi:10.3322/caac.20114 (2011).

68 Castano, A. P., Mroz, P. & Hamblin, M. R. Photodynamic therapy and anti-tumour immunity. *Nat. Rev. Cancer* **6**, 535, doi:10.1038/nrc1894 (2006).
69 Gollnick, S. O. *et al.* Role of cytokines in photodynamic therapy-induced local and systemic inflammation. *Br. J. Cancer* **88**, 1772, doi:10.1038/sj.bjc.6600864 (2003).
70 He, C. *et al.* Core-shell nanoscale coordination polymers combine chemotherapy and photodynamic therapy to potentiate checkpoint blockade cancer immunotherapy. *Nature Communications* **7**, 12499, doi:10.1038/ncomms12499 (2016).
71 Xu, J. *et al.* Near-Infrared-Triggered Photodynamic Therapy with Multitasking Upconversion Nanoparticles in Combination with Checkpoint Blockade for Immunotherapy of Colorectal Cancer. *ACS Nano* **11**, 4463-4474, doi:10.1021/acsnano.7b00715 (2017).
72 Kleinovink, J. W., Fransen, M. F., Löwik, C. W. & Ossendorp, F. Photodynamic-Immune Checkpoint Therapy Eradicates Local and Distant Tumors by CD8⁺ T Cells. *Cancer Immunol. Res.* **5**, 832-838, doi:10.1158/2326-6066.cir-17-0055 (2017).
73 Song, W. *et al.* Enhanced Immunotherapy Based on Photodynamic Therapy for Both Primary and Lung Metastasis Tumor Eradication. *ACS Nano* **12**, 1978-1989, doi:10.1021/acsnano.7b09112 (2018).
74 Chen, B. *et al.* Tumor Vascular Permeabilization by Vascular-Targeting Photosensitization: Effects, Mechanism, and Therapeutic Implications. *Clin. Cancer Res.* **12**, 917-923, doi:10.1158/1078-0432.ccr-05-1673 (2006).
75 Wang, Y. *et al.* Photodynamic induced uptake of liposomal doxorubicin to rat lung tumors parallels tumor vascular density. *Lase Surg. Med.* **44**, 318-324, doi:doi:10.1002/lsm.22013 (2012).
76 Snyder, J. W., Greco, W. R., Bellnier, D. A., Vaughan, L. & Henderson, B. W. Photodynamic Therapy. *A Means to Enhanced Drug Delivery to Tumors* **63**, 8126-8131 (2003).
77 Duan, Y. Y., Clark, G. M. & Cowan, R. S. C. A study of intra-cochlear electrodes and tissue interface by electrochemical impedance methods in vivo. *Biomaterials* **25**, 3813-3828, doi:https://doi.org/10.1016/j.biomaterials.2003.09.107 (2004).
78 Euhus, D. M., Hudd, C., Laregina, M. & Johnson, F. E. TUMOR MEASUREMENT IN THE NUDE-MOUSE. *J. Surg. Oncol.* **31**, 229-234, doi:10.1002/jso.2930310402 (1986).
79 Inoue, Y., Izawa, K., Kiryu, S., Tojo, A. & Ohtomo, K. Diet and abdominal autofluorescence detected by in vivo fluorescence imaging of living mice. *Molecular imaging* **7**, 21-27 (2008).

Chapter 6
Overview and future direction

6.1 Overview

In this thesis, a new set of biomedical applications have been introduced based on previously developed polymer fiber drawing technique. These unconventional multifunctional fiber-based devices have not only enabled the studies of neural circuitry but also allowed for the assessment of silent cells that are not capable of firing action potential both in vitro and in vivo.

First, supported by femtosecond laser micromachining technique and unique helical scaffolds, we developed a spatially expandable fiber-based probe, enabling us to map the deep brain regions across unprecedented distances. By incorporating optical and chemical modalities into the probes, we also enable simultaneous neural stimulation and recording across distant deep brain regions. This platform also enables new applications in diseases such as the precise identification of epileptic seizure foci which is not achievable using existing methods.

Secondly, we successfully integrated the periodic nano-optoelectrodes onto the tips of multifunctional fibers via a free-standing nanohole array mask. The nano-optoelectrodes can serve as not only optical nanoantennas for spectroscopic bio-/chemical detection but also nanostructured electrodes for improved electrophysiology recording. This integrated fiber demonstrates an entirely new platform of merging a label-free bio-/chemical sensor and electrophysiology recording electrodes into a single device.

Another feasible label-free fiber-based sensor has been permitted by a hollow, copper-electrode based fiber fabricated by a novel convergency fiber drawing method. Using electrochemical impedrimetric sensing technique, the high electrically conductive electrode-based

fiber sensor enabled not only real-time non-invasive monitoring of compositional and quality analysis of the extruded bioinks during 3D bioprinting processes, but also served as the printing nozzle wish scalable diameter configuration.

Finally, the employment of this hollow, copper-electrode-embedded fiber probe in multiple tumor models demonstrates its in vivo application regarding immune checkpoint blockade antibodies delivery and simultaneous tumor impedance monitoring. In addition to the interior hollow channel for delivering hydrophilic antibodies, hydrophobic photosensitizers can be delivered to the tumor tissue via repetitive coating on the outer surface of the fiber. In summary, our device has presented the versatility to deliver various drugs at controlled concentrations and is potentially useful for delivering immunotherapeutics while minimizing their toxicities.

6.2 Future direction

The multimaterial multifunctional fiber-based neural interfaces were first developed in 2015. Despite the short history of this field, prominent progress has been made, and significant potential has been demonstrated for both basic and clinical biomedical applications. Looking into the future, we believe there are still many unanswered questions to be addressed.

Firstly, even the femtosecond laser micromachining technique facilitated the multiple interfacing site of the fiber probes along the longitudinal direction, the integration of the micromachined fiber to a more sophisticated device is still a challenge, especially for controlling the individual waveguide.

In Chapter 2, we have presented a technique that can create electrical, microfluidic, and optical windows along the fiber length via femtosecond micromachining. A neural probe that has this multilayer geometry (three-layer structure and has three optical waveguides and three electrodes in each layer) where each optical excitation site has its own neighboring electrical

opening for a more precise monitoring and manipulating the activity of neural circuits in behaving animals can be developed (**Figure 6.1**).

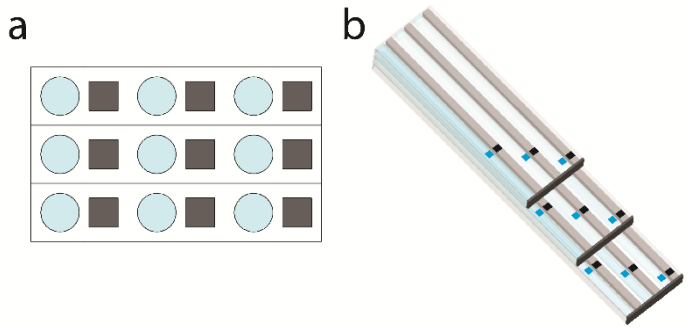

Figure 6.1 Schematic illustration of the designed fiber structure with 9 electrodes and 9 waveguides. (a) The cross-sectional view. (b) The ultimate structure with the electrodes and waveguides exposed by femtosecond laser micromachining.

Secondly, the backend connection needs to be improved for scalable applications. Instead of manual connectorization, flip-chip bonding or wire bonding methods may be employed to connect the electrodes at the fiber backend.

For example, electrical and photonic wire bonding can be introduced to silicon chips enabling compact connections for chronic implantation. To this end, fiber tip will be polished with a fiber slicer and the fiber probe's tip will need to be aligned with a designed chip. Then the electrodes of the fiber will be electrically connected to the chip circuit via wire bonding. After that, the chip will be embedded in a photosensitive resist. The shape of the photonic wire bond (PWB) waveguide will be defined using two-photon lithography which can be realized by femtosecond laser. The unexposed resist will be removed by a development step, and the structures will finally be embedded in a low-index cladding material for optical confinement and electrical insulation. **Figure 6.2** shows the schematics of fiber-to-chip bonding with detailed electrical and photonic wire bonding illustrations where the fiber holds two cylindrical layer structure with 16 electrodes, four waveguides, and one microfluidic channel in total. After the electrical and photonic bonding,

the microfluidic channel can be exposed using femtosecond laser micromachining, and manually connected to a miniaturized tubing.

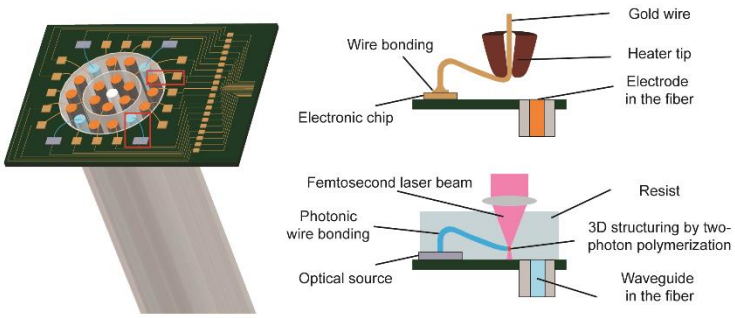

Figure 6.2 Illustration of the fiber-to-chip bonding (left) with detailed electrical (top right) and photonic (bottom right) bonding methods.

Thirdly, the impedance of polymer electrodes needs to be further reduced to minimize the device footprint. One approach is to incorporate nanomaterials (nanofibers, nanotubes, or nanowires) inside and outside the polymer electrodes to enhance the conductivity and charge transport. Moreover, other functionalities that mimic brain complexity can be integrated into the fibers, including chemical sensing fibers, mechanically adaptive fibers, acoustic fibers, and biodegradable fibers.

In our previously published work, we have proved that carbon nanofibers (CNFs) improved the *in vivo* electrical recording performance due to the CNFs alignment during thermal drawing process[1]. Carbon nanotubes (CNTs) have intrinsically large surface areas and intriguing electrical and physical properties, including extremely high conductance and aspect ratios[2]. These attributes suggest that a microelectrode integrated with CNTs may have lower impedance and higher charge transfer characteristics. In addition, CNTs are expected to facilitated the advancement of electrodes through the dura mater due to their mechanical properties[3]. It has been shown that nanotubes can sustain and promote neuronal electrical activity in networks of cultured cells[4], which might result from forming tight contacts with cell membranes that might favor electrical shortcuts using single-

cell electrophysiology technique[5]. Many reports have also demonstrated that electrodes with CNT coating have improved *in vivo* neural recording performance both in rats and primates[6,7]. Hence, I believe that a polymer microelectrode with CNTs enhancement can be the ideal candidate or obtaining loose-patch-juxtacellular recording on brain slides or *in vivo* and some preliminary results have been collected towards this direction.

We have successfully created a polymer composite made of 12.5 wt% CNTs evenly distributed in conductive polyethylene (CPE) via hot pressing and melt mixing. We then implemented the polymer composite into a preform and drew the preform into thin fibers. In the fiber, the core material is polycarbonate polycarbonate (PC, refractive index n_{PC}=1.586) and the insulating material is polyvinylidene difluoride (PVDF, refractive index n_{PVDF}=1.426) which serve as the core and the shell of an optical waveguide. To exam the potential use of the CNT-CPE fiber as a neural probe, its electrochemical impedance characteristics were evaluated via electrochemical impedance spectrum (EIS) (Interface 1010E, Gamry Instruments). Measurements adopted the schemes of a two electrode setup, which consisted of a 2 cm-long CNT-CPE fiber as a working electrode and a Pt wire as a counter electrode as shown in **Figure 6.3**.

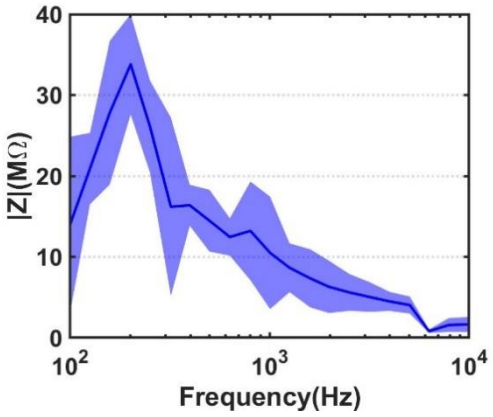

Figure 6.3 Impedance results of the CNT-CPE electrode.

We then implanted the CNT-CPE fiber into the hippocampus region of the wild type mice brain. At day 10 post implantation, neural activities were successfully recorded and the well-isolated cluster further confirmed the capability of the CNT-CPE electrode to record neural activities at single-unit resolution as shown in **Figure 6.4a-b**. Beyond recording endogenous neural activities in wild type mice, simultaneous optogenetic stimulation and electrical recording have also been carried out on Thy1-ChR2-YFP mice. The waveguide in the fiber probe is coupled to a laser source with a wavelength of 473nm. We can record optically evoked neural activities corresponding to each laser pulse as indicated by the blue dot (**Figure 6.4c**).

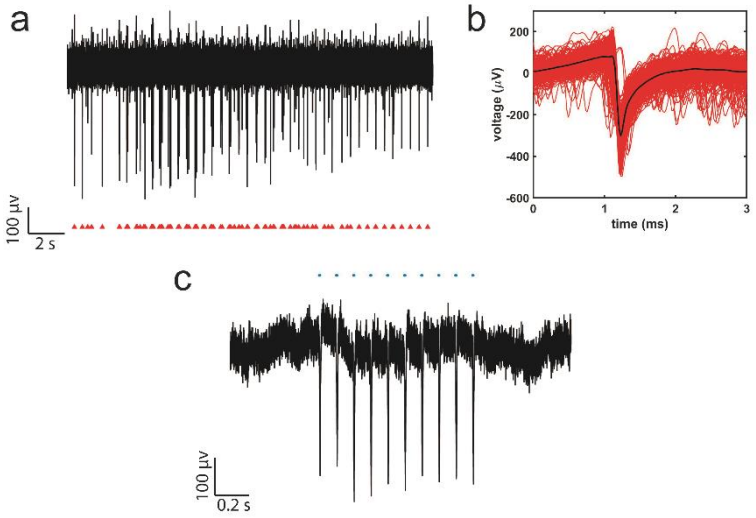

Figure 6.4 In vivo electrophysiology result by using the CNT-CPE electrode. (a) Endogenous neural activity was detected by the CNT-CPE fiber probe 10 days post implantation. (b) The recorded signal was well isolated into one cluster. (c) Optogenetic control of the brain activity via the CNT-CPE functional fiber probe.

Last but not least, applications of the fluidic channel are also largely unexplored where it has been only used for administration of drug or other substances other than withdrawning fluidic sample directly from the brain tissue.

As described in Chapter 3, we have developed a miniaturized multifunctional neural probe platform that can integrate optical nanoplasmonic biosensors and neural recording microelectrodes

on the tip of a flexible and biocompatible polymer fiber. To exploit the motimodal fibers, I believe that functional fiber can serve as an alternative approach to detect neurotransmitters adopting electrochemical method and microdialysis in a single device. In this proposed approach, ideally we can obtain real-time information from the electrochemical measurements and quantitative information of a wide variety of biomarkers through microdialysis.

All of these efforts will rely on the advancement of multiple fields ranging from materials science, optics, electronics, chemistry, mechanics, to biology. Moreover, significant impacts can be made through close collaboration among engineers, biologists, and neuroscientists.

6.3 References

1 Guo, Y. Y. *et al.* Polymer Composite with Carbon Nanofibers Aligned during Thermal Drawing as a Microelectrode for Chronic Neural Interfaces. *Acs Nano* **11**, 6574-6585 (2017).

2 Wang, K., Fishman, H. A., Dai, H. & Harris, J. S. Neural stimulation with a carbon nanotube microelectrode array. *Nano Lett* **6**, 2043-2048 (2006).

3 Malarkey, E. B. & Parpura, V. Carbon nanotubes in neuroscience. *Acta Neurochir Suppl* **106**, 337-341 (2010).

4 Lovat, V. *et al.* Carbon nanotube substrates boost neuronal electrical signaling. *Nano Lett* **5**, 1107-1110 (2005).

5 Cellot, G. *et al.* Carbon nanotubes might improve neuronal performance by favouring electrical shortcuts. *Nat Nanotechnol* **4**, 126-133 (2009).

6 Keefer, E. W., Botterman, B. R., Romero, M. I., Rossi, A. F. & Gross, G. W. Carbon nanotube coating improves neuronal recordings. *Nat Nanotechnol* **3**, 434-439 (2008).

7 Zhang, H., Shih, J., Zhu, J. & Kotov, N. A. Layered nanocomposites from gold nanoparticles for neural prosthetic devices. *Nano Lett* **12**, 3391-3398 (2012).